Characterization of doping atoms (Ta, Nb) in advanced PEM fuel cell supports and catalysts as well as of the surface-solvent interaction of laser-generated Pt nanoparticles
A XAFS study

Dissertation

zur

Erlangung des Doktorgrades (Dr. rer. nat.)

der

Mathematisch-Naturwissenschaftlichen Fakultät

der

Rheinischen Friedrich-Wilhelms-Universität Bonn

vorgelegt von

Mathias Fischer

aus

Schwabach

Bonn 2016

Angefertigt mit Genehmigung der Mathematisch-Naturwissenschaftlichen Fakultät der
Rheinischen Friedrich-Wilhelms-Universität Bonn

1. Gutachter: Prof. Dr. J. Hormes
2. Gutachter: Prof. Dr. S. Linden

Tag der Promotion: 11.11.2016
Erscheinungsjahr: 2016

Table of contents

List of figures

List of tables

1. Introduction

Richard Feynman's famous speech "There's plenty of room at the bottom" [1] over 50 years ago marked the beginning of a new era: nanotechnology. Nowadays nanoparticles (NPs) find application in many research areas, *e.g.* biology, chemistry, or material science, in which they are used as markers [2], catalysts [3], or gas sensors [4]. But "nano" made its way even into our everyday life, for instance, by making building materials more durable or clothes self-cleaning through water-repelling textiles [5]. Since in this day and age it is almost impossible to not get in contact with nanotechnology: what does make nanomaterials so special? First off, a material gets the attribute "nano" when its size in one dimension is smaller than 100nm. This has the consequence of a much higher surface-volume ratio compared to its bulk counterpart. As an example: NPs with a size of 2nm have almost 50% of its atoms sitting on the surface [6]! This has an advantageous effect in catalysis because here reactions happen on the particles' surfaces. Increasing the surface area increases the number of catalytically active sites and thus a material's catalytic activity. A higher relative number of surface atoms also has an impact on a particle's electronic structure because surface atoms are under-coordinated and occupy step, edge and corner sites. For metals an additional difference occurs: a smaller particle size also means a lower number of electrons potentially contributing to hybridization. In case of platinum NPs this has the effect that the average number of 5d electrons is between the bulk value and the value for single Pt atoms [7]. The reason is hybridization of s-, p- and d-states which, compared to single atoms, is present in bulk but less pronounced on the nanoscale. Thus it is safe to say that a nanomaterial's surface has a decisive influence on its properties. This circumstance bears opportunities as well as challenges. On the one hand nanostructures show properties different from their bulk counterpart. Gold NPs for instance can be used as catalysts whereas gold is inert in the macroscopic world [8]. Additionally some properties become size-dependent - one prominent example being the quantum size effect: the band gap of semiconducting nanomaterials shows an inverse trend with their size [9]. On the other hand, the high relative number of surface atoms makes NPs prone to agglomeration and ultimately growth which decreases their relative surface area and thus the feature nanomaterials are made for in the first place. To prevent this from happening two approaches are being applied: particles can either be "anchored" to a support [10], [11] or coated [12]. The latter has a major impact on the macroscopic properties of nanoparticles, *e.g.* their magnetic properties [13].

There are two groups of techniques to produce nanomaterials: “top down” and “bottom up”. “Top down” means that a bulk material is the precursor from which NPs are produced. Lithography, used to create microchips, is a prominent example for a top down technique. “Bottom up”, on the other hand, makes use of the ability of atoms and molecules to self-assemble; a concept nature made use of for a very long time. The most commonly found representatives of bottom-up approaches are wet-chemical synthesis routes [14]. By adjusting the conditions (*e.g.* reaction temperature, choice of additives) one has good control over particle properties like morphology and size. An interesting alternative that emerged in the last few decades, which combines aspects of both approaches, is PLAL (pulsed laser ablation in liquids). The precursor in this case can either be a foil or a pressed powder that is sitting in an organic or inorganic solution. To create nanoparticles one focusses a pulsed laser beam onto the target. Upon absorption several processes are triggered, which eventually lead to nanoparticle formation. Good review articles that contain information about this process, an overview of products, as well as pros and cons of this method are [15] and [16]. The major difference between PLAL and wet-chemical synthesis routes is that via PLAL stabilization of NPs can be achieved without using any additional additives. But whichever way a nanomaterial was created, there is one common post-synthesis step to tailor its properties to a certain application: “functionalization”. This term means that nanostructures are being coated and/or deposited on a support to optimize their size, morphology, composition, or indeed their whole electronic and geometric structure to any given application.

The following thesis is divided into three parts. In the first two parts I characterized PEM (“polyelectrolyte membrane”) fuel cell supports and catalyst-support units. A fuel cell is a device that produces electricity. Today there are about 6 different kinds [17]. They all have the same basic components: an anode chamber in which one fuel gets oxidized, a cathode chamber in which another fuel gets reduced and a membrane of some sort to prevent the two fuels from mixing. One kind is the PEM fuel cell which runs on H_2 and O_2 and is thus the most promising candidate to someday replace the combustion motor in times of fuel scarcity and climate changes. Yet, performance, stability and costs still need to be improved for this fuel cell to become a real alternative. A particularly challenging obstacle is increasing the ORR (oxygen reduction reaction) activity. Out of a variety of approaches for improvement that are being followed in the scientific community today, optimizing the catalyst is the one most commonly pursued. However, just concentrating on the catalyst proved insufficient; its support needs to be improved as well. A support is needed to provide for high dispersion of

catalyst particles and to maintain this dispersion during operation. This works best in case of a strong metal-support interaction (SMSI), *i.e.* a charge transfer between catalyst and support particles, which has additional enhancing effects on the catalytic activity of a modern catalyst-support unit [18]. Both components are nowadays mostly nanostructures due to their high surface area. Carbon, especially carbon black, was the best PEM fuel cell support for decades because it offers a high surface area and excellent electronic and thermal conductivity. Yet, finding an appropriate alternative is indispensable because carbon oxidizes at conditions that develop in a fuel cell, leading to growth of catalyst particles and ultimately loss of performance following the mechanism [19]:

$$C + 2H_2O \rightarrow CO_2 + 4H^+ + 4e^-$$

TiO_2 is an alternative that has the advantage of a better stability over C yet inferior conductive properties [19]. Stability in this context is defined as the percentage of electrochemically active surface area remaining after a certain time of operation. Because no single support material at present can match carbon regarding surface area, costs and conductive properties, creating a C-TiO_2 hybrid support is a very encouraging solution. To improve electronic conductivity and stability of this hybrid support doping TiO_2 with pentavalent ions proved most successful so far [20].

In part one of this thesis I studied TiO_2-based nano-supports, co-doped with Ta and Nb. Two hybrid and one core-shell support were created using TiO_2 and the carbon blacks “KB” (Ketjenblack EC-600JD by AkzoNobel [21]) and “TKKE” (the E-type carbon black by Tanaka Kikinzoku International (America) Inc.). In addition a catalyst-support sample was made by depositing Pt NPs onto the doped TiO_2 support. The goal was to investigate how doping affects the respective host structure in a single/hybrid support as well as a catalyst-support sample.

In part two I examined the reduction/oxidation behaviour of two PEM fuel cell PtPd nano-catalysts deposited on the above described C-TiO_2 hybrid supports. As mentioned before, nanomaterials have strong affinity to form bonds. With catalysts this can lead to agglomeration or adsorption, which blocks catalytically actives sites thus decreasing a catalyst’s activity. To what extent this is the case for this group of fuel cell catalysts during reduction/oxidation is addressed.

In part three the particle-solvent interaction of additive-free Pt NPs, synthesized via PLA in water, was characterized *in situ*. Moreover, citrate and phosphate ions were added separately

ex situ. Both are used to increase the particles' stability, *i.e.* to decrease their affinity for agglomeration, through electrostatic repulsion upon adsorption [22], [23]. The interaction of these ions with the particles was studied as well. In addition, the impact of depositing Pt onto TiO_2 NPs was the subject of research. Since this is the first time, to the best of my knowledge, that the particle-solvent interactions of laser-generated nanomaterials were characterized *in situ*, results gathered in this part are compared to those of similar samples synthesized wet-chemically.

The most common techniques applied to characterize nanomaterials are TEM (transmission electron microscopy), XRD (x-ray diffraction) and XPS (x-ray photoelectron spectroscopy). TEM is an imaging technique with which one can, for instance, get particle size distributions, tell if a deposition process worked, or if particles agglomerate. XRD on the other hand is a diffraction technique. It is applied to make qualitative/quantitative phase analyses or get crystallographic information such as lattice parameters. XRD's main disadvantage for the characterization of nanostructures is that only samples with a certain degree of long-range order give a decent signal standing out from an omnipresent background. This technique thus reaches its limits for very small and/or disordered structures. Furthermore both, TEM and XRD, are not surface-sensitive. As mentioned in the beginning, in the nano-world the surface has a tremendous impact on a material's properties so it is of the utmost importance to learn how a nanomaterial interacts with its environment. In contrast, XPS is a surface-sensitive technique, because it measures electrons that have an escape depth of typically a few nm [24]. At the same time XPS is at a disadvantage because XPS experiments require (ultra) high-vacuum conditions, which disqualifies this technique for *in situ* experiments. XAFS (x-ray absorption fine structure) is an excellent tool to characterize nanomaterials. Its main advantage is that it is the only technique available which with the electronic and geometric structure of all atoms of a given element can be studied simultaneously as well as *in situ*. In contrast to XRD no long-range order is required. Compared to XPS, XAFS has the advantage that it is sensitive to an element's bonding environment. If, for instance, molecules adsorb on NP surfaces this process will be noticeable in XPS as well as XAFS spectra. Yet, XAFS spectra contain the additional information which molecule it is - sufficiently small particle sizes provided. This needs to be mentioned since XAFS is an averaging technique meaning that core and surface atoms both contribute to the signal weighted by their relative number. A smaller particle size equals a higher relative number of surface atoms resulting in a higher sensitivity to what happens on particles' surfaces. The following advantages made x-ray

absorption spectroscopy a particularly excellent choice to answer questions posed in all three parts of this work: (i) one can measure the electronic and geometric structure of all atoms of a given element simultaneously even at low concentrations. (ii) Because this technique is element-specific one can study the impact of doping from the point of view of the host structure and the one of the dopant. (iii) One can monitor changes *in situ*.

As prove for the accuracy of these statements some key results of each part of my thesis are now summarized. Results in part one will show that the synthesis process was successful. The dopants Ta and Nb did in fact replace Ti atoms and are statistically distributed in their respective TiO_2 host structure. One piece of evidence is the interplay of each of these elements' electronic and geometric structure. Crystal field effects cause splitting of the Ta5d/Nb 4d levels which gets more pronounced the more dopant-O_6 octahedra are distorted. Results in part two will show that Pt atoms in PtPd catalysts supported on C-TiO_2 hybrid supports show low affinity for oxidation. They are easily reduced and withstand harsh oxidizing conditions. Results in part three will show that the surfaces of Pt NPs synthesized wet-chemically and via PLAL are indeed different.

2. Methods

X-rays are part of the electromagnetic spectrum with energies in the range of about 1 to 100keV (roughly corresponding to wavelengths of 10 to 0.1Å, [25]). When x-rays pass through a homogenous medium they get attenuated according to the Beer-Lambert law [24]:

$$I = I_0 \cdot e^{-\mu d}$$

"I" and "I_0" stand for the beam intensity after and before interaction with the medium, "d" is the sample thickness and "μ" is the linear absorption coefficient. The latter is actually a sum of coefficients representing processes responsible for the attenuation of radiation in matter, which include the photoelectric effect as well as (elastic) Rayleigh and (inelastic) Compton scattering. Their cross-sections are shown schematically in Figure 2.1 as a function of photon energy in keV [26]:

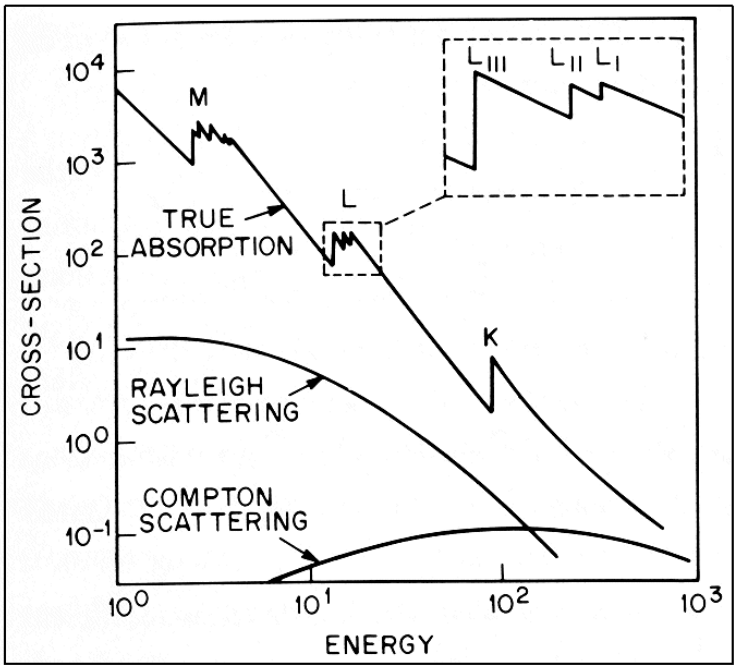

Figure 2.1: schematic cross-sections for photoelectric effect ("true absorption"), Rayleigh and Compton scattering as a function of photon energy in keV. Letters and roman numerals refer to absorption edges as explained in the text

In the x-ray regime the photoeffect dominates (marked "true absorption" in Figure 2.1). Here an inner shell electron absorbs a photon and the now called "photoelectron" gets promoted either into a higher unoccupied valence state or the continuum if the photon energy exceeds its binding energy (Figure 2.2a, modified from [27]). The photoelectron leaves behind a core hole and the atom is then said to be in an "excited state". In the x-ray range this state has a life time of femtoseconds after which the core hole gets filled by an electron from a higher shell which is called "relaxation". Relaxation implies that the excited atom releases the energy it

gained by photon absorption (= binding energy of the inner shell electron - binding energy of the higher shell electron). This energy difference gets predominantly set free either by creating (fluorescence) photons or a transfer to and release of (Auger) electrons as can be seen in Figure 2.2b and c [27]:

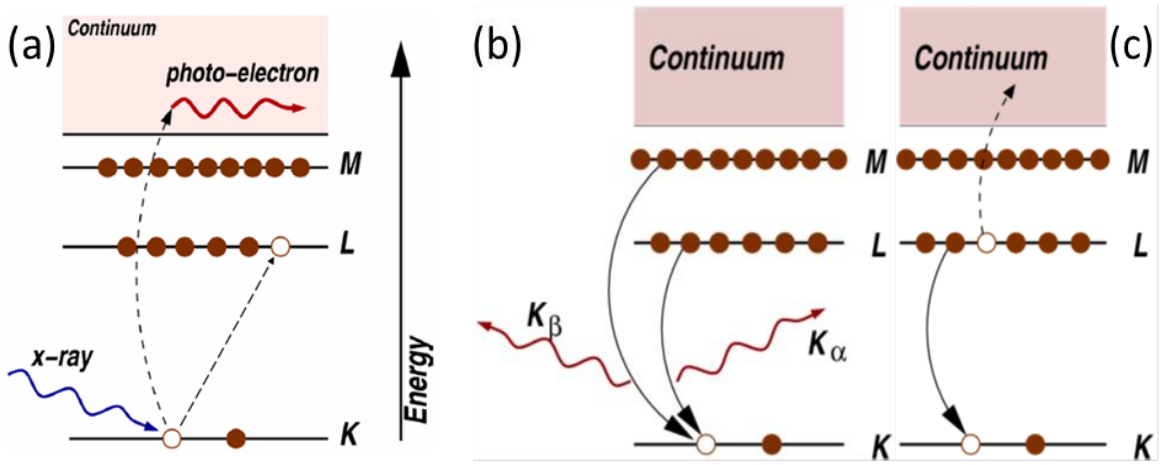

Figure 2.2: schematic of photoeffect and follow-up processes. (a) excitation of an inner shell electron to an unoccupied valence state or the continuum after absorption of a photon and follow-up processes (b) creation of a fluorescence photon or (c) release of an Auger electron. "K", "L" and "M" stand for the respective electron shells corresponding to the principal quantum numbers n = 1, 2 and 3. "Kα" and "Kβ" symbolize fluorescence photons that result in the respective emission lines.

The photoelectric effect has a E^{-3} dependence. Yet at certain energies there are discontinuities, so-called "edge jumps", which on closer inspection are not smooth but have a superimposed fine structure. This structure has several possible contributions: (1) transitions from a bound core state to Rydberg states and the unbound continuum. This is the case for monoatomic gases because they have only complete valence shells. For all other samples two additional effects occur: (2) transitions from a bound core to a bound but unoccupied valence state (since the absorber atom does have at least one partially filled valence shell). And at higher energies: (3) scattering of the ejected core electron off of the electrons of neighbouring atoms. The fact that binding energies of core electrons are unique (Moseley's Law) makes x-ray absorption spectroscopy element-specific.

Not every possible transition to a bound, unoccupied valence state actually can be observed. For dipole transitions the following selection rules apply:

$$\Delta l = \pm 1$$
$$\Delta j = 0, \pm 1 \quad \text{(but not } 0 \rightarrow 0\text{)}$$

"Δl" and "Δj" stand for the difference in angular momentum and total angular momentum quantum number, respectively. Examples for transitions following these rules and the corresponding absorption edges are:

1s	→	$np_{1/2, 3/2}$	K edge
2s	→	$np_{1/2, 3/2}$	LI edge
$2p_{1/2}$	→	$nd_{3/2}$	LII edge
$2p_{3/2}$	→	$nd_{3/2, 5/2}$	LIII edge

In general, a "Δl = -1" transition (*e.g.* p to s orbital) is also allowed but a lot weaker and thus commonly neglected. An example of an absorption edge and its fine structure (Ti K edge rutile spectrum) is shown in Figure 2.3:

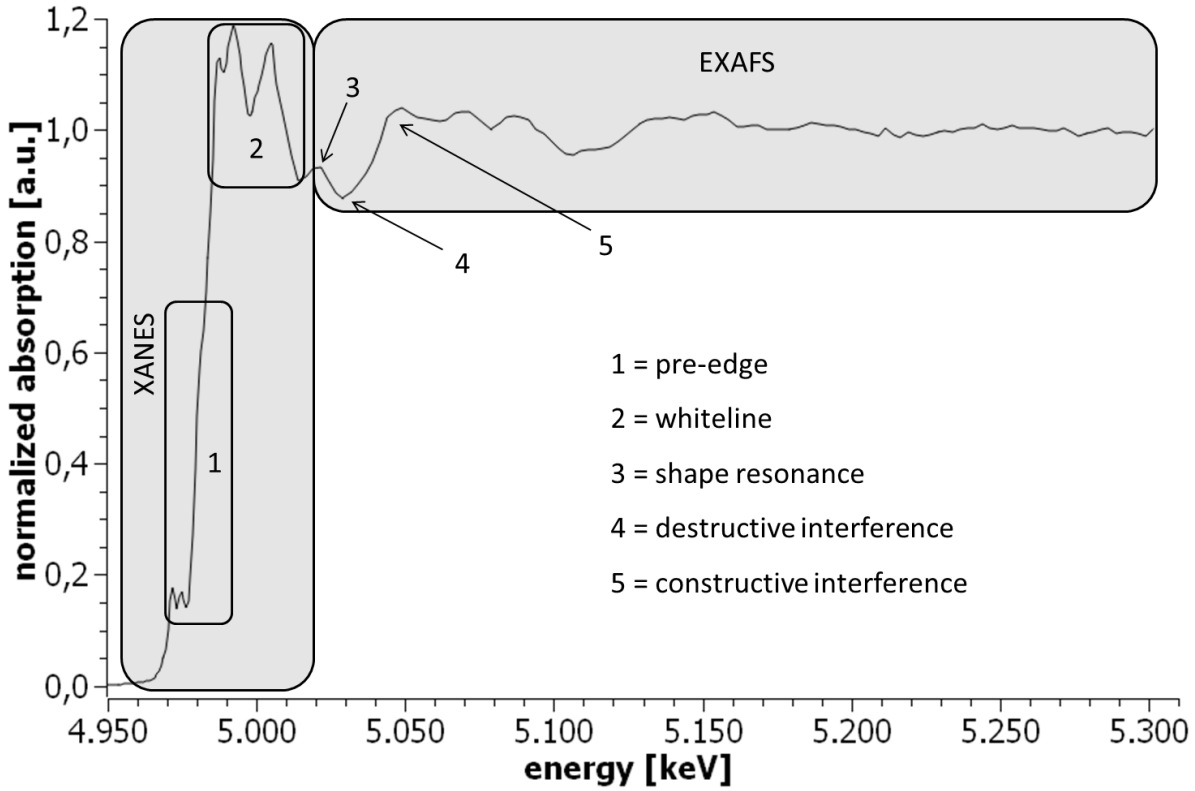

Figure 2.3: normalized Ti K edge spectrum of rutile (features are explained in the text)

The main features of the fine structure are explained in the following:

– whiteline

This is the peak(s) right after the sharp rise in absorption. It is attributed to transitions from a bound core to the lowest bound but unoccupied valence state. This state's occupancy or DOS (density of states) is therefore quantitatively measured by the whiteline intensity. In case of a complete valence shell there is no pronounced whiteline. The whiteline position shifts to higher energies for a higher average oxidation state of the absorber atoms ("chemical shift"). That is because the positive charge of the nucleus attracts all surrounding electrons of a given atom. The fewer electrons there are, shared with or transferred to neighbouring atoms, the more strongly the remaining ones are bound.

– pre-edge

The factors leading to the existence as well as characteristics of pre-edge features are complex and not yet completely understood. Nonetheless it is generally accepted that hybridization of p- and d-states plays an important role since electron transitions that cause the whiteline are to the lowest unoccupied valence state. To observe features at even lower energies electron levels have to exist to which photoelectrons can make transitions. Hybridization creates these electron levels. For instance: K edge whitelines are caused by transitions from 1s to np orbitals whereas transitions to (n-1)d orbitals are dipole-forbidden. Yet, if the local symmetry around the absorbing atoms is not centrosymmetric these np and (n-1)d orbitals hybridize, which enables transitions to hybrid orbitals that have p-character. Thus, from the characteristics of pre-edge features one can derive information about the local symmetry around absorbing atoms.

– shape resonances

Shape resonances occur just above the ionization energy where the wavelengths of photoelectrons are longer than the distance absorber atom-nearest neighbour. They are caused by multiple scattering of photoelectrons off neighbouring atoms and are influenced by the potential photoelectrons experience upon leaving absorber atoms.

All these features can be observed in the region that is called XANES ("x-ray absorption near-edge structure"). Since *ab initio* XANES spectra calculations are still a challenge up to today, the most common approach used to extract information is called "finger-printing". In this method the above described features are compared between an unknown sample and a known reference spectrum. Several approaches are available today to gain even more detailed information, for instance, LCF (linear combination fitting), PCA (principal component analysis) and peak fitting. More details about these techniques and their applications can be found in [28].

Following XANES at higher energies is the so-called EXAFS region ("extended x-ray absorption fine structure") whose features are marked "destructive interference" and "constructive interference" in Figure 2.3. Side note: XANES and EXAFS are commonly combined to the collective term XAFS ("x-ray absorption fine structure"). There is no clear threshold when the XANES regions ends and the EXAFS region begins. A rule-of-thumb separates them when the wavelength of the photoelectron is the same as the distance of the absorbing atoms to their nearest neighbours. So what happens in the EXAFS region? It was already established that a photoelectron leaves an absorber atom if the photon energy exceeds its binding energy - the difference being transferred to the photoelectron as kinetic energy. For

the explanation of EXAFS features it proved advantageous to treat the photoelectron as a (spherical) wave rather than a particle. After leaving its core state this photoelectron wave gets scattered back by electron shells of neighbouring atoms which can happen once (single scattering) or more than once (multiple scattering). When the photoelectron wave returns to its absorber atom there will be a phase difference with the outgoing wave. Its extent depends on the incoming photon energy (determining the wavelength of the photoelectron) as well as the distance and kind of the neighbouring atoms (determining their backscattering properties). Because the last two factors are fixed for a given sample, increasing the incoming photon energy causes alternating constructive and destructive interference, noticeable as maxima and minima in an absorption spectrum. Figure 2.4 shows this schematically [29]:

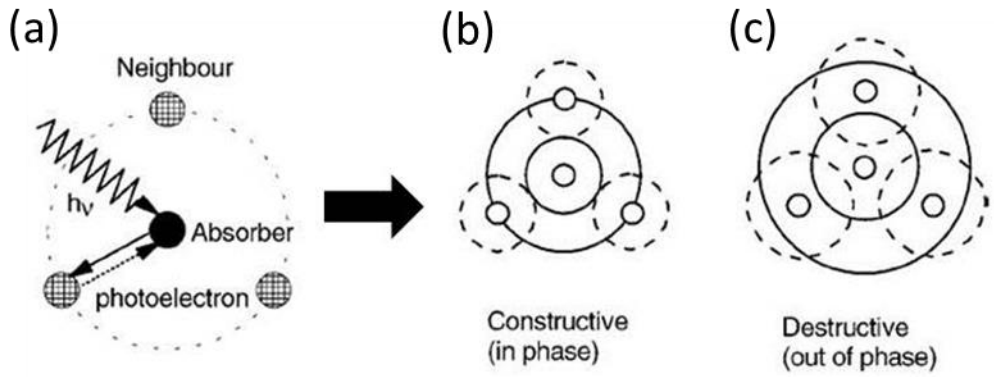

Figure 2.4: schematic of the origin of the EXAFS signal. (a) a photoelectron leaves an absorber atom upon photon absorption as a spherical wave and gets scattered back by neighbouring atoms. Depending on the phase difference, one gets (b) constructive and (c) destructive interference of the outgoing and backscattered photoelectron wave at the absorbing atom. This interference causes the maxima and minima in absorption spectra.

Figure 2.5 schematically shows possible single and multiple scattering events [28]:

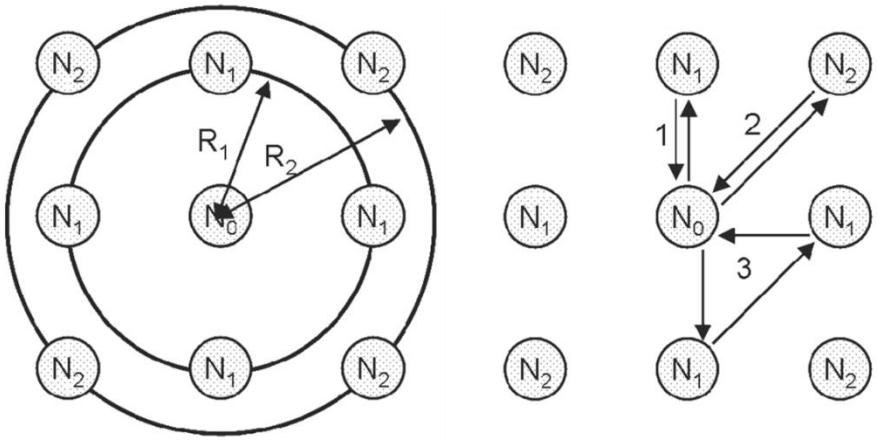

Figure 2.5: schematic of possible single and multiple scattering events. “N0”, “N1” and “N2” represent the absorber atom and atoms in the first and second shell around it, “R0”and “R1” stand for their respective distances to the absorber atom, “1” and “2” indicate single scattering paths and a possible triangular multiple scattering path (“3”).

Multiple scattering paths usually have a minor contribution to an EXAFS spectrum unless the scattering angle is close to 180° ("forward scattering", not shown in Figure 2.5). In this case multiple scatterings paths can have relative intensities higher than single scattering ones (cf. Figure A7). To get information about number, distance and kind of atoms surrounding absorber atoms one has to separate the EXAFS part of a XAFS spectrum from the rest (contributions that are and are not caused by interference effects). This is the idea behind the EXAFS function, which is extracted from experimental data according to [27]:

$$\chi(E) = \frac{\mu(E) - \mu_0(E)}{\Delta\mu_0(E)}$$

χ	EXAFS signal
μ	linear absorption coefficient (experimental)
μ_0	linear absorption coefficient (theoretical)
$\Delta\mu_0$	edge jump

In words: the signal one would get from embedded absorber atoms if the interaction of the photoelectron wave with their neighbours could be turned off is subtracted from the data. This difference is then normalized by the edge jump. Every spectrum, even of the same sample, will have its own edge jump that depends on sample- and setup-related parameters. This is explained in greater detail in the Appendix (chapter A 1.1). Because EXAFS theory makes use of the wave nature of electromagnetic radiation, energy is converted into wave numbers, which are defined on a relative scale because EXAFS features are independent from the edge under investigation [28] (rearranged):

$$k\left[\text{Å}^{-1}\right] = \sqrt{\frac{2m_e}{\hbar^2} \cdot \left(E_{ph} - E_0 + \Delta E_0\right)}\left[all\ three\ energies\ in\ eV\right]$$

k	wave number of the photoelectron wave
m_e	electron rest mass
$\hbar$	reduced Planck constant
E_{ph}	incoming photon energy
E_0	binding/ionization energy of the core electron that gets excited into the continuum
ΔE_0	parameter to align the experimental and theoretical binding/ionization energy

It should be noted that the ionization energy cannot be "seen" in an absorption spectrum since the transition from Rydberg states to the continuum is continuous. Ionization does not cause a feature that stands out. To enable comparisons between spectra several approaches were

proposed to determine an “E0”. The most common approach, and the one exclusively applied in this thesis, is the “inflection point method”. Here one sets E0 in the inflection point of the sharp rise in an absorption spectrum determined by the maximum of the first derivative. To gain information an EXAFS spectrum extracted in such a way is fitted using the EXAFS equation, which is described here in a simplified manner (modified from [29]). As mentioned before, an EXAFS spectrum is caused by photoelectrons leaving their absorber atoms as spherical waves, getting scattered back by neighbouring atoms and returning to the absorber atoms (again as a spherical waves). An EXAFS spectrum can thus be described by a sum of sine waves with an amplitude $A_j(k)$ and a phase $\Phi_j(k)$:

$$\chi(k) = \sum_j A_j\,(k)\sin\left(\Phi_j(k)\right)$$

- $\sum_j \ldots$

The sum goes over coordination shells defined as atoms of the same element at about the same distance from the absorbing atoms. Alternatively one can think of it as the sum over all single scattering paths. Multiple scattering paths can be expressed as linear combinations thereof.

The amplitude $A_j(k)$ is a product of the following factors:

$$A_j(k) = N_j \cdot \frac{1}{kR_j^2} \cdot S_0^2 \cdot f_j(k) \cdot e^{-2\sigma_j^2 k^2} \cdot e^{-\frac{2R_j}{\lambda_j(k)}}$$

- N_j

For single scattering paths this represents the number of atoms in a shell. For multiple scattering it stands for the number of degenerate (= symmetrically equivalent) paths.

- $\frac{1}{kR_j^2}$

This factor constitutes the intensity decrease of the outgoing and backscattered (spherical) photoelectron waves.

- S_0^2: amplitude reduction factor

This factor takes into account the relaxation of the N-1 electrons (all electrons of the absorber atoms minus the photoelectron = “passive”) and additional excitation processes. Even though it is slightly energy-dependant it is commonly set constant and determined by the fit of a reference sample due to the correlation with the N_j parameter.

– $f_j(k)$: backscattering amplitude

The backscattering amplitude and phase constitute the backscattering properties of atoms surrounding absorber atoms. As can be seen in Figure 2.6a and b both are strongly energy- and element-dependant [27]:

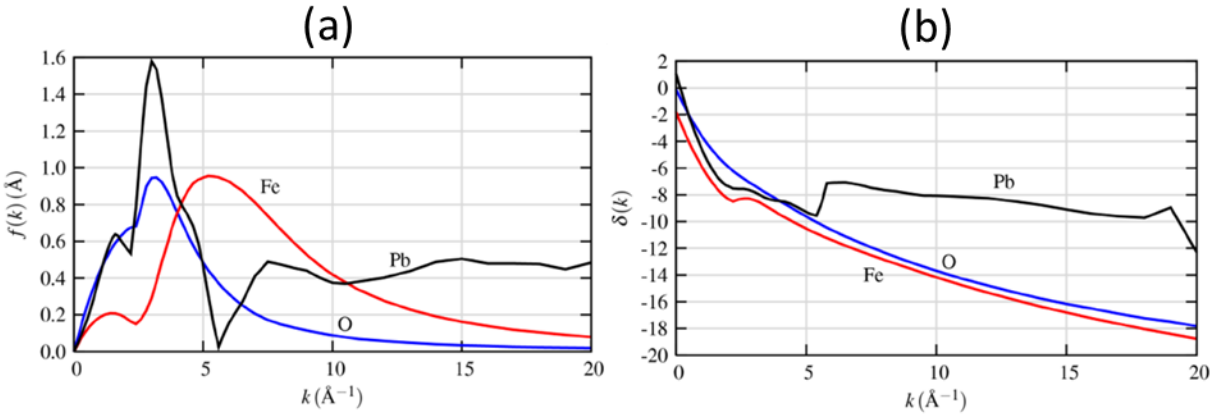

Figure 2.6: backscattering (a) amplitude and (b) phase of various elements

– σ_j^2: mean-square displacement parameter

This factor accounts for structural (*e.g.* due to vacancies) and dynamic (thermal) disorder around absorbing atoms relative to their equilibrium position. In the above written form a Gaussian distribution is implemented but it can be modified to account for a more complex behaviour, for instance in highly disordered systems.

– $\lambda_j(k)$: mean free path

This parameter accounts for both the finite life time of the core hole and the inelastic scattering of the photoelectron waves.

The phase factor $\phi_j(k)$ takes into account the phase difference between the outgoing and backscattered photoelectron waves and can be rewritten as:

$$\sin(\phi_j(k)) = \sin(2kR_j - \delta_j(k))$$

– $2kR_j$

This factor is the main reason why an absorber atom-neighbour distance can be derived from an EXAFS spectrum. It “can be thought of as being related to the time for the electron to travel to the neighboring atom and return” [29]. This time gets shorter due to the influence of the absorber and neighbouring atoms on the photoelectrons causing a phase shift:

– $\delta_j(k) = 2\delta_{absorber}(k) + 2\delta_{j,\,scatterer}(k)$

Absorber atoms and backscattering atoms both contribute to the total phase shift. The former appears twice because photoelectrons experience the potential of absorber atoms twice (upon leaving and returning). The dependency on the wavenumber k of the backscattering amplitude

and phase is the reason why the kind(s) of neighbouring atom(s) can be determined from an EXAFS spectrum with an estimated accuracy of Z±5 [27]. Nowadays, the mean free path and both backscattering parameters are calculated *ab initio* rather than experimentally determined.

– R_j

This parameter represents the absorber atom-neighbour distance. In a fit program this parameter is implemented as R_m + ΔR whereas "R_m" is taken from the respective structural model and "ΔR" is the actual fit parameter.

It should be noted that the actual EXAFS equation is complex as can be seen in the following (modified from [30]):

$$\chi(k) = \sum_j Im[N_j \cdot \frac{1}{2kR_j^2} \cdot S_0^2 \cdot f_j(k) \cdot \mathrm{e}^{i\left(2kR_j + \delta_j(k)\right)} \cdot e^{-2\sigma_j^2 k^2} \cdot e^{-\frac{2R_j}{\lambda_j(k)}}$$

For a more detailed, quantum-mechanical, derivation of the EXAFS equation via the Green's formalism see *e.g.* [31].

The great accomplishment of the EXAFS equation is that it describes the EXAFS signal as a sum of sine waves. It is this property that makes this technique so powerful since these sine waves (representing contributions from different shells) can be separated by applying a Fourier transform. Information like the number, (mean) distance and kind of atoms surrounding absorber atoms as well as their structural (dis)order can now be derived from an EXAFS spectrum - under optimal conditions up to the fourth shell. In the case of nanoparticles, binding partners like metals in alloys, adsorbates or supports can be studied.

3. Experiment

3.1. Structure of a beamline & standard XAFS experiment

Figure 3.1 schematically shows the DCM bending magnet beamline at the CAMD synchrotron radiation facility (Baton Rouge, LA, USA) [32]. It was chosen because it has a structure very similar to the IDEAS bending magnet beamline at the CLS synchrotron radiation facility (Saskatoon, Canada) on which most of the results presented in this thesis were collected.

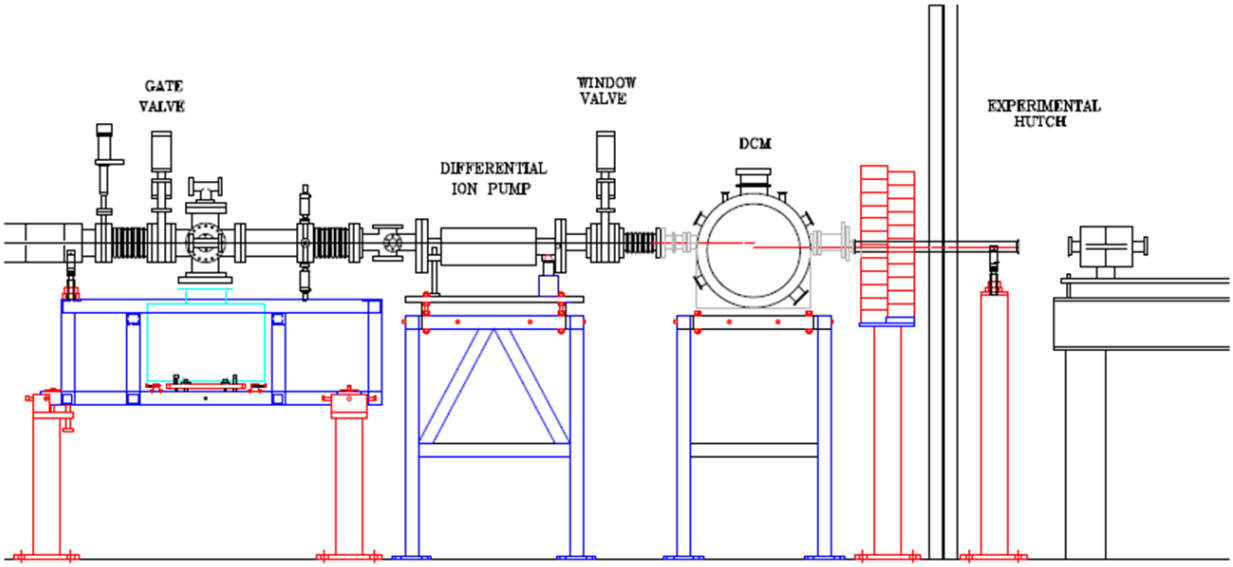

Figure 3.1: schematic of the DCM bending magnet beamline at the CAMD synchrotron radiation facility (Baton Rouge, LA, USA)

The key components are:

- valves

To close off certain sections of the beamline in case of vacuum problems

- slits (here not shown, between gate valve and differential ion pump which enables a "windowless […] transition between an ultra-high […] to high vacuum […]" [33]

To truncate the beam horizontally and vertically. In this thesis they were applied for two reasons. Firstly, to remove the beam's low-energy components (to reduce the heat load on the first monochromator crystal). Secondly, in the reduction/oxidation experiments, to make sure the beam enters and exits the sample chamber without hitting anything but the sample.

- pumps

To provide different kinds of vacua for different sections

– monochromator (here: Lemonnier-type DCM = double crystal monochromator, [34])

Monochromators are indispensable in a standard XAFS experiment because bending magnets and wiggler produce continuous spectra of radiation at once. In order to pick a desired wavelength/energy out of these spectra one varies the angle between the incident beam and a first monochromator crystal. From this angle the wavelength/energy can be calculated using Bragg's law:

$$n\lambda = 2d\sin\theta \rightarrow \frac{1}{\lambda} = \frac{n}{2d\sin\theta} \rightarrow \left(since\ E = \frac{h\cdot c}{\lambda}\right) E = \frac{nhc}{2d\sin\theta}$$

n	order of the reflection (1 = fundamental, 2 = 1st harmonic etc.)
λ	wavelength reflected at the Bragg angle
d	interplanar spacing of the monochromator crystal that's parallel to the surface
Θ	Bragg angle (angle between the wave vector and the crystal surface)
E	energy reflected at the Bragg angle
h	Planck constant
c	speed of light (in vacuum)

One problem that arises when using crystal monochromators is that not only the desired wavelength but also the harmonics (λ/2, λ/3 etc.) are being reflected at the same angle. Since harmonics have higher photon energies than the fundamental, they are attenuated less by a given material (cf. Figure 2.1). Contributions of higher harmonics thus distort a XAFS spectrum. To minimize that effect one can "detune" the second monochromator crystal, *i.e.* tilt it slightly out of its optimum reflecting position. This works because, when going from the fundamental energy to the 1st, 2nd, etc. harmonic, the rocking curves become narrower and shifted (rocking curves measure the angular dependence of the reflectivity in the vicinity of the Bragg angle). Detuning decreases the reflectivity of the fundamental wavelength but the one of all harmonics to a much greater extent - at the expense of energy resolution [35]. The effect of detuning is shown in Figure 3.2 for a Si(111) crystal pair and the rocking curves of the fundamental energy and 3rd harmonic (the second one cannot be observed due to systematic extinction) for a detuning of 3.5arcsec [28]. Numbers in brackets are Miller indices and refer to a certain cut meaning that the respective lattice plane is parallel to the surface.

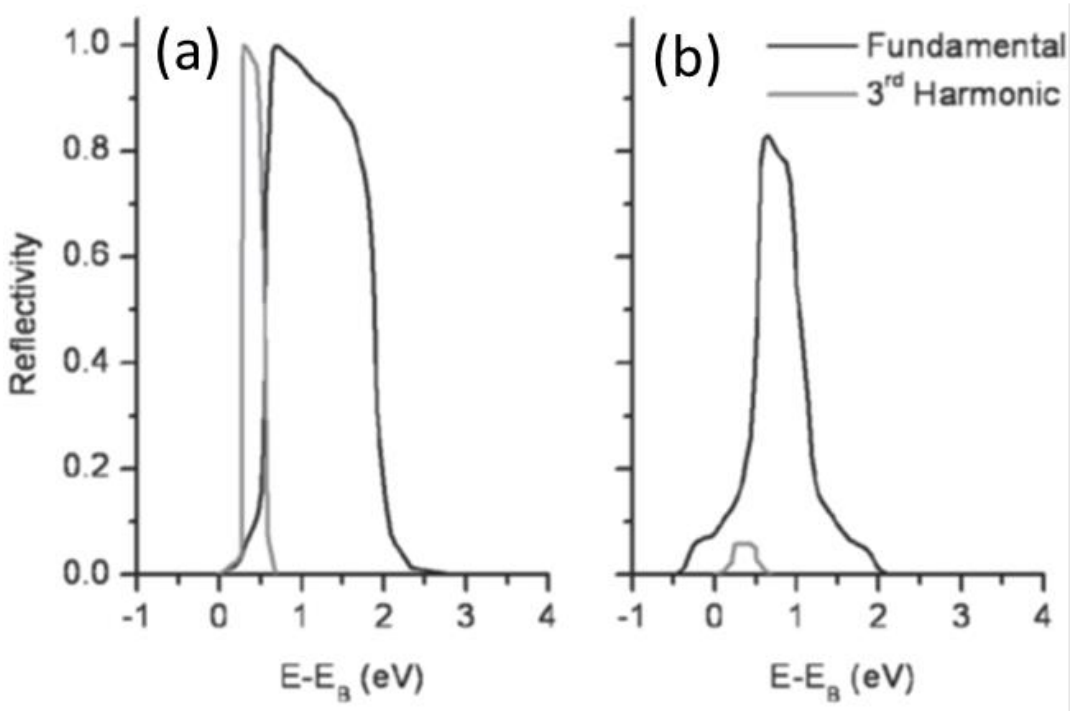

Figure 3.2: rocking curves (= reflectivity against energy) of the fundamental energy as well as the 3rd harmonic for a Si(111) crystal pair (a) at the Bragg angle and (b) detuned by 3.5arcsec (the 3rd harmonic was multiplied by 100 here). "E" and "E_B" refer to the actual photon energy and the one according to Bragg's law.

The second monochromator crystal reflects the beam horizontally. Its angle is changed in accordance with the angle of the first crystal to keep the position of the beam reflected onto the sample stable. The second crystal therefore additionally moves on a metal rail.

At IDEAS Bragg angles between 15-65° can be realized. For a desired energy range a crystal pair with a proper interplanar spacing has to be chosen.

The monochromatic beam now enters the so-called "experimental hutch" in which experiments are performed. The setup for a standard XAFS experiment can be seen schematically in Figure 3.3 (modified from [36]):

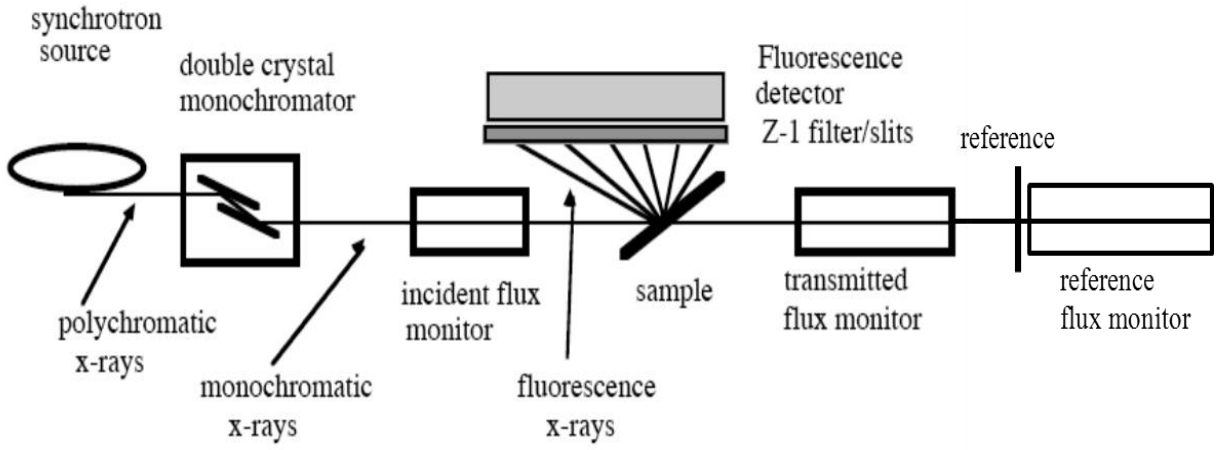

Figure 3.3: schematic setup for a standard XAFS experiment

Its components for detection are ionization chambers and a fluorescence detector. Usually there are three ionization chambers in a row with the sample between chambers 1 and 2 as well as a reference between chambers 2 and 3. Chamber 1 measures the beam intensity before the sample ("incident flux monitor"), chamber 2 the one after (= before the reference, "transmitted flux monitor") and chamber 3 the one after the reference ("reference flux monitor"). For fluorescence detection the sample is set at a 45° angle to the incoming beam and a fluorescence detector is placed at a 45° angle to the sample, perpendicular to the beam. This setup minimizes the radiation being scattered off a sample because synchrotron radiation is linearly polarized in the plane of the electron orbit. This causes electrons in a sample to be accelerated perpendicularly to the direction of the beam. Emission of fluorescence photons is isotropic but scattering is angle-dependent and is zero in the direction of acceleration. A filter can optionally be put in front of a fluorescence detector to absorb scattered radiation. The best choice is a Z-1 filter. "Z-1" hereby refers to the fact that this is most successful if the atomic number Z of the filter is one below the element whose fluorescence emission line is collected. A disadvantage of a filter is that it absorbs photons coming from the sample, which again creates fluorescence photons. To stop these from getting to the detector so-called Soller slits are put in between the filter and detector. These consist of a fan of thin metal blades pointing to the sample.

X-ray absorption experiments can be performed directly in transmission by measuring the beam intensity before and after the sample according to the (rearranged) Beer-Lambert law:

$$\mu d = ln\left(\frac{I_0}{I}\right)$$

They can also be performed indirectly by measuring fluorescence photons or Auger electrons:

$$\mu d \sim \frac{I_f}{I_0}\ (fluorescence\ photons) \qquad \mu d \sim \frac{I_e}{I_0}\ (Auger\ electrons)$$

"I_f" and "I_e" hereby stand for the fluorescence and electron counts and "I_0" again for the beam intensity before interaction with a sample, respectively. Measuring the fluorescence yield of a sample makes XAFS sensitive to concentrations in the ppm range yet susceptible to self-absorption. Measuring the electron yield makes it surface-sensitive but requires (ultra) high-vacuum conditions.

Some experiments were conducted on the HXMA wiggler beamline also at the CLS. Differences to the IDEAS beamline regarding the setup at this beamline are given in the experimental details section below.

3.2. Sample syntheses

Since some samples characterized in this thesis were synthesized wet-chemically and some via pulsed laser ablation the former will be addressed as “wet-chemical samples” and the latter as “PLAL samples” henceforth. Two different methods were applied to synthesize NPs wet-chemically. The method used for samples characterized in the first two parts of this thesis is described in the following: the Pt catalyst was synthesized with a microwave assisted polyol method. Decomposition products of polyols hereby act as reducing agents for metal precursors as well as stabilizers while microwaves significantly speed up the process [37]. Doped TiO_2 supports were synthesized via an acidic catalyzed thermal hydrolysis process. The two carbon black supports “KB” (Ketjenblack EC-600JD by AkzoNobel [21]) and “TKKE” (E-type carbon black by Tanaka Kikinzoku International (America) Inc.) are commercially available. For deposition solutions of catalyst and supports were mixed. Details about the synthesis as well as the deposition process can be found in the supporting info of [38]. The TiO_2 modifications anatase and rutile (both Sigma Aldrich) as well as Ta_2O_5 (Alfa Aesar) were measured as references.

PLAL samples in the third part of this thesis were synthesized in H_2O. As mentioned in the introduction, a higher surface/bulk ratio equals a higher sensitivity for what happens on particles’ surfaces in a XAFS spectrum. To improve that effect particles >10nm were removed by centrifugation prior to the measurements (Hettich320 centrifuge, 5000rpm, 14h). Three samples were prepared: Pt NPs in H_2O (Milli-Q, Millipore), in 0.1mM sodium citrate (Sigma Aldrich), and in 0.1mM sodium phosphate buffer (pH 7, Sigma Aldrich). The sodium citrate and sodium phosphate buffer were added *ex situ* (after particle formation), to make sure that the Pt NPs in all three samples are of uniform size. A 2wt% Pt NP sample supported on commercial anatase NPs (Hombikat Type II, Sachtleben [39]) was prepared. Details about the synthesis as well as the deposition process can be found in [22].

Wet-chemical samples in the third part of this thesis were synthesized in ethylene glycol whose oxidation products act as a stabilizer; no additional stabilizer was added. More information about the synthesis procedure can be found in [40].

Wet-chemical samples were provided by the NRC (National Research Council) Canada; PLAL samples by the CENIDE (Center for Nanointegration Duisburg-Essen, Germany). All wet-chemical and PLAL samples characterized in this thesis are summarized in Table 3.1 (references excluded). For simplicity they are arranged according to the part of the thesis in which they appear:

Table 3.1: summary of samples ("hybrid" refers to the two constituents TiO_2 and C being present next to each other while "core-shell" implies that C is covered by TiO_2 (as confirmed by TEM images). "red./ox." means that these samples were chosen for the reduction/oxidation experiments.)

sample	abbreviation	group
PART ONE		
$(0.04Ta0.06Nb0.90Ti)O_2$	4TiO2	wet-chemical
85wt% $(0.04Ta0.06Nb0.90Ti)O_2$ + 15wt% C(KB), hybrid	4TiO2+KB	wet-chemical
$(0.04Ta0.06Nb0.90Ti)O_2$ + C(KB), core-shell	4TiO2+KB2	wet-chemical
20wt% Pt supported on $(0.04Ta0.06Nb0.90Ti)O_2$	4TiO2+Pt	wet-chemical
70wt% $(0.04Ta0.06Nb0.90Ti)O_2$ + 30wt% C(TKKE)	4TiO2+TKKE	wet-chemical
PART TWO		
20wt% (0.62Pt0.38Pd) supported on 25wt% $(0.01Ta0.03Nb0.96Ti)O_2$ + 75wt% C(TKKE)	PtPd_1TiO2+TKKE (red./ox.)	wet-chemical
20wt% (0.62Pt0.38Pd) supported on 70wt% $(0.04Ta0.06Nb0.90Ti)O_2$ + 30wt% C(TKKE)	PtPd_4TiO2+TKKE (red./ox.)	wet-chemical
PART THREE		
Pt in H_2O	Pt in H2O	PLAL
Pt in 0.1mM sodium citrate	Pt in citrate	PLAL
Pt in 0.1mM sodium phosphate buffer	Pt in phosphate	PLAL
2wt% Pt supported onTiO_2	Pt on TiO2	PLAL
Pt in ethylene glycol	Pt in ethylene glycol	wet-chemical
20wt% Pt supported on $(0.01Ta0.03Nb0.96Ti)O_2$	Pt on 1TiO2	wet-chemical

Samples characterized in this thesis are addressed by their respective abbreviation and group.

3.3. Experimental details

Wet-chemical samples in the first part were powdered and rubbed on a Quartz fiber membrane filter (EMD Millipore) for the measurements.

Samples chosen for the reduction/oxidation experiments were rubbed onto the same filters which were specifically chosen for the conditions samples were subjected to (temperatures up to 300°C and reducing gas atmosphere). Filters were then put into the sample holder on the opposite side of the heating wire (Thermocoax) as can be seen in Figure 3.4a [41], marked by an arrow ("h.w."). A K-type thermocouple (Omega) was screwed into the top of the sample holder and bent towards the sample as close as possible. The sample holder was then placed in a steel cylinder (Figure 3.4b, [41]) which can be water-cooled. Both parts, the sample holder and steel cylinder, constitute a modified Lytle cell. This cell was then put into a sample chamber built in-house. The sample chamber was made from a NW100 5-way cross modified

such that the Lytle cell sits at the right height so that the sample is hit by the beam. Its components are described in the following (numbers correspond to those in Figure 3.4c):

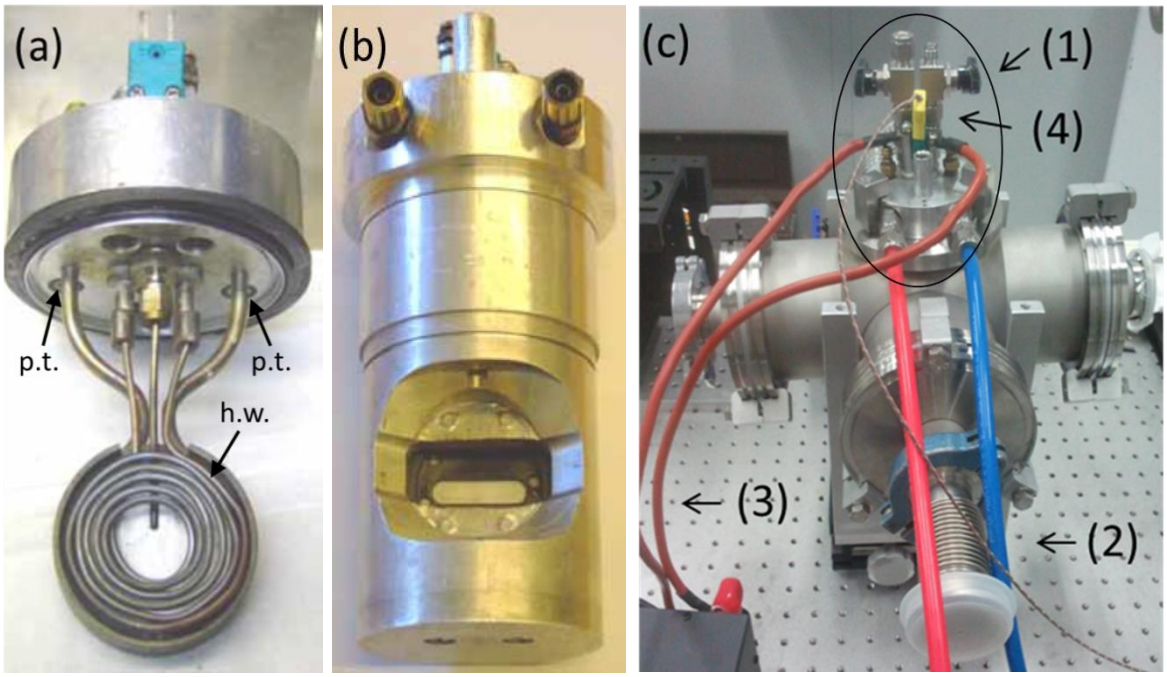

Figure 3.4: equipment for reduction measurements: (a), (b) sample holder without and with steel cylinder. “p.t.” stands for “plastic tube” which was used to connect the sample holder and steel cylinder in case of water cooling. “h.w.” represents the heating wire. Samples were placed on the opposite side. (c) Sample chamber: (1) gas in-/outlet, (2) tubes for water-cooling, (3) wires for heating wire power supply, (4) connection for thermocouple. The ellipse marks the modified Lytle cell.

(1) gas in-/outlet

(2) tubes for water-cooling: if the temperatures of the heating wire exceeded 100°C the steel cylinder was cooled with water from a chiller to protect sample chamber components such as Kapton windows. To do so, it proved necessary to connect the two pieces of the sample chamber with plastic tubes (as marked “p.t.” in Figure 3.4a).

(3) wires that attach the heating wire to the power supply whose settings showed to result in not very well reproducible temperatures. The most likely reason is that the thermocouple was not firmly attached to the samples but just brought into contact. Roughly: 10 and 65W gave temperatures of 70 and 200°C, respectively.

(4) feed-through for thermocouple

Experiments were conducted in a temperature range from room temperature up to 300°C. For reduction a 3.7% H_2 gas mixture with He as a carrier gas (Praxair) was used. Several approaches were applied for gas delivery to the sample. They all have in common that the sample chamber was first pumped down to a pressure in the low 10^{-2}mbar range after which the pump was turned off. The approaches for gas delivery are now described in some detail in the order of increasing flowrate: (i) the gas mixture was input until ambient pressure was

achieved in the sample chamber and then turned off; (ii) a light gas flow without flowmeter was applied; (iii) a flowmeter was used and a flowrate up to its maximum of about 45ml/min, which is higher than [42] and almost equal to the rate f in literature for Pt NPs [43].

The three unsupported PLAL samples were initially in liquid form. Test spectra showed a bad signal-to-noise ratio due to a low Pt concentration. To increase that concentration, 8 vials of these samples were centrifuged for up to 5min at up to 5000rpm until the Pt NPs were visible as dark spots on the walls of the vials. The respective solution was then decanted and a spatula was used to remove the Pt NPs from the walls of the vials. They were then mixed with a few drops of deionized water and poured onto filter paper for XAFS measurements. For an unknown reason no dark spots were visible for the Pt in phosphate sample so it was instead pipetted into a sample holder and sealed with Scotch tape on both sides. Pt on TiO2 was powdered and rubbed either onto a glass fiber filter for Pt LIII or Kapton tape for Ti K edge measurements. The sample Pt in ethylene glycol was present in liquid form and poured onto filter paper for the measurements. Pt on 1TiO2 was mixed with BN and placed into a sample holder with Kapton tape on both sides.

Ti K, Ta LIII, Ta LI, Nb LIII/II and Pt LIII edge XAFS spectra were recorded on the IDEAS beamline. Pt LIII edge and Nb K edge XAFS spectra were recorded on the HXMA beamline. Here, Si collimating mirrors with Rh coating were used before the monochromator.

To record transmission data two kinds of ionization chambers were used: in-house built and by Oxford. Gas mixture and pressure were chosen for an optimal signal-to-noise ratio. At all edges, except Nb LIII/II, reference foils were measured simultaneously. Most samples were measured without a sample chamber in air at ambient conditions. Exceptions were Nb LIII/II edge measurements as well as reduction/oxidation experiments. The former were conducted at such low energies that attenuation of the beam by air molecules is very strong. To improve that air at 70mbar was used in the sample chamber. For all samples and references transmission data were recorded and of samples also fluorescence data simultaneously. For fluorescence detection a Si drift (Vortex, IDEAS) or a 32 element Ge solid state detector (Canberra, HXMA) was used. The former was cooled with water using an in-house built system, the latter with liquid N_2. For Pt (all) and Ta LIII edge scans (just reduction/oxidation experiments) the fluorescence detector was capped with a collimator and wrapped in layers of tin foil to reduce low-energy fluorescence (predominantly from Ti). The dead time was kept below 20% for a reasonable correction, done automatically by software. Table 3.2 summarizes the most important experimental parameters:

Table 3.2: summary of experimental parameters (reduction/oxidation experiments are omitted. Conditions in the three ionization chambers were the same at a edges except the Ti K edge at which the 2nd/3rd ionization chamber was by Oxford filled with N_2 at ambient pressure.)

element/ edge	energy [eV]	mono crystal pair	emission line	beamline	detuned	kind/gas/pressure sample chamber	kind/gas/pressure ionization chambers
Ta LIII	9,881	Ge(220)	Ta $L_{\alpha 1,2}$	IDEAS	no	no chamber air ambient pressure	Oxford air ambient pressure
Ta LI	11,682	Ge(220)	Ta $L_{\alpha 1,2}$	IDEAS	no	no chamber air ambient pressure	Oxford air ambient pressure
Pt LIII	11,564	Ge(220)	Pt $L_{\alpha 1,2}$	IDEAS	no	no chamber air ambient pressure	Oxford air ambient pressure
Pt LIII	11,564	Si(111)	Pt $L_{\alpha 1,2}$	HXMA	to 50%	no chamber air ambient pressure	Oxford N_2 ambient pressure
Ti K	4,966	Ge(220)	Ti $K_{\alpha 1,2}$	IDEAS	to 50%	no chamber air ambient pressure	in-house built N_2 500mbar/ ambient pressure
Nb LIII	2,371	InSb(111)	Nb $L_{\alpha 1,2}$	IDEAS	to 50%	in-house built air 70mbar	in-house built air 70mbar
Nb LII	2,465	InSb(111)	Nb $L_{\alpha 1,2}$	IDEAS	to 50%	in-house built air 70mbar	in-house built air 70mbar
Nb K	18,986	Si(111)	Nb $K_{\alpha 1,2}$	HXMA	to 50%	no chamber air ambient pressure	Oxford N_2 ambient pressure

Table 3.3, Table 3.4, and Table 3.5 summarize the scan parameters of all experiments done in this thesis divided into the three parts. Energies are given relative to the respective edge energies as determined by the inflection point method.

Table 3.3: scan parameters used in part one (investigating the impact of Ta-/Nb- co-doping PEM fuel cell supports. “f” stands for “function”. The intensity and thus signal-to-noise ratio of the EXAFS signal decreases gradually for increasing energy. To improve that ratio the integration time in the post-edge region was gradually increased from the given value to a maximum of10s using an empirical function.)

Ti K edge			**Ta LIII edge**		
pre-edge region	energy range [eV]	-200 to -30	**pre-edge region**	energy range [eV]	-200 to -30
	step size [eV]	10		step size [eV]	10
	integration time [s]	1		integration time [s]	1
edge region	energy range [eV]	-30 to +40	**edge region**	energy range [eV]	-30 to +40
	step size [eV]	0.75		step size [eV]	0.75
	integration time [s]	1		integration time [s]	1
post-edge region	energy range	+40eV to 9Å^{-1}	**post-edge region**	energy range	+40eV to 9Å^{-1}
	step size [eV]	0.1Å^{-1}		step size [eV]	0.1Å^{-1}
	integration time [s]	1 (f)		integration time [s]	1 (f)
Nb LIII/II edge			**Nb K edge**		
pre-edge region	energy range [eV]	-70 to -30	**pre-edge region**	energy range [eV]	-200 to -30
	step size [eV]	10		step size [eV]	10
	integration time [s]	3		integration time [s]	1
edge region	energy range [eV]	-30 to +40	**edge region**	energy range [eV]	-30 to +40
	step size [eV]	1		step size [eV]	0.25
	integration time [s]	3		integration time [s]	1
post-edge region	energy range	+40eV to 8Å^{-1}	**post-edge region**	energy range	+40eV to 14Å^{-1}
	step size [eV]	0.05Å^{-1}		step size [eV]	0.05Å^{-1}
	integration time [s]	3 (f)		integration time [s]	1 (f)

Table 3.4: scan parameters used in part two (reduction/oxidation behaviour of PEM fuel cell catalyst-support units. “f” is explained in the caption of Table 3.3)

Pt LIII edge		
pre-edge region	energy range [eV]	-200 to -30
	step size [eV]	10
	integration time [s]	3
edge region	energy range [eV]	-30 to +40
	step size [eV]	1
	integration time [s]	3
post-edge region	energy range	+40eV to 9Å^{-1}
	step size [eV]	0.1Å^{-1}
	integration time [s]	3 (f)

Ta LIII edge		
pre-edge region	energy range [eV]	-200 to -30
	step size [eV]	10
	integration time [s]	2
edge region	energy range [eV]	-30 to +40
	step size [eV]	1
	integration time [s]	2
post-edge region	energy range	+40eV to 9Å^{-1}
	step size [eV]	0.1Å^{-1}
	integration time [s]	2 (f)

Ti K edge		
pre-edge region	energy range [eV]	-200 to -30
	step size [eV]	10
	integration time [s]	1
edge region	energy range [eV]	-30 to +40
	step size [eV]	0.5
	integration time [s]	1
post-edge region	energy range	+40eV to 9Å^{-1}
	step size [eV]	0.05Å^{-1}
	integration time [s]	3 (f)

Table 3.5: scan parameters used in part three (characterization of un- and TiO_2-supported Pt nanoparticles synthesized via pulsed laser ablation in liquid. "f" is explained in the caption of Table 3.3)

Pt LIII edge			**Ti K edge**		
pre-edge region	energy range [eV]	-200 to -30	**pre-edge region**	energy range [eV]	-200 to -30
	step size [eV]	10		step size [eV]	10
	integration time [s]	1		integration time [s]	1
edge region	energy range [eV]	-30 to +40	**edge region**	energy range [eV]	-30 to +40
	step size [eV]	1		step size [eV]	0.75
	integration time [s]	2		integration time [s]	1
post-edge region	energy range	+40eV to $9Å^{-1}$	**post-edge region**	energy range	+40eV to $9Å^{-1}$
	step size [eV]	$0.1Å^{-1}$		step size [eV]	$0.05Å^{-1}$
	integration time [s]	2 (f)		integration time [s]	2 (f)

All recorded spectra were processed using ATHENA (version 0.8.061) from the IFEFFIT software package [44], [45]. Spectra were first energy-calibrated by determining the threshold energy E0 of the respective reference spectrum (inflection point method), whose values were taken from [46]. These were then aligned to the respective first one of the series. A linear background was subtracted from all spectra and normalization done using a second-order polynomial. To increase the signal-to-noise ratio several spectra of the same sample were averaged. The detailed procedure can be the found in the Appendix (chapter A 1.1).

For Ta LIII and Nb K edge EXAFS analysis the program WinXAS (FEFF7 code) was used [47]. The structural file for rutile TiO_2 was taken from [48] (COD ID 9015662).

For Pt LIII edge EXAFS data analysis the program ARTEMIS from the IFEFFIT software package was used (version 0.8.014). EXAFS data were extracted using ATHENA in all cases and the approach described in chapter 2: applying the EXAFS function and converting energy into wavenumber. Values for the amplitude reduction factor S_0^2 were obtained by fitting the 1st shell of the respective reference foil. This value was then kept fixed for subsequent fits of sample EXAFS data. The structural file for Pt was taken from [49]. A Hanning window with a dk value of 1.0 was used for all Pt data fits. They had a k^n-weight of n = 1 and 3 simultaneously. One ΔE parameter was fitted for all paths of the respective data set (as shown *e.g.* in [30]). The detailed procedure can be the found in the Appendix (chapter A 1.2). For more information about XANES and EXAFS data handling as well as the IFEFFIT software package see [44], [45].

Fits were done in R-space to the 2nd shell with one Pt-N as well as one Pt-Pt path. The former was used instead of a Pt-O path because this resulted in FEFF returning an error message meaning that calculating scattering paths for a Pt foil structure worked with N atoms in the 1st shell but not with O atoms. Using N atoms and interpreting them as O atoms is however reasonable, since both have almost identical backscattering properties. To reduce the number of fit parameters one mean-square displacement parameter σ^2 was fitted for each path, kept fixed and the fit repeated. This resulted in a total of 6 fit parameters (two numbers of next neighbours N, two distances from absorber atoms to the respective shell R, one ΔE for both paths and one third order cumulant-expansion parameter σ^3 for the Pt-N path to account for its asymmetry).

4. Results

All spectra were measured in fluorescence unless specified otherwise. Differences between spectra are thus not caused by the different recording techniques transmission and fluorescence. Table 3.1 summarizes samples and their respective abbreviations.

4.1. Doping of PEM fuel cell supports

In this chapter the impact of Ta-/Nb- co-doping a TiO_2 nano-support was studied. Starting with a single support, two C-TiO_2 hybrid and one core-shell support as well as one Pt-TiO_2 catalyst-support unit were characterized. The goal was to determine how (in which chemical state) and where (at which crystallographic position(s)) dopants are incorporated into the respective TiO_2 host structure and how that impacts these structures. Additionally, a possible catalyst-dopant interaction was examined.

4.1.1. General information

In this subchapter general information is given that aids understanding the following results.
The ground state electron configurations of gaseous neutral Ti/Ta/Nb atoms are [50]:

- Ti: [Ar] $3d^2$ $4s^2$
- Ta: [Xe] $4f^{14}$ $5d^3$ $6s^2$
- Nb: [Kr] $4d^4$ $5s^1$

Ti K, Ta LI and Nb K edge whitelines are caused by transitions to unoccupied p-states, which are empty for these three elements. There are now two reasons why they are partially filled in my samples. (i) all samples are solids: this has the consequence that orbitals overlap to form bands which causes charge redistribution from Ta 5d/Nb 4d to Ta 6p/Nb 5p orbitals. (ii) all samples are oxides: this causes a charge transfer between Ta 5d/Nb 4d (Ta 6p/Nb 5p) and O 2p orbitals.
At the Ti K edge there are 3 (rutile) and 2 (anatase) whiteline peaks just like at the Ta LI and Nb K edge. There is no agreement in literature yet about their origin, but it is generally accepted that these peaks area caused by shake-down processes [51] and transitions to split p-levels [52].

As can be seen in Table 3.1, TiO_2 supports were co-doped with Ta and Nb. The idea behind that was to replace tetravalent Ti with pentavalent Ta/Nb in the TiO_6 octahedra and thereby

provide additional electrons to increase the electric conductivity of the semiconductor TiO_2. This enhancement effect can be explained with the formation of an impurity band by these additional electrons in the band gap close to the conduction band [53]. To guarantee charge compensation either Ti^{4+} is reduced to Ti^{3+} or Ti vacancies are created.

Doping TiO_2 with pentavalent ions to enhance its electronic conductivity is not limited to electrocatalytic applications but is also used in photocatalysis [54] as well as in unrelated fields, *e.g.* for making TCOs (transparent conductive oxides) [55] or solar cells [56]. Doping TiO_2 has the additional effects of hindering grain growth and shifting the anatase-rutile phase transition to higher temperatures [57].

Both the rutile and anatase structure consist of TiO_6 octahedra which in rutile share 2 edges with adjacent octahedra and 4 in anatase as can be seen in Figure 4.1 [58]:

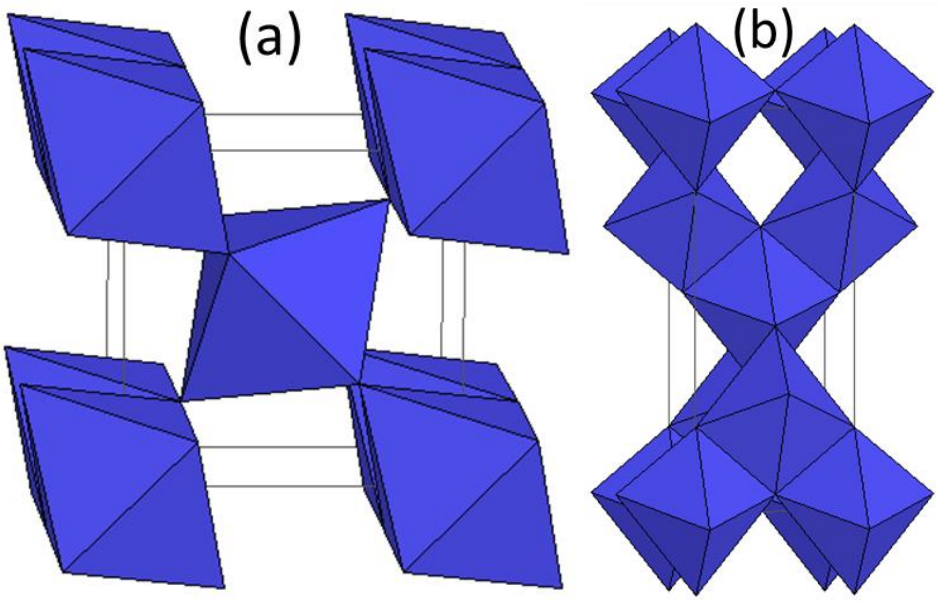

Figure 4.1: crystal structure of (a) rutile and (b) anatase. Both consist of TiO_6 octahedra. Lines mark unit cells.

What cannot be seen in above figures is that the TiO_6 octahedra in both structures are distorted meaning that the distances from the Ti atoms at the center to the 4 equatorial O atoms are about 0.03Å shorter than the ones to the 2 apical O atoms.

There are many techniques available nowadays to study doping. By means of XRD one can determine the atomic site in which doping took place as well as how and to what extent a host structure gets distorted - if it gets distorted. A disadvantage to this technique is that no information about the chemical state of a dopant is accessible from XRD data. From an FTIR (Fourier-transform infrared) spectrum one can derive binding partners and thus, for example, if dopants form cluster. Yet, no crystallographic information about the dopant or the host

structure can be acquired. Applying EDS (energy-dispersive x-ray spectroscopy) one can obtain the concentration of a dopant and its spatial distribution, but neither information about chemical state(s) nor crystallographic position(s). An application of all these techniques can be found in [56].The huge advantage of XAFS over these three other techniques to answer questions regarding doping is that one can get information about crystallographic positions as well as the chemical state of a dopant even if a host structure does not get distorted - including but not limited to concentrations in the ppm range.

4.1.2.XANES: Ti K edge

Figure 4.2 shows normalized Ti K edge XANES spectra of the five measured samples together with (a) rutile and (b) anatase (insets show pre-edge and whiteline regions, vertically offset for clarity. The former are from different scans with better resolution). Between 3 and 6 individual scans were averaged for one spectrum. Due to experimental problems with the data collection of the rutile and anatase Ti reference foils their calibration was not possible. These spectra were shifted manually to align respective features. Shifts between features of samples and references thus might come from this alignment process. The rutile and anatase spectrum also were corrected for self-absorption using ATHENA.

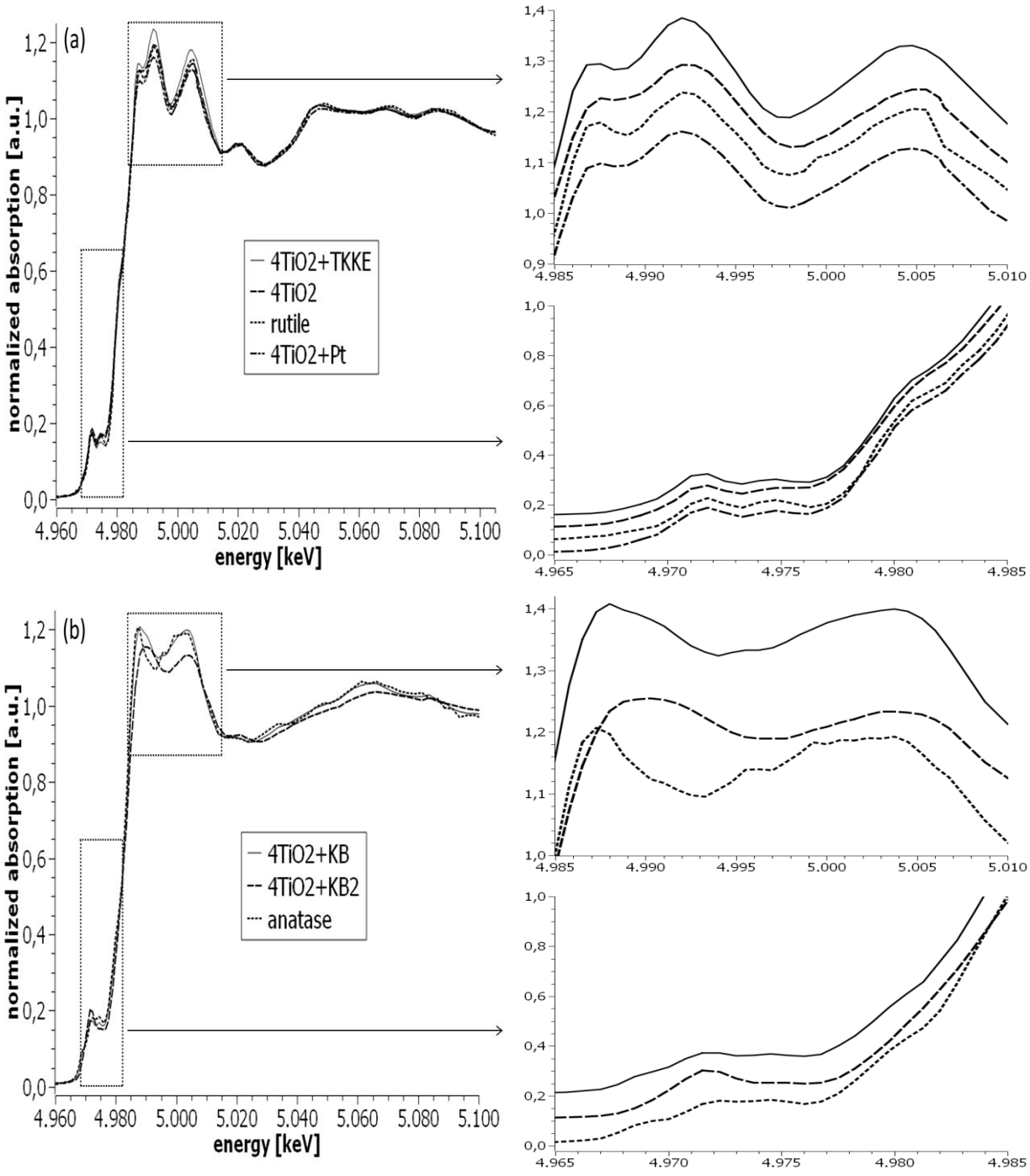

Figure 4.2: normalized Ti K edge XANES spectra of (a) rutile, 4TiO2+TKKE, 4TiO2, as well as 4TiO2+Pt and (b) 4TiO2+KB, 4TiO2+KB2, as well as anatase. Insets: pre-edge (different scans)/whiteline regions, vertically offset

The two figures above show an excellent agreement between sample and reference spectra meaning that TiO_2 is predominantly present as rutile in the samples 4TiO2+TKKE, 4TiO2 and 4TiO2+Pt and as anatase in the samples 4TiO2+KB and 4TiO2+KB2. Differences between sample and reference spectra can be explained with the incorporation of one or both dopants into the respective TiO_2 host structure and an electron transfer between Ti and C(KB), C(TKKE), as well as Pt atoms - differences due to experimental reasons neglected.

Differences in the pre-edge region between samples portrayed in Figure 4.2 can be explained with incorporation of Ta and/or Nb into the rutile structure as can be seen in Figure 4.3a and b [51], [59]:

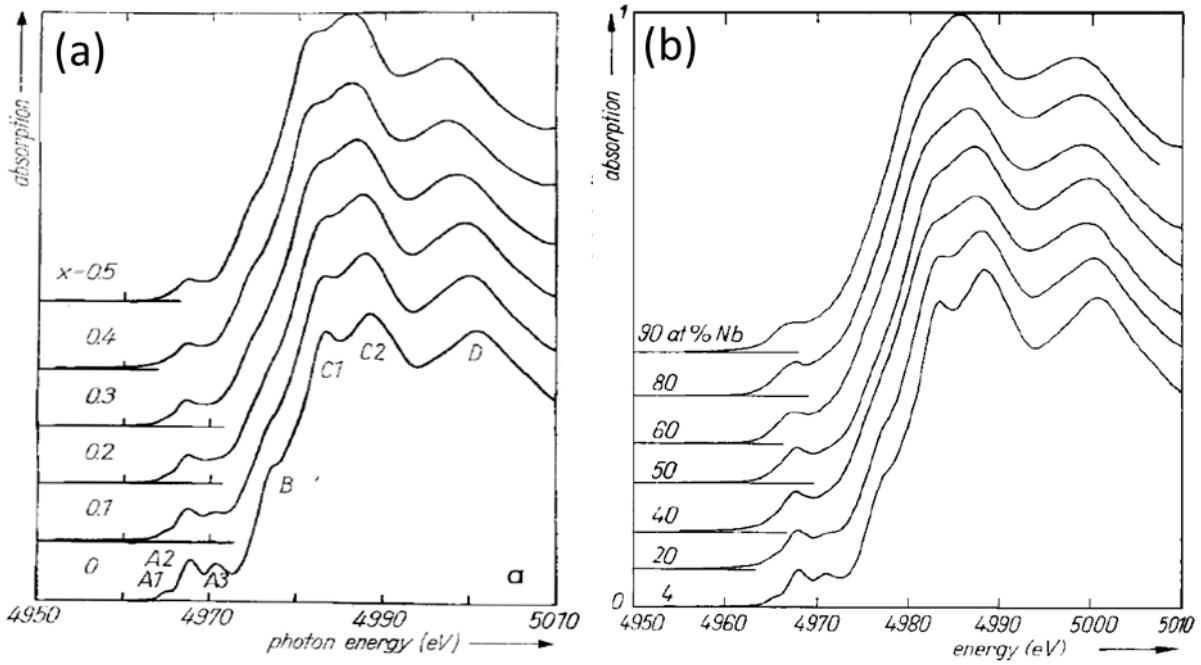

Figure 4.3: impact of (a) Ta and (b) Nb doping on rutile Ti K edge XANES spectra. Samples characterized in this thesis were doped with 4at% Ta and 6at% Nb.

Both dopants in their respective concentrations (Ta/Nb: 4/6at%) cause very similar changes in the pre-edge region: an intensity decrease of peaks A1, A2 and A3. This makes it impossible to determine whether or not both dopants were incorporated into the respective TiO_2 host structure. Yet, the extent of the intensity decrease indicates that (Figure 4.2). Based on [51] and [59] (and explanations given therein) I hypothesize that Ta-/Nb-doping in anatase has an impact on the pre-edge region of Ti K edge spectra comparable to rutile. Nowadays it is generally accepted that features A1, A3 and A2 are due to quadrupole transitions, dipole transitions, and a mixture of both, respectively [60]. According to [61], peaks A2 and A3 are strongly influenced by dipole-allowed transitions to states with Ti 3d(t2g) and 3d(eg) character ("t2g" and "eg" are the two energy levels created by crystal field splitting in octahedral coordination). As mentioned in chapter 2, pre-edge features are strongly influenced by hybridization of p-/d-states. Accordingly, doping rutile with Ta/Nb seems to impact the degree to which Ti 3d and 4p states are hybridized by distorting the TiO_6 octahedra to a greater or lesser extent. Pre-edge peak intensity differences between sample spectra can thus be explained with slightly different dopant concentrations.

Peaks in the whiteline region are due to transitions from Ti 1s to 4p states. Peak intensities depend on the unoccupied density of the latter. Intensity differences are a result of different

densities of states, which have two causes: distortion of TiO_6 octahedra (as explained in the previous section) and electron transfer between Ti and C(KB), C(TKKE), as well as Pt atoms. The 4TiO2+KB2 spectrum (core-shell sample) needs special attention because it deviates most from its reference (Figure 4.2b). There are two striking differences: (1) the intensity of the second pre-edge feature A2 (about 4,970eV) is increased whereas the intensity of the first and third feature is decreased. As explained in more detail in the previous section, the increased A2 intensity indicates the strongest degree of hybridization of Ti p-/d-states and thus distortion of the TiO_6 octahedra of all five measured samples. What "distortion" actually means is debated in the following. In [61] the impact of different kinds of distortion on the pre-edge region of rutile Ti K edge spectra was calculated. Even though the rutile structure was used as a reference in these calculations I hypothesize that the increased intensity of the 4TiO2+KB2 A2 feature comes from shorter Ti-O bonds despite its predominant anatase TiO_2 structure. This is supported by [24] "as the intensity of pre-edge peaks drops sharply with increasing bond length". The most plausible scenario is that Ti atoms are shifted out of the center of their TiO_6 octahedra. The fact that the A2 feature is more intense in the 4TiO2+KB2 than the 4TiO2+KB spectrum (cf. Figure 4.2b) is an indication that the C-TiO_2 interaction is stronger in the core-shell compared to the hybrid support. Alternatively, the increased A2 peak intensity could come from a significant rutile concentration since this feature is more pronounced in a rutile spectrum. Yet, linear combination fits done by me showed no indication of this scenario! Another aspect to consider is coordination. Farges et al. [62] determined a correlation between the position as well as intensity of the three pre-edge features at the Ti K edge in titanium oxides with coordination of Ti by O atoms. In short, a lower coordination number leads to more intense peaks at lower energies. As can be seen in the insets of Figure 4.2, a shift of the A2 feature can be seen for those samples where TiO_2 is present as anatase but not for the ones where it is present as rutile. This indicates either a smaller particle size and/or a higher degree of disorder of anatase TiO_2 particles. (2) the first whiteline peak C1 (about 4,990eV) is severely broadened compared to the anatase reference and the 4TiO2+KB spectrum despite their identical chemistry. In [63] a broadening of the whiteline peak at 4,990eV is explained with a particle size effect and an accompanied degree of disorder. The fact that the signal of the 4TiO2+KB2 spectrum decreases fastest with increasing energy indicates that TiO_2 particles have the smallest particle size in this sample. The broadening of its first whiteline peak points towards a higher degree of disorder compared to the anatase and 4TiO2+KB spectrum, which agrees with the higher pre-edge peak intensity. This conclusion is supported by spectra similar to those in Figure 4.2b ([64],

[65]) in which very small and amorphous TiO_2 with a short-range anatase-like structure were characterized, respectively.

TiO_2 is predominantly present as anatase in the two samples containing C(KB) and as rutile in the three that don't. The decreased pre-edge feature intensities strongly indicate that both dopants, Ta and Nb, were incorporated into the respective TiO_2 host structure of all five samples characterized in this work. Neither their chemical state nor crystallographic positions can be derived from Ti K edge results. Ta LIII/LI as well as Nb LIII/K edge XANES and EXAFS data were evaluated to answer these questions.

4.1.3. XANES: Ta & Nb LIII edge

Because samples that don't contain C(KB) returned similar Ta LIII edge XANES spectra as did samples that do, both groups of samples are portrayed separately in Figure 4.4 (insets show whiteline regions). This discrepancy is most likely due to TiO_2 being present as anatase in the C(KB)-containing samples and as rutile in all other ones (cf. Figure 4.2). The 4TiO2 spectrum is included in both images to show similarities and differences. 3 individual scans were averaged for one spectrum.

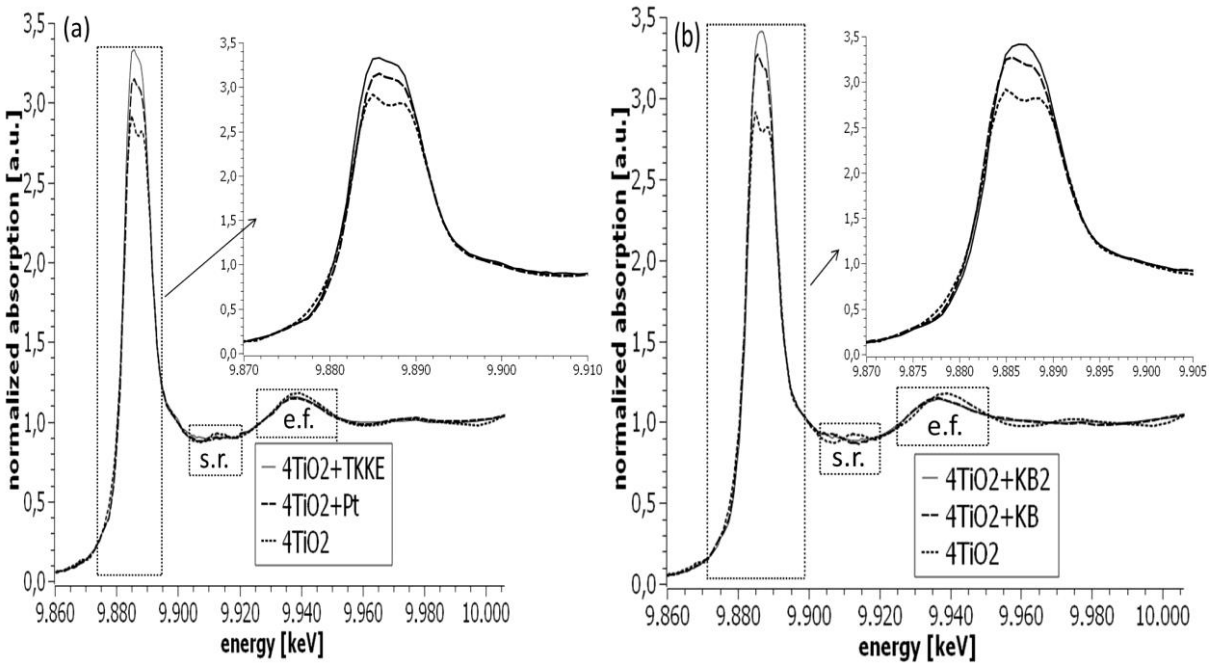

Figure 4.4: normalized Ta LIII edge XANES spectra of (a) 4TiO2+TKKE, 4TiO2+Pt as well as 4TiO2 and (b) 4TiO2+KB2, 4TiO2+KB as well as 4TiO2. "s.r." and "e.f." mark "shape resonances" and "EXAFS features", respectively. Insets: whiteline regions

This spectral resemblance between samples with and without C(KB) isn't as clear at the Nb LIII edge which is most likely due to the rather poor data quality (Figure 4.5, insets show the

whiteline regions). Due to the low energy no reference channel was recorded simultaneously for these spectra. They were aligned manually to the 4TiO2 spectrum. Between 3 and 6 individual scans were averaged for one spectrum.

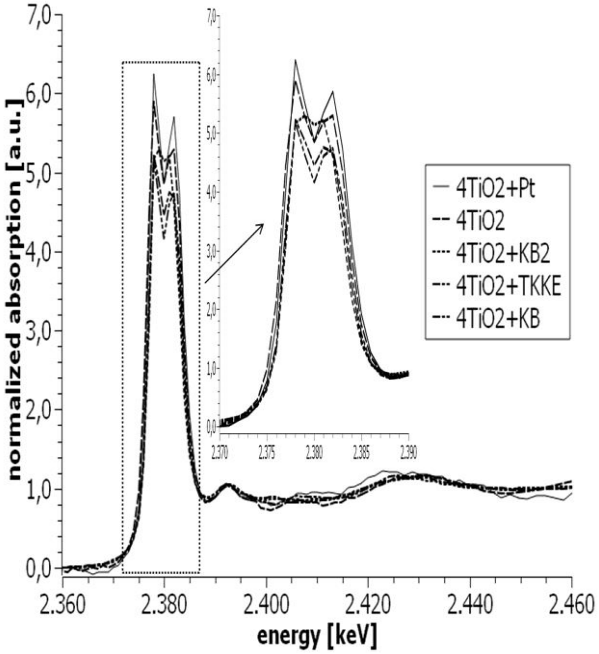

Figure 4.5: normalized Nb LIII edge XANES spectra of all five measured samples. Inset: whiteline regions

The similarity amongst the Ta/Nb LIII edge spectra strongly indicates a similar local geometric environment of Ta and Nb atoms in the five measured samples. Differences in the post-edge region can reasonably be assumed to reflect the different host structures anatase and rutile. To get more detailed information about the local geometric environment of Ta and Nb in the five measured samples the 4TiO2 spectrum is now compared to the spectra of the mineral tantalite ((Fe, Mn)(Ta, Nb)$_2$O$_6$), Ta$_2$O$_5$, and a Ta foil (Figure 4.6a) as well as LiNbO$_3$ (Figure 4.6b, both insets show the whiteline regions). The tantalite and LiNbO$_3$ spectrum were digitized from [66] and [67] using WebPlotDigitizer. Since in these references no values for the absorption were given it was chosen to be 1 at the end of the spectra. A wrong choice results in peak intensities being too small/high. Differences in peak intensities between the 4TiO2 and reference spectra might thus come from the digitization process. Spectra are vertically offset for clarity.

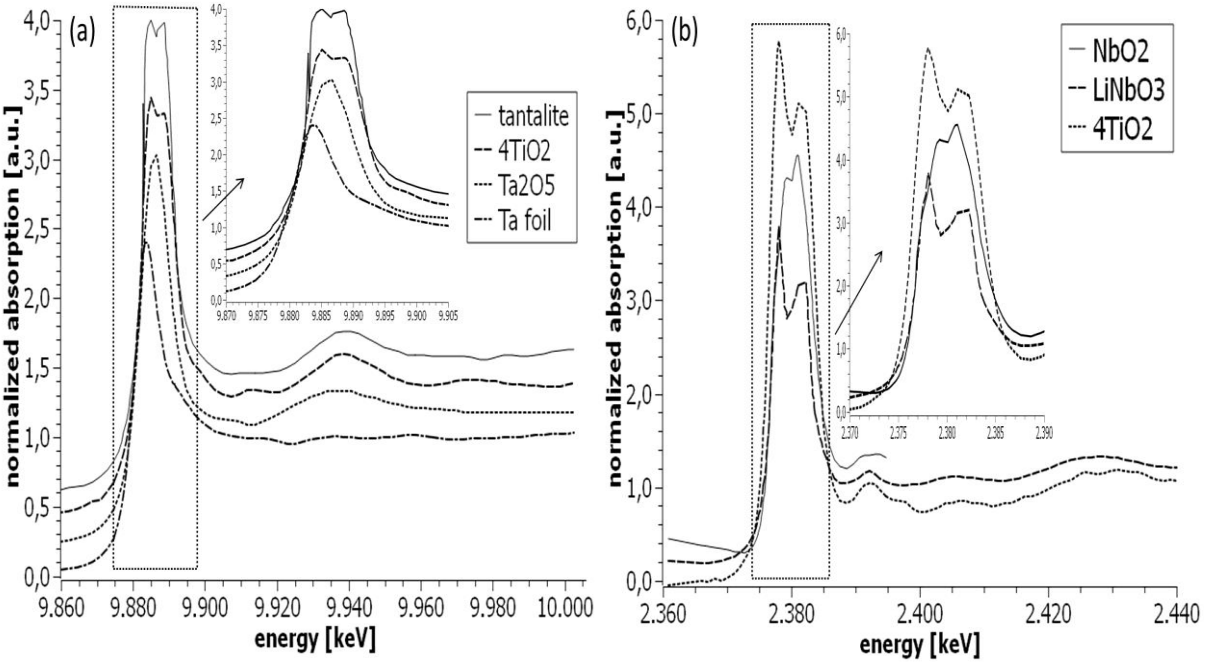

Figure 4.6: normalized Ta LIII edge XANES spectra of tantalite, 4TiO2, Ta_2O_5 as well as a Ta foil, vertically offset. Inset: whiteline regions

The 4TiO2 Ta LIII edge spectrum resembles the one of tantalite. One can thus conclude that Ta atoms in the five measured samples have a similar local geometric environment as they do in tantalite which is "6-[fold] coordinated by oxygen atoms" [66]. On the other hand, the 4TiO2 spectrum is completely different from those of the Ta foil and Ta_2O_5. This means that the Ta atoms are present neither in a metallic form (they don't form cluster) nor in the only stable oxide form. Usually, average oxidation states can be derived from edge positions due to chemical shifts (spectra shift to higher energies for higher average oxidation states). Applying this correlation did not work for the five samples measured here because the edge position for Ta_2O_5 (9,882.1eV) is well below the literature value (which, according to [68], can be calculated assuming a +1eV shift per +0.7 change in average oxidation state. Ta atoms in a Ta foil are in a ±0 oxidation state, Ta atoms in Ta_2O_5 in a +5 oxidation state. This +5 change corresponds to a shift of about +7.1eV and thus, taking into account the edge position of the Ta foil which is 9,881eV, a Ta_2O_5 edge position of 9,888.1eV). Though is it not clear what caused this deviation it is safe to assume that the same situation holds true for all sample spectra. For this reason no average oxidation states were derived from edge positions at the Ta LIII edge. The 4TiO2 Nb LIII edge spectrum is similar to the one of $LiNbO_3$ but different from the one of NbO_2. Since Nb atoms are coordinated octahedrally by O atoms in a distorted manner in both reference samples (see [67] for $LiNbO_3$ and [49] for NbO_2) these differences will be discussed later on.

Despite all the similarities between the five sample spectra at the Ta/Nb LIII edge there are differences that need to be discussed (Figure 4.4 and Figure 4.5):

(i) All Ta and Nb LIII edge whitelines are split into two peaks, approximately 4eV apart, which is a consequence of crystal field splitting of Ta 5d and Nb 4d levels. The fact that this effect is not visible for 4TiO2+KB2 at the Ta LIII edge is a consequence of a smaller splitting. The degree of crystal field and ultimately whiteline splitting depends on the coordination symmetry around absorbing atoms and increases in the following order for group V, VI and VII metal compounds of 4d/5d transition metals [69]:

tetrahedron < distorted octahedron < regular octahedron

A splitting of about 4eV indicates that Ta and Nb atoms in all five samples are coordinated octahedrally by oxygen atoms in a distorted manner. This supports the finding from the Ta LIII edge post-edge region: the spectral (and thus local structural) similarity of all five measured samples to tantalite. The same coordination symmetry can be found for Ti atoms in rutile/anatase, which is a strong indication that these were actually replaced by Ta and Nb in the TiO_6 octahedra. According to [70], the ionic radii of 6-fold coordinated Ti^{4+} (0.61Å), Ta^{5+} and Nb^{5+} (both 0.64Å) are very similar. A replacement is thus likely and it is not expected that incorporation of the dopants Ta and Nb significantly changes the degree of distortion of its surrounding octahedra. A different degree of distortion manifests itself in a different whiteline peak intensity ratio [71] or degree of whiteline splitting [69]. To examine these statements whiteline fits were performed using a sum of two Lorentzians (Ta LIII edge) or two Gaussians (Nb LIII edge) to account for transitions to the "doublet" (two energy levels created by crystal field splitting in octahedral coordination: t_{2g} and e_g) and one arctan function to account for transitions to the continuum using MATHEMATICA (version 9.0.1.0). All functions were constrained to the same width because they all originate from the same electron state being excited ($2p_{3/2}$). First the 4TiO2 spectrum was fitted. Due to the correlation between the positions and widths of the Lorentzian/Gaussian functions the former were optimized manually, then kept fixed and just the widths fitted. This fit width was then kept fixed and the positions fitted. For the sake of consistency the value for the width was used for the fits of all other spectra. Because there is a shoulder on the high-energy side of the Ta LIII edge whitelines the position of the arctan function was constrained to a higher energy than the second Lorentzian function. This wasn't necessary at the Nb LIII edge because there are no visible shoulders. Replacing the Lorentzians with Pseudo-Voigts (Ta LIII edge) and the Gaussians with Lorentzians or Pseudo-Voigt functions (Nb LIII edge) gave only minor improvements. Figure 4.7a and b show as an example the fit results of the 4TiO2 spectrum at

the (a) Ta LIII and (b) Nb LIII edge. Table 4.1 summarizes the most relevant fit results. Fits of the other eight spectra together with the complete fit results can be found in the Appendix (Figure A9a-e as well as Table A1 and Figure A10a-e as well as Table A2).

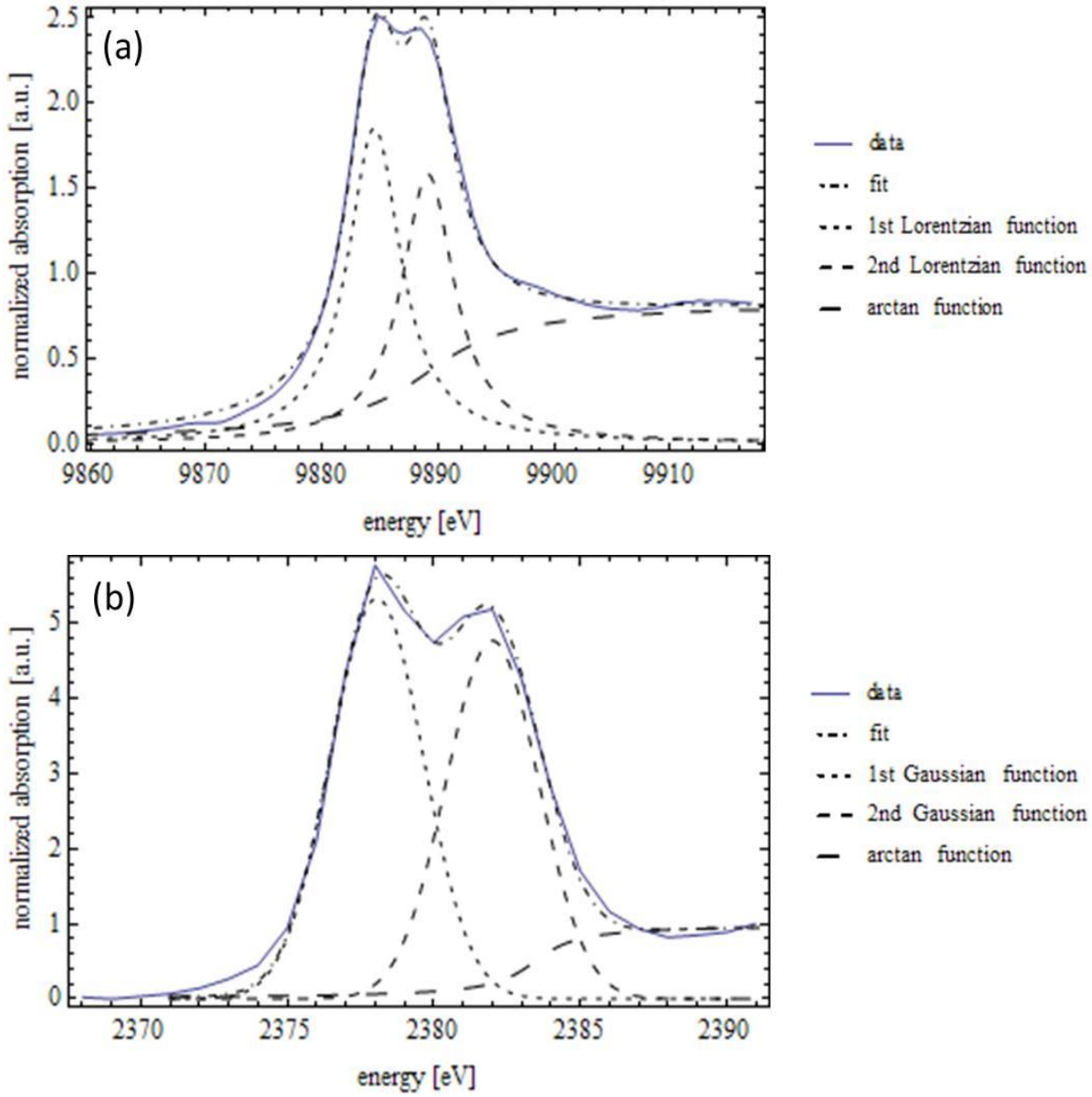

Figure 4.7: whiteline fits of the 4TiO2 spectrum at the (a) Ta LIII and (b) Nb LIII edge

Table 4.1: Ta and Nb LIII edge whiteline splittings and amplitude ratios (= amplitude of $1^{st}/2^{nd}$ Lorentzian function) of all five measured sample spectra as determined by MATHEMATICA fits (errors were calculated according to the Gaussian error propagation law using the uncertainties given by MATHEMATICA)

	4TiO2	**4TiO2+KB**	**4TiO2+KB2**	**4TiO2+Pt**	**4TiO2+TKKE**
whiteline splitting (Ta LIII edge) [eV]	4.6 ± 0.1	4.0 ± 0.1	3.8 ± 0.1	4.2 ± 0.1	4.1 ± 0.1
amplitude ratio (Ta LIII edge)	1.2 ± 0.1	1.2 ± 0.1	1.2 ± 0.1	1.2 ± 0.1	1.2 ± 0.1
whiteline splitting (Nb LIII edge) [eV]	3.9 ± 0.2	3.8 ± 0.2	3.3 ± 0.2	3.9 ± 0.1	3.8 ± 0.2
amplitude ratio (Nb LIII edge)	1.1 ± 0.1	1.1 ± 0.1	1.2 ± 0.1	1.1 ± 0.1	1.1 ± 0.1

As can be seen in Table 4.1, the whiteline splittings are identical (in the range of error) with two exceptions: (1) the 4TiO2 Ta LIII edge splitting is strongest of all five samples. Possible explanations are a lower Ta concentration in this sample or that interaction with C/Pt causes the TaO_6 octahedra to be more distorted and thus a smaller splitting in the other four sample spectra. The latter seems more likely because whiteline intensity differences indicate some kind of interaction between Ta and C/Pt atoms which is more pronounced at the Ta than the Nb LIII edge (Figure 4.4 and Figure 4.5, respectively). (2) The core-shell sample (4TiO2+KB2) shows the smallest splitting (and thus highest degree of distortion) of both TaO_6 and NbO_6 octahedra. One possible explanation is that Ta/Nb atoms are partially present in a lower than 5+ oxidation state. This would result in a larger ionic radius that distorts the TaO_6/NbO_6 octahedra to a greater extent. Yet, the highest degree of distortion can also be found at the Ti K edge for TiO_6 octahedra which strongly suggests that the whole TiO_2 structure is highly disordered in this sample.

The amplitude ratios of the two whiteline peaks (= amplitude of $1^{st}/2^{nd}$ Lorentzian function) are identical for all samples and dopants in the range of error. This means that the different compositions and degrees of distortion of the TaO_6/NbO_6 octahedra do not cause “a shift in occupation (from upper to lower state of the doublet)” as is the case in [71].

What “degree of distortion” means as well as its impact on Ti K edge pre-edge region was already discussed in chapter 4.1.2. The same aspects are now revisited and their impact on Ta/Nb LIII edge whitelines shown. In [69] DFT calculations were done to investigate the

impact of different bond lengths/angles in ReH_6 octahedra on the energy position/splitting of the Re 5d levels caused by crystal field splitting. A change in bond angles seems to have a bigger impact (effectively) on the whiteline splitting than a change in bond length. Following these results it means that maybe the dopant-O bond lengths are different between samples characterized in this work, but definitively the O-dopant-O bond angles are! Coordination is another aspect that has a tremendous impact on the shape of LIII edge whitelines. Mayanovic et al. [71] simulated Ta LIII edge XANES spectra with Ta being 5-/6- and 7-fold coordinated by oxygen. Because these spectra are quite different from each other and from the ones in Figure 4.4, it is safe to assume that only 6-fold coordination needs to be considered when talking about distortion. In [72] Nb LIII edge spectra are shown with Nb being 4- and 6-fold coordinated by oxygen. Both give split whitelines but 4-fold coordination shows a splitting of about 2eV with a more intense second peak and 6-fold coordination shows a splitting of about 4eV with a more intense first peak. From this observation one can deduce that Nb atoms in all five samples are predominantly present in 6-fold coordination as well (Figure 4.5), 4TiO2+KB2 most likely being the only exception. Its smaller whiteline splitting and equally intense whiteline peaks could be explained with Nb being partially present in 4- and/or 5-fold coordination.

The whiteline intensity increases in the order (Figure 4.4 and Figure 4.5):

4TiO2 < 4TiO2+Pt < 4TiO2+KB < 4TiO2+TKKE < 4TiO2+KB2 (Ta LIII edge)

4TiO2+KB = 4TiO2+TKKE < 4TiO2+KB2 < 4TiO2 < 4TiO2+Pt (Nb LIII edge)

For Ta this is the inverse trend as the whiteline splitting, for Nb it is not. This strongly suggests an electron transfer from the different supports and the catalyst to the Ta atoms. Nb on other hand seems to donate electrons to all carbon supports but accept electrons from the Pt catalyst. In any case there is an interaction between the dopants and the supports as well as the catalyst. One possible explanation is the formation of dopant-O-C/Pt bonds. Given the fact that the concentrations of the two dopants are rather low (Ta/Nb: 4/6at%) an electron transfer seems like an unlikely scenario, especially considering that to form dopant-O-C bonds dopant atoms would have to sit predominantly at or close to the surface. However, no better explanation is available at this point. The Ta LIII edge whitelines of all five measured samples are close to the one of Ta_2O_5, indicating that Ta atoms in these samples are present in a 5+ oxidation state. All these whitelines show a shoulder on the high energy side at about 9,900eV (Figure 4.4). According to [71] this is due to 2p → 6s transitions. No such shoulder can be seen in the Nb LIII edge spectra. As can be seen in Figure 4.6b, the whiteline of 4TiO2 closely resembles the one of LiNbO3 whereas it is completely different from the one of NbO_2

regarding whiteline splitting and peak intensity ratio. This (and the resemblance of the whitelines of all five measured samples amongst each other) strongly suggests that Nb atoms in all five samples are predominantly present in a pentavalent state as well.

It should be stressed at this point that the idea behind doping was to increase the electronic conductivity of the semiconductor TiO_2 by providing additional electrons. At the time of the measurements this effect should already took place, meaning that Ta and Nb should be present in a lower than 5+ oxidation state. Based on the results in this chapter it looks like this did not happen.

(ii) Spectra of samples with and without C(KB) have shape resonances at different positions (marked "s.r." in Figure 4.4a+b). This discrepancy is most likely caused by the different geometric structure in and beyond the first coordination shell of rutile/anatase. The shape resonance in case of the core-shell sample (4TiO2+KB2) is not very pronounced, which points towards this sample having the smallest particle size.

(iii) Spectra of samples with and without C(KB) have EXAFS features at different positions (marked "e.f." in Figure 4.4b). This suggests different Ti-O and Ti-Ti or Ta-O and Ta-Ti bond lengths, which is most likely due to the different TiO_2 structures.

(iv) The 4TiO2+KB2 signal decreases fastest with increasing energy at both the Ta and Nb LIII edge suggesting the smallest particle size which agrees with the shape resonance finding in (ii). Other differences between spectra at the Nb LIII edge (Figure 4.5) are for the most part caused by the rather poor data quality.

Figure 4.8 shows normalized Nb LII edge XANES spectra of all five measured samples. Between 3 and 6 individual scans were averaged for one spectrum. The inset shows the whiteline regions:

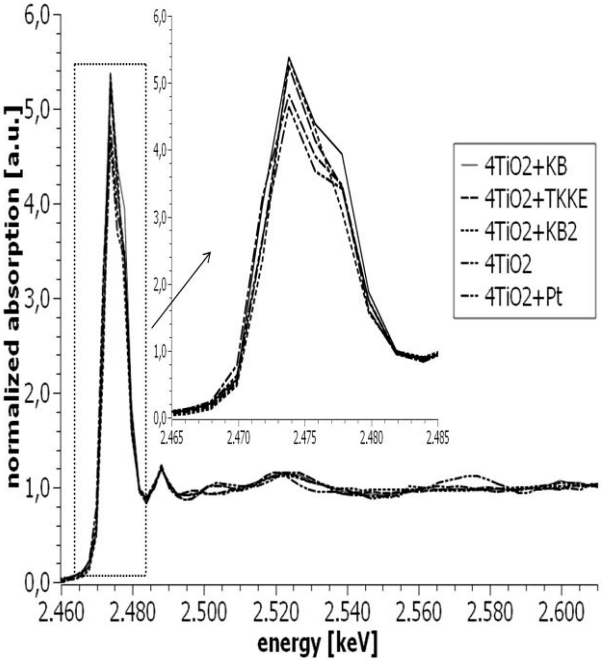

Figure 4.8: normalized Nb LII edge XANES spectra of all five measured samples. Inset: whiteline regions

The whiteline intensity roughly shows an inverse trend compared to the Nb LIII edge intensity (Figure 4.5) suggesting, compared to 4TiO2, a slight shift in occupation in all five samples between Nb $4d_{3/2}$ and $4d_{5/2}$ levels, because one probes the unoccupied density of $4d_{3/2}$ and $4d_{5/2}$ states at the Nb LIII but just the one of $4d_{3/2}$ states at the Nb LII edge. One explanation for this finding is different degrees of distortion of NbO_6 octahedra in the five samples.

Asakura et al. determined a negative linear correlation between whiteline splitting at the LIII edge and the pre-edge feature intensity at the K or LI edge [69]. It was already established in this chapter that a smaller LIII edge whiteline splitting can be explained with a higher degree of distortion of the respective dopant-O_6 octahedra. A higher degree of distortion causes the empty 6p/5d (Ta) and 5p/4d (Nb) as well as O 2p states to hybridize to a greater extent and thus a greater contribution of p-states to the pd hybrid orbitals. A more pronounced contribution leads to an increase in K and LI edge pre-edge feature intensities because these are strongly influenced by s → p transitions. To check this correlation between whiteline splitting and pre-edge feature intensities Nb K and Ta LI edge XANES spectra were evaluated.

4.1.4.XANES: Nb K & Ta LI edge

Because samples that don't contain C(KB) returned similar Nb K XANES spectra as did samples that do, both groups of samples are portrayed separately in Figure 4.9. This

discrepancy is most likely due to TiO_2 being present as anatase in the C(KB)-containing samples and as rutile in all other ones (cf. Figure 4.2). The 4TiO2 spectrum is included in both images to show similarities and differences. Between 3 and 6 individual scans were averaged for one spectrum.

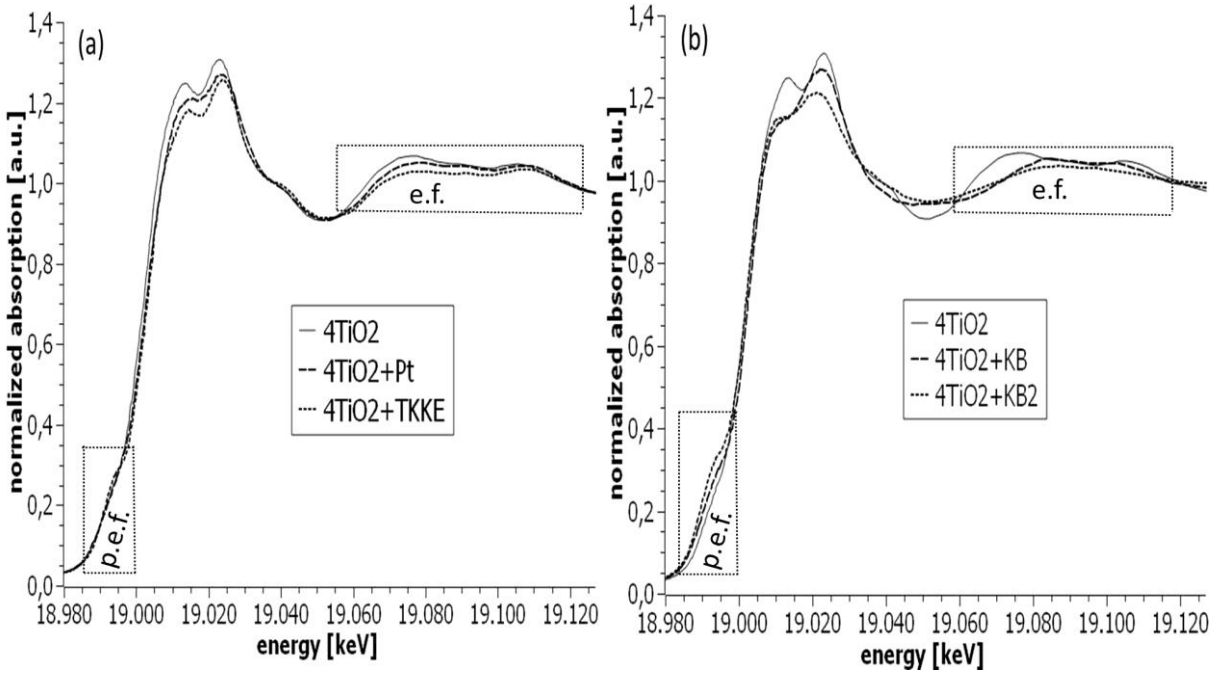

Figure 4.9: normalized Nb K edge XANES spectra of (a) 4TiO2, 4TiO2+Pt as well as 4TiO2+TKKE and (b) 4TiO2, 4TiO2+KB as well as 4TiO2+KB2. “p.e.f.” and “e.f.” mark “pre-edge features” and “EXAFS features”, respectively.

This spectral resemblance between samples without C(KB) isn’t as clear at the Ta LI edge which is most likely due to the rather poor data quality (Figure 4.10). Both spectra were measured in transmission. 23 and 13 individual scans were averaged for one spectrum.

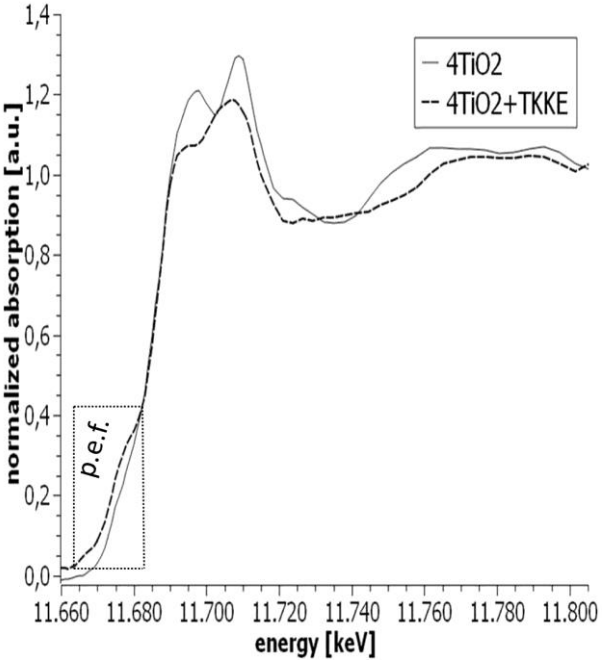

Figure 4.10: normalized Ta LI edge XANES spectra of 4TiO2 and 4TiO2+TKKE. “p.e.f.” marks “pre-edge features”

The similarity amongst the Nb K edge spectra confirms the finding from the Nb LIII edge that Nb atoms in all five measured samples have a similar local geometric environment. Differences in the post-edge region can reasonably be assumed to reflect the different host structures anatase and rutile. Differences in this region at the Ta LI edge are for the most part caused by the rather poor data quality.

Despite all the similarities between sample spectra at the Nb K and Ta LIII edge there are differences that need to be discussed (Figure 4.9 and Figure 4.10):

(i) The pre-edge feature intensities (marked “p.e.f.”) increase in the order:

4TiO2 < 4TiO2+Pt < 4TiO2+TKKE < 4TiO2+KB < 4TiO2+KB2 (Nb K edge)

4TiO2 < 4TiO2+TKKE (Ta LI edge)

As explained at the end of chapter 4.1.3, this means that distortion of NbO_6 and TaO_6 octahedra increases in the same order. One important aspect to consider here is the number of atoms adjacent octahedra share. In [73] mineral samples are compared that contain NbO_6 octahedra that are either isolated, corner- or edge-sharing. The first two give similar pre-edge features intensities whereas the latter gives a higher one. The reason for this is cation-cation repulsion, which gets more pronounced the more atoms adjacent octahedra share. The pre-edge intensities of samples characterized in this work resemble that of isolated and corner-shared octahedra. Because octahedra share 2 edges in rutile and 4 in anatase [74] this strongly suggests that Nb and Ta atoms are statistically distributed in the respective TiO_2 host structure of all five characterized samples! According to Antonio et al. ([75]) there is a correlation

between the pre-edge feature and the oxidation state of Nb ions: the pre-edge feature shifts to lower energies and loses intensity with increasing Nb^{4+} concentration and is absent for $Nb(IV)O_2$. There doesn't seem to be a significant shift of this feature in the spectra presented here, pointing towards a very similar ratio of Nb^{5+}/Nb^{4+} in all five samples (Figure 4.9). The fact that there is a pre-edge feature means that a significant portion of Nb atoms are present in a pentavalent state in all five measured samples. It is reasonable to assume that this is also the case for Ta, given the similar electronic structures of Nb and Ta. This assumption is supported by the work of Yamamoto [60], who found a negative linear dependence of K pre-edge feature intensities from the number of d-electrons for 3d transition metal compounds. There is some evidence in this paper that the same dependence is true for 4d and 5d transition metal compounds. This finding agrees with Ta/Nb LIII edge results which suggest that Ta/Nb atoms are predominantly present in a pentavalent state.

For a quantitative evaluation of Nb K edge pre-edge features of all five measured samples fits were performed using MATHEMATICA and the approach based on [69]. One Lorentzian function was used for the fit of the pre-edge feature to account for transitions from 1s to pd states with p-character. Another Lorentzian and one arctan function were chosen to fit the pre-edge region only and do not correspond to actual electron transitions. The 4TiO2 spectrum was fitted first and the arctan amplitude as well as the width of all functions held constant for all subsequent fits. The same parameter was used to fit the widths of the two Lorentzian functions. Since the sole purpose of this fit process was a quantitative evaluation of Nb K edge pre-edge feature intensities (= intensities of the first Lorentzian function), no attention was given to the feasibility of all other parameters. The 4TiO2 fit is shown as an example in Figure 4.11. Table 4.2 summarizes the peak areas of the first Lorentzian function of all five samples. Fits of the other four spectra together with complete fit results can be found in the Appendix (Figure A11a-e and Table A3).

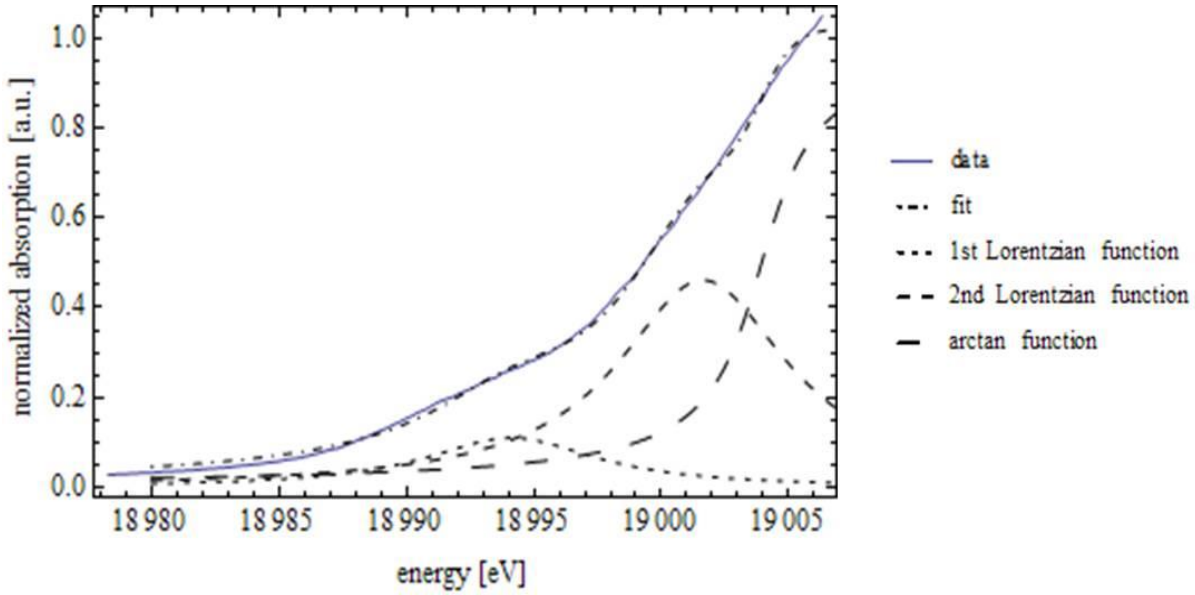

Figure 4.11: MATHEMATICA fit of the 4TiO2 Nb K edge pre-edge feature

Table 4.2: Nb K edge pre-edge feature areas (the area under the first Lorentzian function) of all five measured samples as determined by MATHEMATICA fits. Uncertainties are given by MATHEMATICA.

sample	**pre-edge feature area**
4TiO2	1.42 ± 0.05
4TiO2+Pt	1.74 ± 0.05
4TiO2+TKKE	1.91 ± 0.05
4TiO2+KB	2.11 ± 0.05
4TiO2+KB2	2.52 ± 0.05

The values of the pre-edge feature areas indicate that Nb is coordinated octahedrally by oxygen atoms in a distorted manner in all five samples (see [69]). This conclusion is supported by Piilonen et al. [73], who calculated Nb K edge XANES spectra with Nb being 5-fold coordinated by O atoms, resulting in a pre-edge feature much more intense than the ones observed in this work (Figure 4.9).

An analogous situation was found by Tanaka et al. [76], who showed a Ta LI edge spectrum in which Ta atoms are “coordinatively unsaturated” (partially having a lower than 6-fold coordination); a conclusion they based on the increased pre-edge feature intensity. Because the intensity increase one gets from Ta atoms having less than 6 neighbours is very pronounced one can exclude this scenario when looking at the pre-edge feature intensities in Figure 4.10.

Because differences between the five samples regarding their LIII edge whiteline splitting are less pronounced compared to differences regarding their K/LI edge pre-edge feature

intensities I hypothesize that the latter are more sensitive to distortion of coordination symmetry than the former.

(ii) The whiteline intensity increases in the order:

4TiO2+TKKE < 4TiO2+Pt < 4TiO2 and 4TiO2+KB2 < 4TiO2+KB < 4TiO2 (Nb K edge)

4TiO2+TKKE < 4TiO2 (Ta LI edge)

As pointed out in chapter 4.1.1, whitelines at the Nb K and Ta LI edge consist of two peaks. Intensity differences indicate an electron transfer from Nb/Ta to the different supports and catalyst whose trend is different than that of the LIII edge (Figure 4.5). Because at the LIII edge the unoccupied Nb 4d/Ta 5d DOS is probed whereas the Nb 5p/Ta 6p DOS is probed at the K/LI edge, this speaks for a complex interaction of both dopants with the different supports and catalyst. The intensity decrease of the two whiteline peaks compared to the 4TiO2 spectrum is not uniform. For all samples the intensity decrease of the first peak is more pronounced than the second one. The latter is also severely broadened in case of the C(KB)-containing samples. Because whiteline peaks at the Nb K/Ta LI edge are believed to be caused by transitions to split p-levels, a non-uniform intensity decrease means that these levels contribute to different degrees to an electron transfer.

(iii) The intensities of the EXAFS features (marked “e.f.” in Figure 4.9a+b) and the whitelines show the same trend for samples with and without C(KB). In general, EXAFS feature intensities are proportional to the number of bonds. Both the whiteline and EXAFS feature intensities could therefore be explained with a lower Nb concentration and thus number of Nb-O bonds.

(iv) Similarities and differences in the post-edge region can reasonably be assumed to reflect the different host structures anatase and rutile meaning a similar local geometric environment of Ta/Nb atoms in the samples with and without C(KB). The XANES signal of the 4TiO2+KB2 spectrum decreases fastest with increasing energy compared to every other spectrum, which agrees well with the results from the Ti K and Ta/Nb LIII edge. This means that TiO_2 particles in this sample show the smallest particle size from the Ti, Ta, and Nb point of view.

Figure 4.12 compares Nb K, Ta LI and Ti K edge spectra of (a) 4TiO2 and (b) 4TiO2+TKKE. The last two were shifted in energy until edge and post-edge features were aligned. Spectra are vertically offset for clarity:

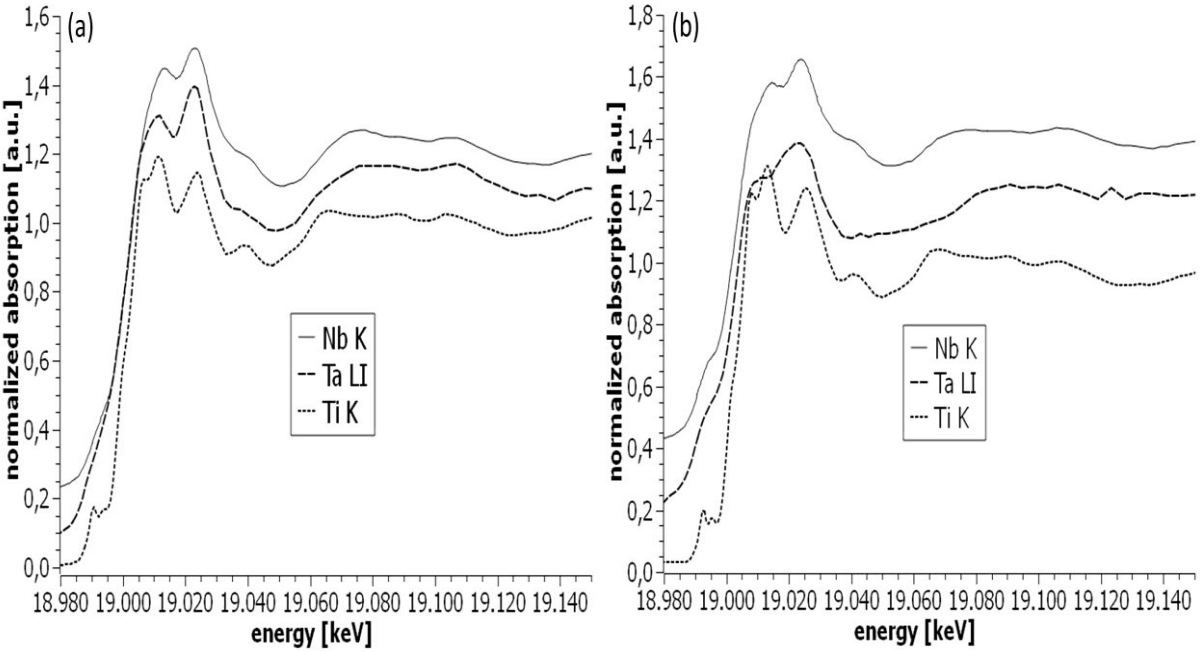

Figure 4.12: normalized Nb K, Ta LI and Ti K edge XANES spectra of (a) 4TiO2 and (b) 4TiO2+TKKE, vertically offset

All spectra show a close spectral resemblance strongly suggesting a similar local geometric environment of Nb, Ta and Ti atoms in but also beyond the first coordination shell. This finding supports the conclusions drawn from the Ta/Nb LIII edge whiteline splittings and Ta LI/Nb K edge pre-edge feature intensities that Ta/Nb atoms did substitute Ti atoms in both samples and are statistically distributed in their respective TiO_2 host structure. Differences in the post edge region at the Ta LI edge are due the rather poor data quality and a different energy resolution.

Based on the results presented so far I came up with a hypothesis I didn't find in literature in this form. As is already known, whiteline intensity differences at the Ta/Nb LIII edge between the five measured samples are caused by different densities of Ta 5d/Nb 4d states. My hypothesis now is these have an, what I call, "external" and an "internal" contribution. "External" in this scenario means that electrons are transferred between dopant (Ta/Nb) and non-dopant atoms (O/C/Pt) forming bonds between them. The "internal" contribution on the other hand implies a change of the crystal field in dopant-O_6 octahedra caused by a change in symmetry (distortion of said octahedra). Accordingly, these changes get more pronounced for higher degrees of distortion. This geometrical change is accompanied by changes of the character of Ta 5d (Nb 4d) and Ta 6p (Nb 5p) wave functions ultimately determining transition probabilities and thus intensities of pre-edge and whiteline peaks. Because the degree of distortion of dopant-O_6 octahedra is slightly different between samples and dopants

it means that there has to be some kind of interaction between dopant and C/Pt atoms. The external effect thus causes the internal effect.

For Ta this hypothesis is supported by XANES data. Based on the LIII edge whiteline splittings, the degree of distortion of TaO_6 octahedra increases in the following order:

4TiO2 < 4TiO2+Pt = 4TiO2+KB = 4TiO2+TKKE < 4TiO2+KB2

Based on my hypothesis of the internal effect, this means that the sample 4TiO2 has the highest number of 5d and lowest number of 6p electrons (the opposite is true for the sample 4TiO2+KB2). Consequently, whiteline intensities should follow the same trend at the Ta LIII edge and the inverse trend at the Ta LI edge as the degree of distortion of TaO_6 octahedra. This can indeed be observed (Figure 4.4 and Figure 4.10). Additionally, pre-edge feature intensities at the Ta LI edge should follow the same trend as the respective whiteline intensities since both are caused by transitions to states with p-character. This is also the case.

Nb K edge pre-edge feature intensities suggest that the degree of distortion of NbO_6 octahedra increases in the following order:

4TiO2 < 4TiO2+Pt < 4TiO2+TKKE < 4TiO2+KB < 4TiO2+KB2

(I use K edge pre-edge features instead of LIII edge whiteline splittings at this point because differences regarding the latter are more pronounced) Applying the internal effect part of my hypothesis again, this means that the whiteline intensities at the Nb LIII edge should follow the same trend as the degree of distortion of NbO_6 octahedra which is in fact not the case (Figure 4.5). Yet, Nb K edge pre-edge feature as well as whiteline intensities indeed do follow the inverse trend as the degree of distortion of NbO_6 octahedra (Figure 4.9) thus confirming my hypothesis. In Figure 2.1 it can be seen that x-rays are attenuated more strongly by a material the lower their energy is which makes samples more prone to self-absorption. Due to the fact that the Nb LIII edge is at the lowest energy of all edges under investigation here, self-absorption is most likely the reason why Nb LIII edge whiteline intensities don't follow the predicted trend. Because this aspect is the only one not confirming my hypothesis, taking into account all other aspects I still believe it to be reasonable.

This hypothesis now raises the following question: does distortion of dopant-O_6 octahedra indeed change the densities of Ta 5d (Nb 4d) and Ta 6p (Nb 5p) states? In [7] it is argued that upon formation of Pt nanoparticles from Pt atoms hybridization of 5d/6s/6p orbitals occurs leading to a charge redistribution of electrons from states with d- to ones with s- and p-character. Therefore, charge redistribution upon hybridization is something that does indeed occur in case of transition metals. Taking into account that the degree of distortion of dopant-O_6 octahedra does in fact impact said hybridization it is, in my opinion, reasonable to assume

that a higher degree of distortion changes the densities of Ta 5d (Nb 4d) and Ta 6p (Nb 5p) states and thus the intensities of Ta LI (Nb K) pre-edge features and Ta (Nb) LIII whitelines. Another argument that speaks for the feasibility of my hypothesis is that the two aspects degree of distortion and number of d-electrons influence the pre-edge feature intensities in opposite ways. A lower degree of distortion as well as a higher number of d-electrons leads to less intense pre-edge features. Yet, the latter also results in larger ionic radii, thus a higher degree of distortion and eventually more intense pre-edge features. The fact that Nb K edge pre-edge feature intensities actually decrease with a higher number of d-electrons ([75], [77]) means that this aspect has a stronger influence on pre-edge feature intensities than the degree of distortion or that there is an internal effect causing a change of the character of Ta 5d (Nb 4d) and Ta 6p (Nb 5p) wave functions.

Results from the last two sections showed that both dopants Ta and Nb substituted Ti atoms in TiO_6 octahedra, which was the goal of the synthesis. The core-shell sample (4TiO2+KB2) displays the highest degree of disorder and smallest particle size, which is most likely correlated. Whiteline intensity differences indicate an interaction of both dopants with the carbon supports as well as the Pt catalyst, most likely via dopant-O-C/Pt bonds. The results strongly suggest that both dopants are statistically distributed in their respective samples. This finding and the distortion of dopant-O_6 octahedra were checked by means of EXAFS.

4.1.5.EXAFS: Ta LIII & Nb K edge

As is explained in greater detail in chapter A 1.2, for the calculation of EXAFS data one first has to pick one or more structural models, which should resemble the sample whose data are fitted as closely as possible. For fitting Ta LIII and Nb K edge EXAFS data two structural models are now introduced. Both are derived from the rutile structure ([48], COD ID: 9015662) and in both cases the respective dopant replaces Ti atoms in the TiO_6 octahedra thus creating TaO_6 and NbO_6 octahedra, as was already concluded from the respective XANES results. If the dopants were statistically distributed these dopant-O_6 octahedra would be sharing O atoms with TiO_6 octahedra whereas those would be dopant-O_6 octahedra if dopants formed cluster. Because EXAFS measures the radial distribution of atoms around absorber atoms, from the dopants point of view two possible scenarios emerge: in case of a statistical distribution, Ta/Nb atoms “see” Ti atoms in the second and third shell whereas those are Ta/Nb atoms if clustering occurred. These scenarios were named “scattering model” and “cluster model”. They are depicted in Figure 4.13:

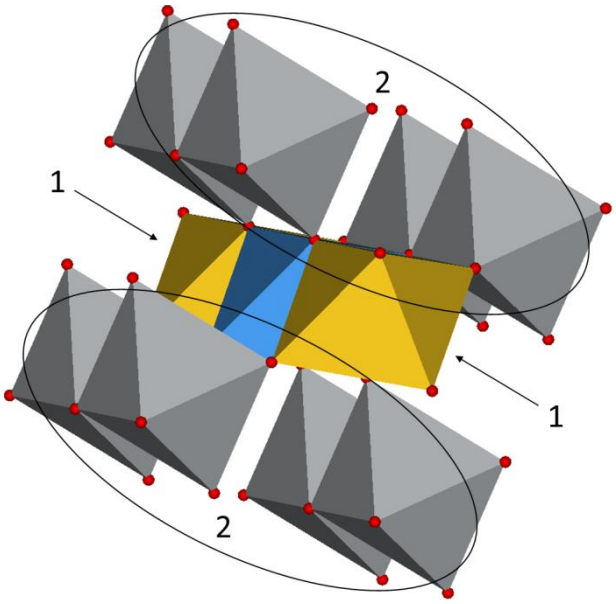

Figure 4.13: illustration of the scattering and cluster model. Central: dopant-O_6 octahedron, "1" mark the two dopant-O_6 (cluster model) or TiO_6 octahedra (scattering model), "2" mark the eight TiO_6 octahedra. Small circles represent O atoms. Both models are derived from the rutile structure.

Both models were then used to calculate theoretical EXAFS spectra using the EXAFS equation (cf. chapter 2). Their parameters were fitted until an optimal agreement between theoretical model and experimental data was reached. Fits were done in R-space up to the 3rd shell. Every shell had two fit parameters (R = distance from the absorber atom to the respective shell and σ^2 = mean-square displacement between the absorber atom and the atoms in a respective shell). Numbers of next neighbours N were first fixed to the respective crystallographic values of rutile due to their strong correlation to the σ^2 parameter. After reasonable σ^2 values were obtained N was fitted as well for the 1st Ta shell. As was established in the last three chapters, Ta and Nb replace Ti in the TiO_6 octahedra that are already distorted. Any distortion will lead to different dopant-O bond lengths in different directions and thus a splitting of the oxygen shell around the dopant atoms. To account for this splitting in case of Nb data four models were proposed:

i. 6 O atoms at the same distance
ii. 2 O atoms at one and 4 at a shorter distance
iii. 3 O atoms at one and 3 at a shorter distance
iv. 4 O atoms at one and 2 at a shorter distance

Taking into account the scattering and cluster model this resulted in a total of 8 models. In the structural model used to fit Ta data no splitting was implemented because the respective peak in the Fourier transform magnitude is a lot narrower compared to Nb data (not shown). A splitting thus seemed unlikely. One ΔE parameter was fitted for all paths of the respective data set.

At the Ta LIII edge, data was collected for an EXAFS analysis beyond the first shell only of the 4TiO2 sample. The scattering model turned out to give better results than the cluster model, as is demonstrated in the following. Figure 4.14a and b compare the fit results of both, magnitude and imaginary part of the Fourier transform:

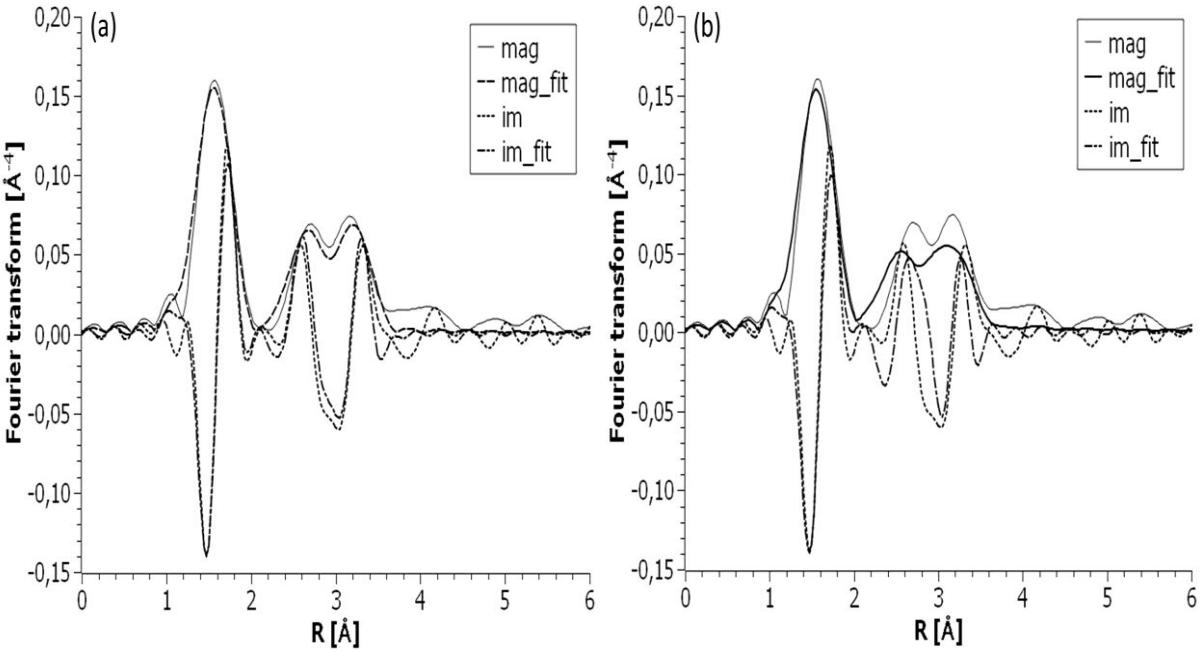

Figure 4.14: EXAFS fit results of 4TiO2 Ta LIII edge data in R-space using the (a) scattering and (b) cluster model. The Fourier transform magnitude is denoted by “mag” and its imaginary part by “im”.

Comparing results in Figure 4.14 one can clearly see that both models fit the first shell equally well (because the parameters were the same). Yet, the scattering model fits the 2nd and 3rd shell better as can be seen from both the magnitude and imaginary part of the Fourier transform.

Another way to look at EXAFS data is in k-space. To do that, contributions from the three scattering paths were back Fourier transformed for both models and compared to the experimental data as can be seen in Figure 4.15:

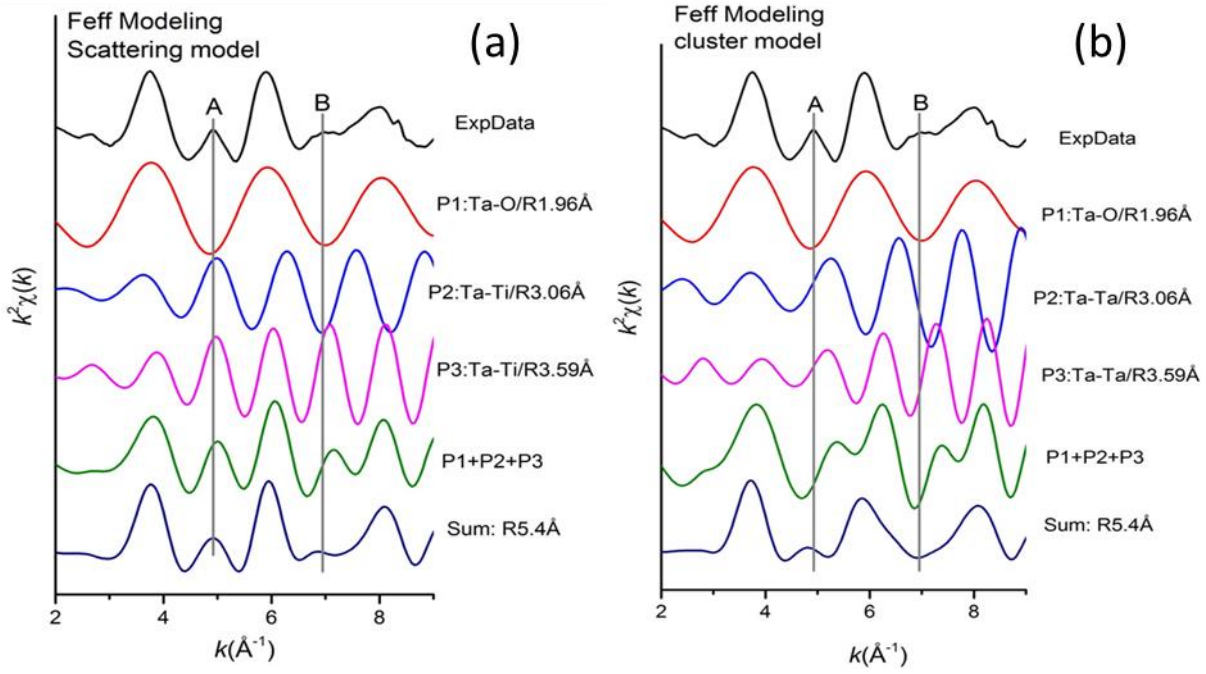

Figure 4.15: k^2-weighted Ta LIII edge EXAFS data of 4TiO2 in k-space ("ExpData"). Contributions of the three scattering paths and their respective distance from the absorber atom are added ("P1/P2/P3") as well as their sum for a cluster of 5.4Å in size for the (a) scattering and (b) cluster model. All data are vertically offset for clarity. "A" and "B" mark features that are reproduced by the scattering but not the cluster model.

What can be learned from looking at the data in k-space is that only the scattering model reproduces the features at 5 and 7$Å^{-1}$.Values of the fit parameters are now summarized in Table 4.3:

Table 4.3: EXAFS fit results of 4TiO2 Ta LIII edge data ("f" refers to a parameter kept fixed during a fit to its respective crystallographic value, N = number of next neighbours, R = distance from absorber atom to the respective shell, σ^2 = mean-square displacement of the bond length between the absorber atom and the atoms in a shell.)

model	**path 1**			**path 2**			**path 3**			**residual**
	N	**R [Å]**	**σ^2 [Å²]**	**N**	**R [Å]**	**σ^2 [Å²]**	**N**	**R [Å]**	**σ^2 [Å²]**	
scattering	5.8	1.96	0.0028	2^f	3.06	0.0036	8^f	3.59	0.0074	13.3
cluster	5.9	1.96	0.0039	2^f	2.74	0.0076	8^f	3.25	0.0075	27.6
rutile	6.0	1.96	/	2	2.96	/	8	3.57	/	/
path 1: Ta-O for scattering/cluster model paths 2/3: Ta-Ti, Ta-Ta, Ti-Ti for scattering model, cluster model and rutile, respectively										

The fit results support the visual impression that the scattering model describes the local geometric structure of Ta atoms in the 4TiO2 sample better than the cluster model. The XANES finding that Ta atoms replaced Ti atoms in the TiO_6 octahedra and are statistically distributed in the TiO_2 host structure are thereby confirmed. Arguments for this conclusion are the smaller σ^2 values, R-values closer to the rutile ones and a smaller residual (cf. Table

4.3). As was assumed based on the similar ionic radii, replacing Ti by Ta does not add a significant distortion to the rutile structure, because the fitted distances agree with the bond lengths found in rutile. Differences lie within the margin of error.

The same two models were then used to fit Nb K edge EXAFS data of the samples 4TiO2, 4TiO2+Pt and 4TiO2+TKKE. In contrast to the Ta data, splitting of the O shell was included with 4 different combinations as described above (models i, ii, iii and iv). For all samples values of different models agree within error limits, meaning that all these models describe the local geometric structure of Nb atoms in the respective sample equally well (Table 4.4). Complete fit results can be found in the Appendix (Figures A12-16 and Tables A4-8).

Table 4.4: EXAFS fit results of Nb K edge data of samples 4TiO2, 4TiO2+Pt and 4TiO2+TKKE ("f" refers to a parameter kept fixed during a fit to its respective crystallographic value, "scattering" stands for the scattering as opposed to the cluster model, "ii/iii/iv" represent the models used to resolve the O shell splitting as described in greater detail in the text. Explanations of the fit parameters can be found in the caption of Table 4.3.)

sample	**model**	**path 1**			**path 2**			**path 3**			**residual**
		N	R [Å]	σ^2 [Å²]	N	R [Å]	σ^2 [Å²]	N	R [Å]	σ^2 [Å²]	
4TiO2	scattering ii / iv	2^f 4^f	2.10 1.97	0.0037 0.0037	2^f	3.02	0.0109	8^f	3.64	0.0103	6.9
	scattering iii	3^f 3^f	2.08 1.94	0.0016 0.0016	2^f	3.02	0.0109	8^f	3.63	0.0103	6.6
4TiO2+Pt	scattering ii / iv	2^f/4^f	2.09 1.96	0.0047 0.0047	2^f	3.05	0.0068	8^f	3.64	0.0090	9.8
4TiO2+TKKE	scattering ii	2^f 4^f	2.12 1.95	0.0022 0.0049	2^f	3.05	0.0096	8^f	3.65	0.0122	8.9
	scattering iii	3^f 3^f	2.09 1.93	0.0043 0.0030	2^f	3.05	0.0096	8^f	3.65	0.0122	8.7
	scattering iv	4^f 2^f	2.07 1.91	0.0065 0.0015	2^f	3.05	0.0098	8^f	3.65	0.0122	8.6
rutile	/	2 4	1.98 1.95	/	2	2.96	/	8	3.57	/	/

path 1: Nb-O for scattering/cluster model

paths 2/3: Nb-Ti, Nb-Nb, Ti-Ti for scattering model, cluster model and rutile, respectively

Results in Table 4.4 confirm the XANES finding that Nb atoms replaced Ti atoms in the TiO_6 octahedra and are statistically distributed, for the same reasons as put forward for Ta data. However, compared to Ta, there are several differences. Incorporation of Nb leads to two O subshells that can be resolved by EXAFS analysis, and Nb-O bond lengths are slightly elongated compared to rutile. One possible explanation is that Nb atoms are present in a lower than pentavalent state. Atomic distances in all three samples are identical in the range of error. Table 4.5 compares the fit results of the 4TiO2 sample from Ta LIII (scattering models ii/iv) with Nb K edge data:

Table 4.5: EXAFS fit results of 4TiO2 Ta LIII and Nb K edge data ("f" refers to a parameter kept fixed during a fit to its respective crystallographic value. Explanations of the fit parameters can be found in Table 4.3.)

	N	**R [Å]**	**σ^2 [Å^2]**
Ta-O shell	5.8	1.96	0.0028
Nb-O shell	2^f 4^f	2.10 1.97	0.0037 0.0037
1st Ta-Ti shell	2^f	3.06	0.0036
1st Nb-Ti shell	2^f	3.02	0.0109
2nd Ta-Ti shell	8^f	3.59	0.0074
2nd Nb-Ti shell	8^f	3.64	0.0103

Table 4.5 shows that bond lengths are, for the most part, slightly elongated for Nb and the respective mean-square displacement parameters are higher for each Nb path. This indicates that, at least for the sample 4TiO2, Nb incorporation does indeed cause a higher degree of distortion of the rutile host structure than Ta incorporation. One possible explanation is that the Nb^{4+}/Nb^{5+} ratio is higher than the Ta^{4+}/Ta^{5+} ratio which would also explain the smallest Ta LIII edge whiteline splitting of this sample compared to the other four (cf. Table 4.1). A lower oxidation state results in a larger ionic radius which distorts the respective dopant-O_6 octahedra to a greater extent.

Ti K edge spectra show that TiO_2 is predominantly present as anatase in the two samples containing C(KB) and as rutile in the three that don't. Ta LIII and Nb K edge post-edge regions confirm that. All five Ta LIII edge spectra also closely resemble the one of the mineral tantalite strongly indicating a very similar local geometric structure despite differing chemical compositions. A comparison of Nb K, Ta LI and Ti K edge post-edge regions of the samples 4TiO2 and 4TiO2+TKKE shows a striking resemblance meaning a very similar local

geometric environment of Nb, Ta and Ti atoms in and beyond the 1st coordination shell (at least in these two samples).

The decreased Ti K edge pre-edge feature intensities strongly indicate that both dopants Ta and Nb are incorporated into the respective TiO_2 host structure of all five samples. Ta LI and Nb K edge pre-edge feature intensities show that both dopants were incorporated in isolated dopant-O_6 octahedra meaning that both replaced Ti atoms in the TiO_6 octahedra and are statistically distributed in the respective TiO_2 host structure, which was the goal of the synthesis.

From the splitting of Ta/Nb LIII whitelines, caused by crystal field effects, it can be derived that Ta/Nb atoms are coordinated octahedrally by oxygen atoms in a distorted manner. This finding agrees with Ta LI and Nb K edge pre-edge feature results. Whiteline intensity differences between the five samples at the Ta LIII/LI and Nb LIII/K edge strongly indicate an interaction of both dopants with the carbon supports as well as the Pt catalyst, most likely via dopant-O-C/Pt bonds. No information about the average oxidation states of the dopants could be derived from Ta/Nb LIII edge positions. Yet, comparison to literature indicates that (at least a significant portion of) Ta/Nb atoms in all five samples are present in a +5 oxidation state. This is supported by the existence of pre-edge features at the Ta LI and Nb K edge which would be less intense if Ta/Nb atoms were present exclusively in a +4 oxidation state.

EXAFS analysis shows differences between Ta LIII and Nb K edge data. For one, the splitting of the O shell cannot be resolved for Ta but for Nb data. Moreover, compared to rutile, bond lengths are identical within the margin of error for Ta but slightly elongated for Nb. The respective mean-square displacement parameters of each Ta path are also smaller compared to the ones of the Nb paths. This is strong evidence that Nb incorporation did indeed distort the TiO_2 host structure of all five samples to a greater extent compared to Ta incorporation (at least for the sample 4TiO2).

The core-shell sample (4TiO2+KB2) displays the highest degree of disorder (Ti K edge: most intense A2 pre-edge feature, widest C1 whiteline peak; Ta/Nb LIII edge: smallest whiteline splitting; Nb K edge: most intense pre-edge feature) and smallest particle size (signal decreases fastest at every edge), which is most likely correlated. The fact that the highest degree of disorder can also be seen at the Ti K edge suggests that this is a consequence of the manufacturing and not the doping process.

EXAFS fits in this chapter were performed by Ning Chen, beamline scientist at the HXMA beamline at the CLS.

4.2. Reduction / oxidation behaviour of PEM fuel cell catalysts

Two nano-catalyst samples supported on two hybrid nano-supports were chosen to test their reduction/oxidation behaviour. Due to their high relative surface area nanoparticles have high affinity for oxidation, which blocks catalytically active sites and thus decreases a catalysts' activity. To what extent this is the case for this group of PEM fuel cell catalysts is addressed in this chapter. Compositions of both samples and abbreviations used for them are given in Table 3.1. Samples were stored in a refrigerator for several months before the measurements and were exposed to air during that time as well as during preparation. Pt LIII edge XANES spectra were only recorded for the first sample and both Ta LIII and Ti K edge XANES spectra were recorded for the second. A 3.7% H_2 (carrier gas: He) gas mixture was used for reduction and atmospheric air for oxidation. Bare and supported Pt NPs were reduced in [42] and [43] and values for the gas flow from these references were used as a guideline in this work, because no information was found in literature about the reduction behaviour of the samples summarized in Table 3.1. Three different approaches for sample-gas exposure were tested. The sample chamber was pumped down first to a pressure in the 10^{0} – 10^{-2}mbar range every time:

i. The sample chamber was flooded with the reduction gas to ambient pressure. Then the gas was turned off
ii. There was light gas flow without flowmeter
iii. There was a stronger gas flow with a flowmeter set to up to 45.5ml/min

Spectra were taken at different temperatures. Details can be found in the respective section.

4.2.1. PtPd_1TiO2+TKKE: Pt LIII edge XANES

First, the sample chamber was flooded with the reduction gas to ambient pressure at room temperature. The first spectrum after gas exposure was taken about 1h after the sample chamber was filled. These conditions caused the whiteline intensity to drop to the intensity of the metal foil. To test if the whiteline intensity can be recovered the sample was exposed to air at room temperature overnight. Figure 4.16 compares spectra taken before gas exposure ("before"), 1h after ("after") and having had the sample sit out overnight ("re-oxidized"):

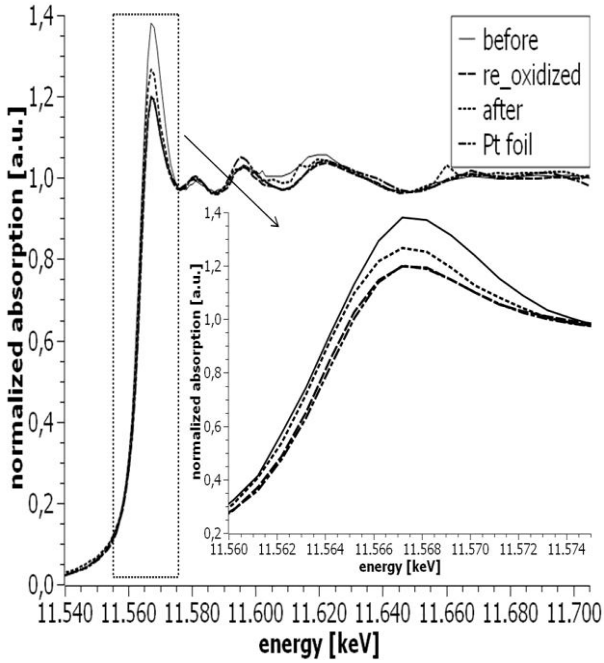

Figure 4.16: normalized Pt LIII edge XANES spectra of PtPd_1TiO2+TKKE before gas exposure ("before"), 1h after ("after") and having had the sample sit out overnight ("re-oxidized")

Based on these spectra I drew the following conclusions: (i) the sample was (partially?) oxidized before gas exposure because its whiteline intensity was well above the one of the metal foil. This conclusion is supported by comparing PtPd_1TiO2+TKKE spectra recorded on IDEAS and HXMA (Figure 4.17). Results are clearly reproducible:

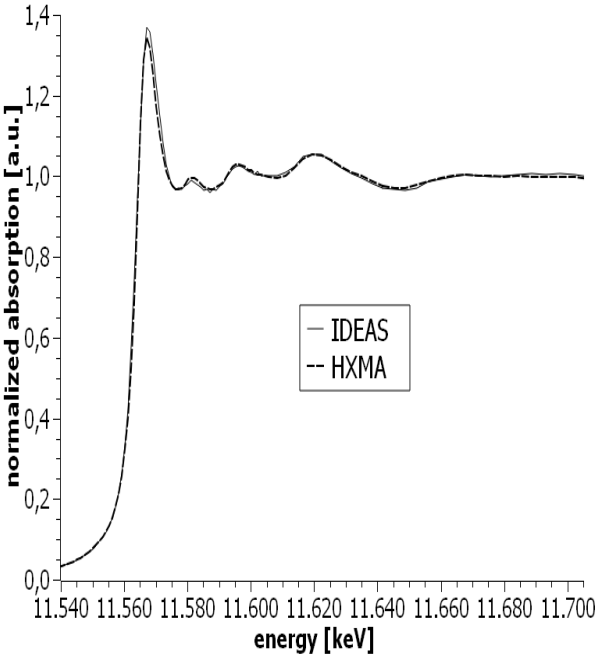

Figure 4.17: normalized Pt LIII edge XANES spectra of PtPd_1TiO2+TKKE recorded on the IDEAS and HXMA beamline, respectively

(ii) The sheer presence of the reducing gas was sufficient to reduce the sample completely, because there were no more changes in the spectra even after applying a light gas flow. A fact

supporting this conclusion is that the whiteline decreased to the level of the Pt foil. (iii) Exposing the sample to air at room temperature overnight caused the whiteline intensity to partially recover, which I interpret as a partial re-oxidation. To test if the whiteline intensity can be fully recovered the sample was exposed to air for another 5 days and subsequently heated up to almost 120°C to speed up the re-oxidation process. After about 3h the sample was exposed to the gas mixture at a flowrate of 30.0ml/min for 2h at room temperature. However, there were no more changes in the spectra despite reducing/oxidizing conditions harsher than before! Differences in the dip at about 11,610eV I attribute to experimental reasons and thus not to changes caused by the gas atmosphere.

Given these results and the fact that both samples were stored for months in air before the measurements leads me to believe that Pt atoms in this kind of sample show low affinity for oxidation. This assumption is confirmed when comparing spectra of both samples recorded at IDEAS and HXMA (Figure 4.18a+b):

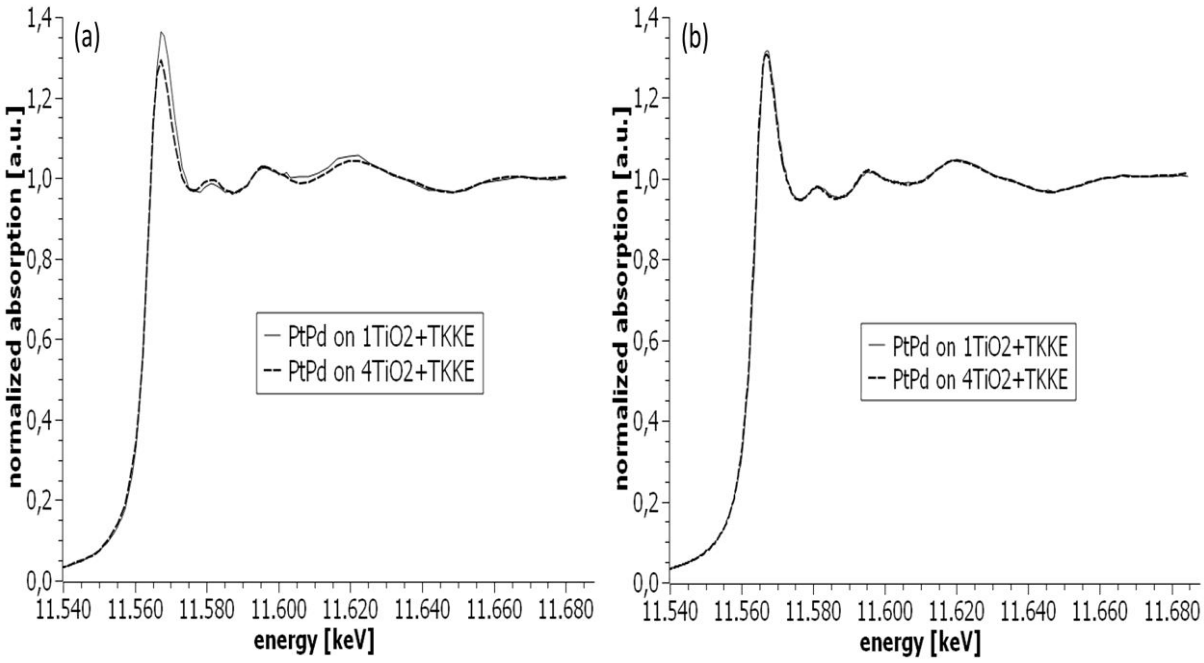

Figure 4.18: normalized Pt LIII edge XANES spectra of PtPd_1TiO2+TKKE and PtPd_4TiO2+TKKE recorded on the (a) IDEAS and (b) HXMA beamline

Above figures show that the whiteline intensity of the sample PtPd_1TiO2+TKKE is higher than the one of the PtPd_4TiO2+TKKE measured at IDEAS but identical to the one measured at HXMA. Because PtPd_4TiO2+TKKE was taken from two different batches I interpret this result in such a way that Pt atoms in the batch measured at IDEAS were oxidized to a lesser extent than the one measured at HXMA. The fact that both batches were stored in a refrigerator in air for several months before the measurements is a strong indication that Pt atoms in the group of samples studied here show indeed low affinity for oxidation.

After this first catalyst sample's reduction/oxidation behaviour was tested from the Pt point of view the behaviour of the second catalyst sample from the Ta/Ti point of view was tested as well.

4.2.2.PtPd_4TiO2+TKKE: Ta LIII / Ti K edge XANES

At the Ta LIII edge the sample PtPd_4TiO2+TKKE was exposed to the gas mixture at a flowrate of 45.5ml/min at room temperature. Figure 4.19 shows selected XANES spectra. Numbers correspond to scan numbers (insets show the whiteline region of the same spectra):

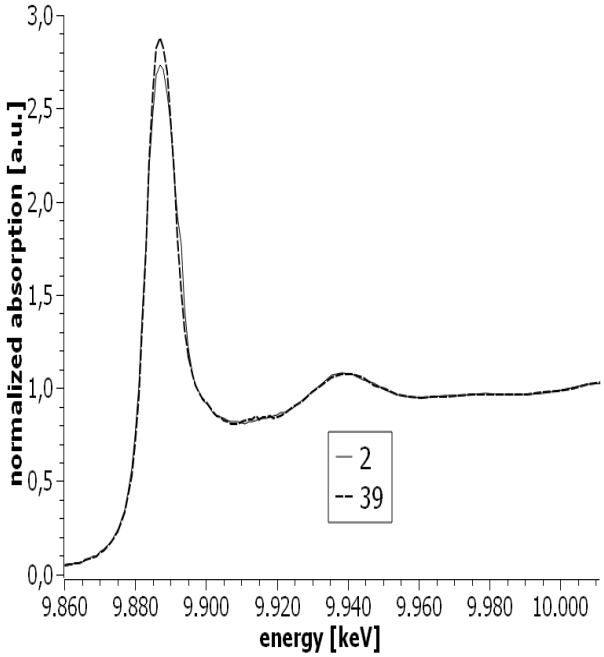

Figure 4.19: normalized Ta LIII edge XANES spectra of PtPd_4TiO2+TKKE. Numbers correspond to scan numbers ("2": before gas exposure", "39": > 6h after)

For Ti K edge data collection of the sample PtPd_4TiO2+TKKE the sample chamber was flooded with the reduction gas to ambient pressure at room temperature. Figure 4.20 compares the spectra taken before gas exposure to one done 4.5h after:

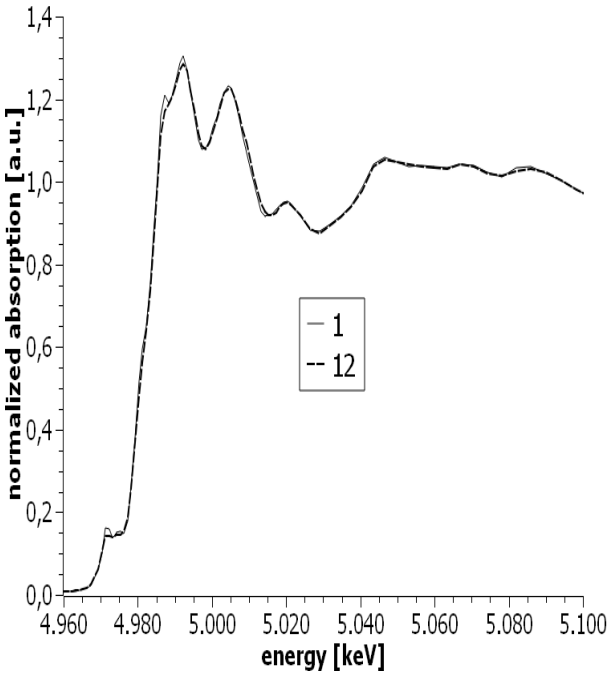

Figure 4.20: normalized Ti K edge XANES spectra of PtPd_4TiO2+TKKE. Numbers correspond to scan numbers ("1": before gas exposure, "12": 4.5h after)

Changes in Figure 4.19 and Figure 4.20 are within error limits meaning that both Ta and Ti atoms were not reduced under the conditions applied here: exposure to the reduction gas at up to 45.5ml/min at room temperature for up to 6h.

Pt LIII edge XANES spectra of two PtPd catalysts supported on doped C(TKKE)-TiO_2 hybrid supports show that Pt atoms in both samples were (partially?) oxidized before the start of the reduction experiments. The sheer presence of the reducing gas (3.7% H_2 / He as a carrier gas) was sufficient to reduce the Pt atoms completely. Their complete re-oxidation was unsuccessful - even at harsher conditions (longer exposure to air, temperature up to 120°C). Results strongly indicate that Pt atoms in this kind of sample show low affinity for oxidation. This conclusion is based on the fact that two batches of the second sample were oxidized to a different extent. Moreover, Pt atoms could not be completely re-oxidized. Ta and Ti atoms were tested under reducing conditions as well but show no changes.

4.3. Characterisation of PLAL Pt NPs

In this chapter the particle-solvent interaction of laser-generated Pt NPs in water, a sodium citrate solution, and a sodium buffer solution was characterized *in situ*. Additionally, the impact of depositing PLAL Pt NPs onto TiO_2 NPs on the structure of the former was studied. Results are compared to those of similar samples synthesized wet-chemically.

4.3.1. General information

The major difference of PLAL compared to traditional wet-chemical synthesis routes is that the former creates NPs without a strongly bound ligand-layer, which circumvents the necessity of having to remove it. These "purification steps" [78] can result in particle growth [11] (and ultimately loss of surface area) or phase separation in alloys [40]. For catalyst particles both effects lead to a decrease in catalytic activity.

PLAL NPs have partially oxidized surfaces [79] to which, in a solution, negative ions bind until the initially positive surface charge is overcompensated [80]. This situation can be best described by the Stern model in which particles in a solution have an electrical double layer. Ions adsorbed directly on the particle surfaces form the stationary layer to which a diffuse layer is bound. The diffuse layer is formed of ions and molecules only loosely attached due to thermal motion [81]. Differently charged species create a potential that decreases linearly from the particle surfaces to the outside of the stationary layer then exponentially to zero through the diffuse layer.

Up till now, information about the surface characteristics of PLAL NPs and their interactions with different solvents as well as supports were gathered by XPS and zeta potential measurements [82]. The zeta potential is defined as the potential on the outside of the diffuse layer. From XPS spectra one can obtain information about the charge density at particle surfaces (= different oxidation states of atoms in the outermost layers and their relative concentrations). The zeta potential on the other hand is an important parameter to quantitatively describe the stability of particles in a solution but is "relatively insensitive to specific ion adsorption at the fixed stern layer […]" [82]. A higher value means stronger electrostatic repulsion between adjacent particles, thus preventing agglomeration.

XAFS gives complementary information about the interaction of PLAL NPs with solvent species and supports. Compared to XPS, XANES spectra have the advantage that the specific bonding environment of an element of interest can be studied, *i.e.* one cannot only tell that molecules are bound to particle surfaces but one might even be capable of narrowing it down to which one(s). From EXAFS spectra one can obtain additional qualitative and quantitative information about atoms bound to particle surfaces, if one is dealing with sufficiently small particle sizes.

4.3.2. Unsupported samples

In this section the Pt NP surface-solvent interaction in water and the impact of adding citrate and phosphate ions are discussed. Figure 4.21a compares the normalized XANES spectra of the three unsupported PLAL samples to the one of a Pt reference foil. Between 13 and 33 individual scans were averaged for one spectrum. The inset shows just the whiteline region. Figure 4.21b shows the k^1-weighted EXAFS Fourier transform magnitudes of the same samples. Data are not phase-corrected meaning that peak positions are at smaller distances than actual bond lengths.

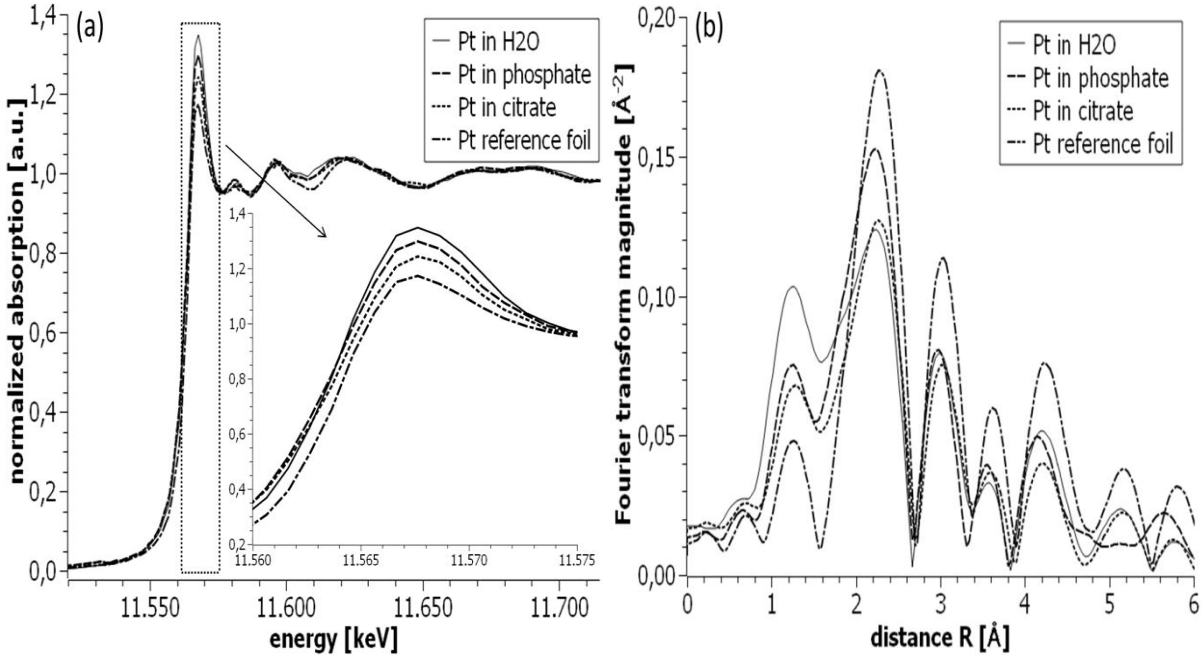

Figure 4.21: (a) normalized Pt LIII edge XANES spectra of the three unsupported PLAL samples and a Pt reference foil. Inset: whiteline regions. (b) k^1-weighted EXAFS Fourier transform magnitudes (dk = 1.0, dr = 0.0, Hanning window), not phase-corrected

The bump at about 11,530eV in the Pt in citrate/phosphate spectrum is due to experimental reasons and does not stem from the respective sample. Differences and similarities are now discussed in greater detail (Figure 4.21a):

(i) The whiteline intensity increases in the following order:

Pt foil < Pt in citrate < Pt in phosphate < Pt in H2O

From this one can deduce that PLAL NPs do not interact similarly with the species in their respective solution. Now what does this interaction look like? One can rule out Pt-H bonds because these would result in a broadening and intensity decrease of the whiteline [83], which is not the case here. This leaves bonds between Pt surface atoms and one or more O-containing species. As was already established in chapter 4.3.1, PLAL NPs have partially oxidized surfaces at which, in H_2O, Pt-OH and Pt-O^- species are formed [79], [80]. It is thus (reasonably) assumed that these are responsible for the whiteline intensity of the Pt in H2O sample. When adding citrate/phosphate one can observe a decrease in whiteline intensity, which means that Pt surface atoms are reduced. The most plausible scenario is that citrate/phosphate species bind to the outside of the particles' stationary layer, thus weakening their Pt-OH bonds.

(ii) The whiteline widths and intensities follow the same trend. The reason for this is an overlap of the particles' Pt 5d bands with O $2\pi^*$ anti-bonding orbitals "forming an antibonding state above the Fermi level" [84]. As the interaction of Pt surface atoms with the respective stationary layer increases in strength, this effect gets more pronounced.

(iii) Post-edge regions of the three unsupported PLAL samples closely resemble each other and the one of the Pt reference foil, indicating that the former have the same local geometric structure: fcc (face-centered cubic). The fact that peaks of the nano sample spectra are shifted to slightly different energies and are wider, compared to the reference, is a consequence of different Pt-Pt bond lengths and larger mean-square displacements. Surface relaxation effects are one possible explanation for that. NP surface atoms are under-coordinated, causing the bonds between surface/core atoms to contract in order to minimize the surface energy [85]. The close spectral resemblance nonetheless speaks for a high degree of crystallinity in the three nano-samples.

(iv) EXAFS Fourier transform magnitudes (Figure 4.21b) confirm the XANES finding that the three nano-samples have fcc structure, because their features closely resemble the ones of the reference foil. The decreased peak intensity is a particle size effect since it is proportional to the coordination number. The peak at 1.2Å is more intense in case of the nano-samples. It results from photoelectrons being backscattered by low-Z elements like C, N or O. Considering the synthesis, O is the most probable binding partner of Pt atoms in all three unsupported PLAL samples. The intensities of the 1.2Å peak follow the same trend as the whiteline intensities suggesting that a different number of Pt-O bonds are responsible.

The Pt in phosphate spectrum deviates from all other spectra for distances > 4.7Å suggesting a different local geometric structure. Yet, this conclusion is contradicted by the corresponding XANES post-edge regions which closely resemble each other (Figure 4.21a). It is thus assumed that the worse data quality of the Pt in phosphate spectrum is responsible for this observation.

In Table 4.6 EXAFS fit results of the samples portrayed in Figure 4.21 are summarized:

Table 4.6: summary of Pt LIII edge EXAFS fit results of the three unsupported PLAL samples and a Pt reference foil. N(Pt)/N(O) is the number of Pt-Pt/Pt-O bonds, ΔE aligns the experimentally determined edge energy with the one used in the calculation, R(Pt-Pt)/R(Pt-O) is the average Pt-Pt/ Pt-O bond length, σ^2 Pt-Pt/σ^2 Pt-O is the mean-square displacement of the Pt/O atom in a Pt-Pt/Pt-O bond, σ^3 Pt-O is the third cumulant-expansion parameter of the Pt-O bonds, "f" refers to the parameter kept fixed for the final fit.

Δk: 2 – 8.5, ΔR = 0.7 – 3.4Å, number of data points = 10.4-10.8, number of variables = 6				
	Pt foil	**Pt in H2O**	**Pt in citrate**	**Pt in phosphate**
N (Pt)	12	12.0 ± 0.7	12.1 ± 0.7	13.1 ± 1.0
N (O)	0	2.0 ± 0.2	1.5 ± 0.3	1.7 ± 0.5
ΔE [eV]	7.9 ± 0.4	5.6 ± 0.8	7.0 ± 0.7	5.4 ± 1.2
R(Pt-Pt) [Å]	2.75 ± 0.01	2.73 ± 0.01	2.75 ± 0.01	2.73 ± 0.01
R(Pt-O) [Å]	/	2.15 ± 0.03	2.12 ± 0.04	2.16 ± 0.07
σ^2 [10^3 Å^2] Pt-Pt	5.1 ± 0.1	6^f ± 2	6^f ± 2	4^f ± 3
σ^2 [10^3 Å^2] Pt-O	/	5^f ± 6	12^f ± 13	10^f ± 19
σ^3 [10^3 Å^2] Pt-O	/	8 ± 1	5 ± 3	8 ± 4

What can be learned from these results is that the respective samples are very similar to each other taking into account measurement uncertainties. These are rather large, because of the short data sets and thus fit ranges. Results from Table 4.6 nonetheless suggest that addition of citrate/phosphate does not alter the local geometric structure of the Pt NPs in H_2O and especially not their surfaces.

Pt LIII edge XANES spectra showed that the stationary layer of Pt NPs in H_2O consists of Pt-OH and Pt-O^- species. Adding citrate/phosphate species weakens the interaction of the particle surfaces with this stationary layer. Post-edge regions show that Pt NPs in all three unsupported PLAL samples have fcc structure, which is confirmed by their corresponding EXAFS spectra.

These results are now compared to those from Pt NPs synthesized wet-chemically. The Pt in citrate spectrum is chosen as representative of the PLAL samples and the spectrum of Pt NPs in ethylene glycol as representative of wet-chemical synthesis (Figure 4.22a). The inset shows

just the whiteline region. Figure 4.22b shows the k^1-weighted EXAFS Fourier transform magnitudes of both samples. Data are again not phase-corrected.

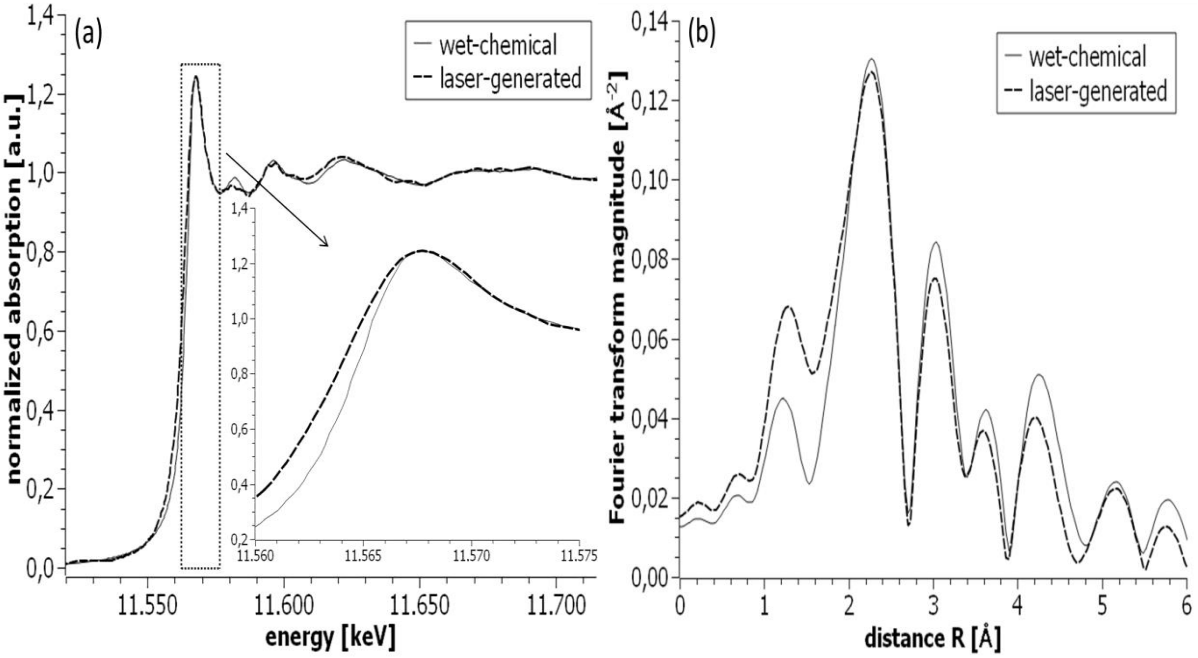

Figure 4.22: (a) normalized Pt LIII edge XANES spectra of wet-chemically synthesized Pt in ethylene glycol and laser-generated Pt in citrate. Inset: whiteline regions. (b) k^1-weighted EXAFS Fourier transform magnitudes (dk = 1.0, dr = 0.0, Hanning window), not phase-corrected

The same aspects as discussed for the three unsupported PLAL samples are now discussed again (Figure 4.22a):

(i) The whiteline intensities are, analogous to the last section, interpreted as an indicator of the particle-solvent interaction strength. The fact that the whiteline intensities of both samples are identical in the range of error is accordingly interpreted as this interaction being equally strong in both samples. Beforehand one would assume the particle-solvent interaction to be stronger in case of the wet-chemical sample, so this observation is rather surprising! One possible explanation is that Pt NPs in this sample were synthesized without an additional stabilizer, resulting in a weaker particle-solvent interaction.

(ii) The whiteline of the PLAL sample is wider compared to the one of the wet-chemical sample. This finding can be reasonably attributed to experimental reasons since both spectra were recorded on different beamlines with different monochromator crystals; a different energy resolution is thus to be expected.

(iii) The spectral resemblance in the post-edge region between PLAL and wet-chemical Pt NPs strongly suggests the latter having fcc structure as well and a very similar degree of crystallinity.

(iv) EXAFS spectra closely resemble each other confirming both conclusions (Figure 4.22b). Most differences are within the margin of error except the 1.2Å peak which is more intense

for the PLAL sample indicating a higher number of Pt-O bonds. This assumption is confirmed by EXAFS fit results (Table 4.7):

Table 4.7: summary of Pt LIII edge EXAFS fit results of wet-chemical and PLAL Pt NPs ("f" refers to the parameter kept fixed for the final fit)

Δk: 2 – 9.8, ΔR = 0.7 – 3.4Å, number of data points = 10.1-10.9, number of variables = 6		
	wet-chemical (in ethylene glycol)	**PLAL (in citrate)**
N (Pt)	10.9 ± 0.5	12.1 ± 0.7
N (O)	0.5 ± 0.1	1.5 ± 0.3
ΔE [eV]	7.4 ± 0.5	7.0 ± 0.7
R(Pt-Pt) [Å]	2.75 ± 0.01	2.75 ± 0.01
R(Pt-O) [Å]	2.11 ± 0.05	2.12 ± 0.04
σ^2 [10^3 Å^2] Pt-Pt	6^f ± 2	6^f ± 2
σ^2 [10^3 Å^2] Pt-O	2^f ± 11	12^f ± 13
σ^3 [10^3 Å^2] Pt-O	8 ± 3	5 ± 3

EXAFS fit results confirm the visual impression that the number of Pt-O bonds is lower for the wet-chemical compared to the PLAL sample (after addition of citrate!) even though both show identical whiteline intensities (Figure 4.22a). How can this be explained? No information about the average oxidation states in either sample can be deduced from whiteline positions because chemical shifts are small for any platinum oxide (PtO, Pt_3O_4, PtO_2) [86]. Whiteline intensities are thus the only indicators of average oxidation states. The most plausible explanation for this discrepancy assumes predominantly Pt(IV)O_2-type bonds on the surface of wet-chemical NPs and Pt(II)O-type bonds on the surface of the PLAL NPs. At least for the latter this hypothesis is supported by XPS results where mostly Pt(0) and Pt(II)-O bonds were fitted [Fischer, M; Hormes, J.; Marzun, G.; Wagener, P., Barcikowski, S; submitted for publication]. The strength of the Pt-O interaction is hereby compensated by the number of Pt-O bonds, *i.e.* the lower number of stronger Pt(IV)-O bonds and higher number of weaker Pt(II)-bonds eventually produce the same whiteline intensity.

4.3.3. TiO_2-supported samples

Figure 4.23a compares the normalized XANES spectra of the PLAL samples Pt in H2O and Pt on TiO2. According to the manufacturer, TiO_2 is present as anatase, which was confirmed by XANES analysis (data not shown). 16 and 26 individual scans were averaged for one spectrum. Figure 4.23b shows the k^1-weighted EXAFS Fourier transform magnitudes of both samples. Data are again not phase-corrected.

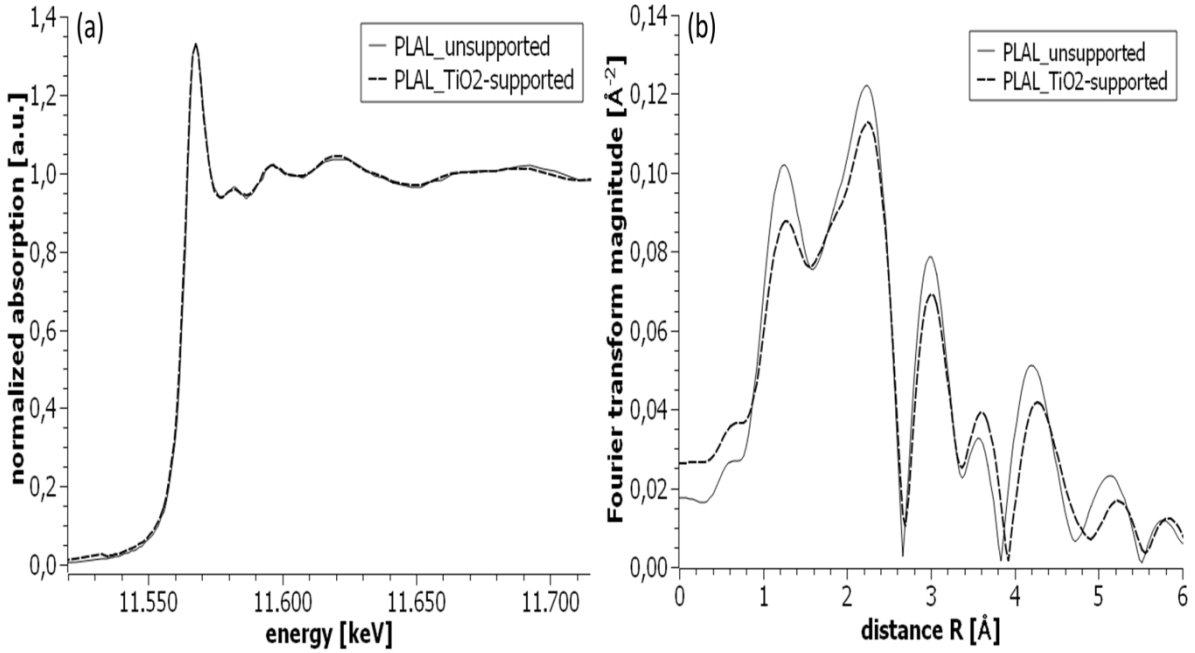

Figure 4.23: (a) normalized Pt LIII edge XANES spectra of the PLAL samples Pt in H2O and Pt on TiO2. (b) k^1-weighted EXAFS Fourier transform magnitudes (dk = 1.0, dr = 0.0, Hanning window), not phase-corrected

All differences between the two XANES spectra are within the margin of error. This means that the deposition process has no measurable impact on the electronic and geometric structure of the Pt NPs. Both components, Pt and TiO_2 NPs, had a solvent layer before the deposition process, and it is safe to assume that neither of them loses it during deposition. This means that there is no direct Pt-TiO_2 interaction (= no covalent bonds between Pt and TiO_2), which is not surprising since no proper high temperature calcination took place; a hypothesis that is supported by literature (*e.g.* [87]) and by looking at similar samples synthesized wet-chemically. Figure 4.24a compares, to this end, the wet-chemical samples Pt in ethylene glycol and Pt on 1TiO2. Figure 4.24b shows the k^1-weighted EXAFS Fourier transform magnitudes of both samples. Data are again not phase-corrected.

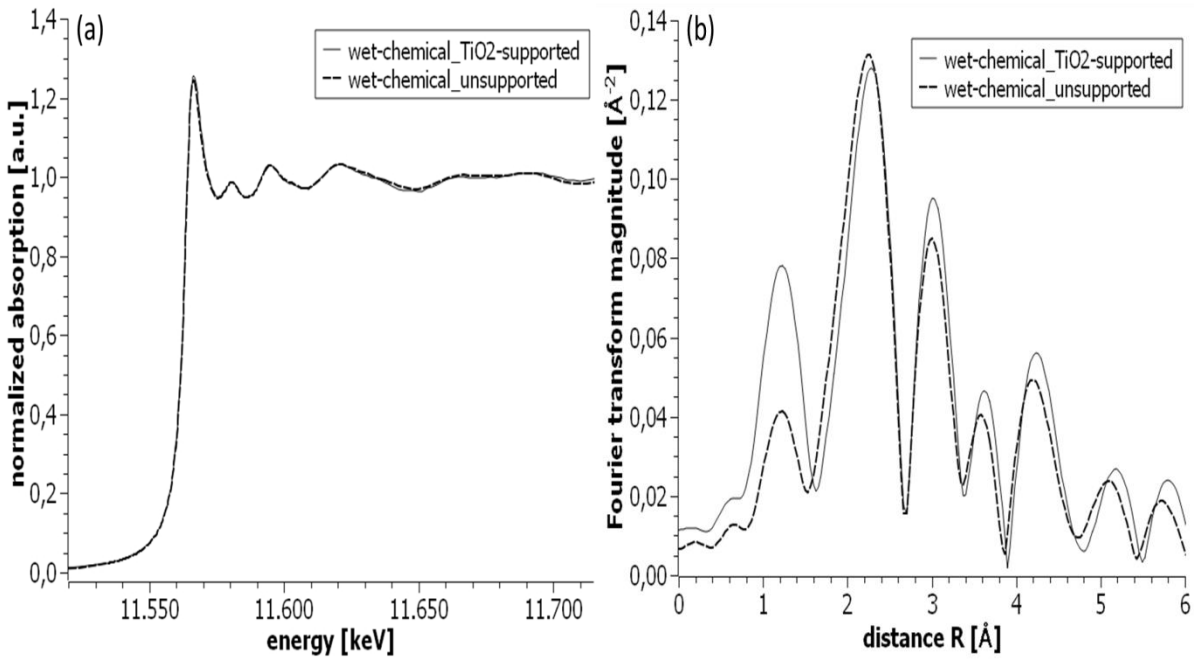

Figure 4.24: (a) normalized Pt LIII edge XANES spectra of the wet-chemical samples Pt in ethylene glycol and Pt on 1TiO2. (b) k^1-weighted EXAFS Fourier transform magnitudes (dk = 1.0, dr = 0.0, Hanning window), not phase-corrected

The identical whiteline intensities of the wet-chemical samples Pt in ethylene glycol and Pt on 1TiO2 support the hypothesis put forward in the last section that without proper calcination no changes in the electronic structure of Pt NPs occur upon depositing them on a TiO_2 support. The higher loading in case of the wet-chemical compared to the PLAL sample (20 vs. 2wt%!) is another piece of evidence for this hypothesis. It should not go unmentioned that depositing laser-generated Pt onto commercial TiO_2 NPs (Hombikat) was also done by Marzun et al. [22]. In this work, measurements of zeta potentials and isoelectric points (IEP) of Pt and TiO_2 NP solutions were performed before and after mixing. It was found that the deposition process caused a net charge transfer noticeable because the IEP of the mixture was between the one of the individual components. Combining the results from this paper with the ones gathered in this work two conclusions were drawn: (1) both the Pt and TiO_2 NPs have a protective layer in their respective solution which are combined upon deposition. (2) Deposition does not alter the electronic structures of Pt and TiO_2 particles.

EXAFS data of PLAL and wet-chemical samples (Figure 4.23b and Figure 4.24b) show a close spectral resemblance between un- and TiO_2-supported samples meaning that the deposition process does not have a significant impact on the geometric structure of Pt NPs either - regardless of the synthesis route. The only significant difference is the increased 1.2Å peak intensity in case of the wet-chemical Pt on 1TiO2 compared to the Pt in ethylene glycol spectrum. One possible explanation is a higher number or a different character of Pt-O bonds.

From previous XPS and zeta potential studies it was already established that the particle-solvent interaction of PLAL NPs can best be described by the Stern model: particle surfaces are partially oxidized. In a solvent this surface charge is overcompensated by the adsorption of negative ions (Pt-OH and Pt-O^-) forming the stationary layer to which ions and molecules bind loosely thus forming the diffuse layer. Stabilization of PLAL NPs is thus mainly guaranteed through electrostatic repulsion of adjacent particles.

Pt LIII edge whiteline intensities are an indicator of the particle-solvent interaction strength. They show that the phosphate and citrate ions added *ex situ* adsorb to the outside of the stationary layer and thus weaken its bonds to the Pt NP surfaces. XANES spectra also show that Pt NPs in all three unsupported PLAL samples have fcc structure with a high degree of crystallinity (deviations from the bulk most likely caused by surface effects). EXAFS results confirm that. A comparison of unsupported PLAL (in citrate) and wet-chemical Pt NPs (in ethylene glycol) show strong indications that the former predominantly have Pt(II)O-type bonds on their surfaces, whereas these are Pt(IV)O_2-type bonds in the case of wet-chemical NPs; a conclusion which is supported by XPS results for the PLAL sample. The deposition process turned out to have little to no effects on the electronic and geometric structure of PLAL as well as wet-chemical Pt NPs, and the latter showed small differences due to either a change in number or character of the Pt-O bonds. This means that for both (fundamentally different!) synthesis routes the solvent layer stays intact during the deposition process which is most likely due to the fact that no high-temperature calcination was done.

5. Summary and outlook

(One) Samples in this part were one Ta-/Nb- co-doped single TiO_2 support, two C-TiO_2 hybrid and one C-TiO_2 core-shell support. Two kinds of carbon black were used: C(KB) (Ketjenblack EC-600JD by AkzoNobel [21]) as well as C(TKKE). "TKKE" is the E-type carbon black by Tanaka Kikinzoku International (America) Inc. The goal of the experiments was to determine how (in which chemical state) and where (at which crystallographic position(s)) dopants were incorporated into the respective TiO_2 host structure and how that impacted these structures. Additionally, I examined a possible catalyst-dopant interaction.

XANES data show that TiO_2 is predominantly present as anatase in the two samples containing C(KB) and as rutile in the three that don't. The local geometric structure of Ta atoms in all five samples resembles the one of the mineral tantalite despite differing chemical compositions. XANES data further show that both dopants replaced Ti atoms in the TiO_6 octahedra and are statistically distributed in all five samples, which was the goal of the synthesis. EXAFS analysis confirms this conclusion and also revealed that Nb incorporation did distort the TiO_2 host structure of at least one sample to a greater extent compared to Ta incorporation. XANES results strongly indicate an interaction of both dopants with the carbon supports as well as the Pt catalyst, most likely via dopant-O-C/Pt bonds. The core-shell support displays the highest degree of disorder and smallest particle size, which is most likely correlated. There is evidence that the highest degree of disorder is a consequence of the manufacturing and not the doping process.

It should be stressed that the idea behind doping was to increase the electronic conductivity of the semiconductor TiO_2 by providing additional electrons. Based on the XANES results it looks like this did not happen. However, measurements of the group that provided the samples showed that doping actually does show the desired effect. Further studies are necessary to resolve this contradiction.

At the time of writing this the best catalyst (of the group of PEM catalysts characterized in this work) regarding durability, and ORR mass activity is 20wt% (0.62Pt0.38Pd) on core-shell $(0.04Ta0.06Nb0.90Ti)O_2$ + C(KB) (which is the sample 4TiO2+KB2 I characterized here). Ta-/Nb- co-doping hereby increases the conductivity and durability of the TiO_2 support and eventually the ORR mass activity of the PtPd-C/TiO_2 catalyst-support unit ([38], [88], personal correspondence]. The core-shell support is superior to the hybrid support of identical chemistry and the commercially available 47wt% Pt on C(TKKE) for two reasons (taken from [38], [88]): (1) Highest durability: the TiO_2 shell protects the C core from oxidation, thus

preventing agglomeration of catalyst particles and therefore loss of electrochemically active surface area. Also, the interaction of C(KB) with TiO_2 seems to be stronger if the latter is present as anatase - as is the case for samples containing C(KB) as opposed to C(TKKE) where TiO_2 is present as rutile. (2) Higher ORR mass activity: this seems to be a consequence of the best catalyst-support interaction, though is it not completely understood at this point what "best" means. I hypothesize that the structure of TiO_2 particles (smallest particle size and highest degree of disorder) makes the 20wt% (0.62Pt0.38Pd) on core-shell $(0.04Ta0.06Nb0.90Ti)O_2$ + C(KB) sample the best catalyst-support unit given superior electrochemical performance compared to its hybrid counterpart.

(Two) Their increased relative surface area makes nano-catalysts prone to oxidation which ultimately decreases their catalytic activity. Pt LIII edge XANES spectra of two PtPd catalysts supported on doped C(TKKE)-TiO_2 hybrid supports show that Pt atoms in both samples were (partially?) oxidized before the start of the reduction experiments. The sheer presence of the reducing gas (3.7% H_2 / He as a carrier gas) was sufficient to reduce the Pt atoms completely. Their complete re-oxidation was unsuccessful - even at harsher conditions. Results strongly indicate that Pt atoms in this kind of sample show low affinity for oxidation. Ta and Ti atoms were tested under reducing conditions as well but show no changes.
In general, the sample chamber used here is a good choice for reduction/oxidation experiments. Yet, the reproducibility of temperature measurements should be improved by attaching the thermocouple firmly to the sample. Since the chemical compositions and structures of the selected samples are fairly unique I have doubts that the results gathered here are easily transferable.

(Three) Samples in this part were Pt NPs in water, a sodium citrate solution, a sodium buffer solution and TiO_2-supported Pt NPs all synthesized via PLAL (pulsed laser ablation in liquid). Of the first three their surface characteristics were characterized *in situ* and the respective particle-solvent interaction examined. The catalyst-support interaction was studied in the Pt-TiO_2 system. Results were compared to similar samples synthesized wet-chemically.
From previous XPS and zeta potential studies it was already established that the particle-solvent interaction of PLAL NPs can best be described by the Stern model, the stationary layer consisting of Pt-OH and $Pt\text{-}O^-$ species. Pt LIII edge XANES spectra confirm that for all three unsupported PLAL samples. They also show that the phosphate and citrate ions added *ex situ* adsorbed to the outside of the stationary layer and thus weakened its bonds to the Pt

NP surfaces. XANES spectra also show that Pt NPs in all three unsupported PLAL samples have fcc structure with a high degree of crystallinity. A comparison of unsupported PLAL and wet-chemical Pt NPs show strong indications that the former predominantly have Pt(II)O-type bonds on their surfaces, whereas these are Pt(IV)O_2-type bonds in the case of wet-chemical NPs; a conclusion which is supported by XPS results for the PLAL sample. The deposition process turned out to have little to no effects on the electronic and geometric structure of PLAL as well as wet-chemical Pt NPs, and the latter showed small differences due to either a change in number or character of the Pt-O bonds. This means that for both (fundamentally different!) synthesis routes the solvent layer stays intact during the deposition process which is most likely due to the fact that no high-temperature calcination was done.

X-ray absorption spectroscopy proved that it is a powerful tool to characterize all components of a modern fuel cell catalyst-support unit. Whereas previous studies focussed on the catalyst, this work concentrated on the support. To be precise: the impact of Ta-/Nb- co-doping on C-TiO_2 hybrid/core-shell supports as well as a Pt-TiO_2 catalyst-support unit. Combined with techniques that characterize macroscopic properties like electric conductivity or stability, XAFS is a tremendous help in understanding the interplay of the various components present nowadays in modern PEM fuel cell catalyst-support systems, especially considering that it is the only technique available today by which the electronic and geometric structure of an element of interest can be studied both *in situ* and even *in operando*. Further investigations in this direction will help this understanding and, eventually, lead to better catalyst systems.
XAFS investigations gave new insights into the particle-solvent as well as particle-support interaction of PLAL NPs. Given that this was the first time, to the best of my knowledge, that XAFS was applied to characterize PLAL NPs, future studies will deliver an even deeper insight in the products of this interesting alternative to traditional wet-chemical synthesis routes.

Appendix

A.1 XANES & EXAFS data handling

This section gives more detailed information about how XANES (using ATHENA) and EXAFS (using ARTEMIS) data were processed.

A.1.1 XANES

In order to be able to compare XANES spectra several steps have to be taken. Using the example of a Ta LIII edge spectrum of the sample 4TiO2, these steps are now explained in greater detail.

1. Raw data

Since 4TiO2 was measured in fluorescence one plots the fluorescence count of the Ta $L_{\alpha 1,2}$ emission line normalized by the beam intensity before the sample (Figure A1):

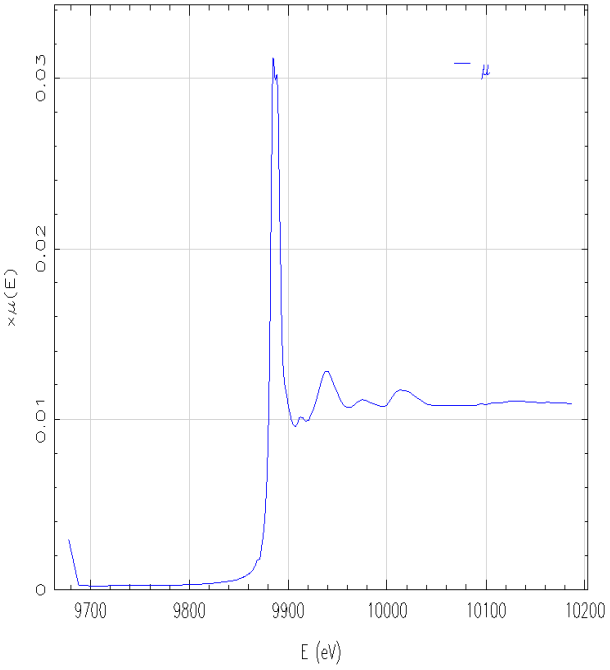

Figure A1: Ta LIII edge XANES spectrum of 4TiO2, raw data

2. Calibration

For calibration, a reference foil was measured simultaneously. Its edge position is determined by the inflection point method meaning that the edge energy is set in the inflection point of the sharp rise in an absorption spectrum. This point is determined by the maximum of the 1st derivative, which should correspond to the zero-crossing of the 2nd derivative (Figure A2). From the moment of importing data ATHENA already determined the edge energy. Its difference to the literature value is what both the sample and reference spectrum are now shifted by as soon as the edge energy of the reference is set to the literature value. In this work edge energies were taken from [46].

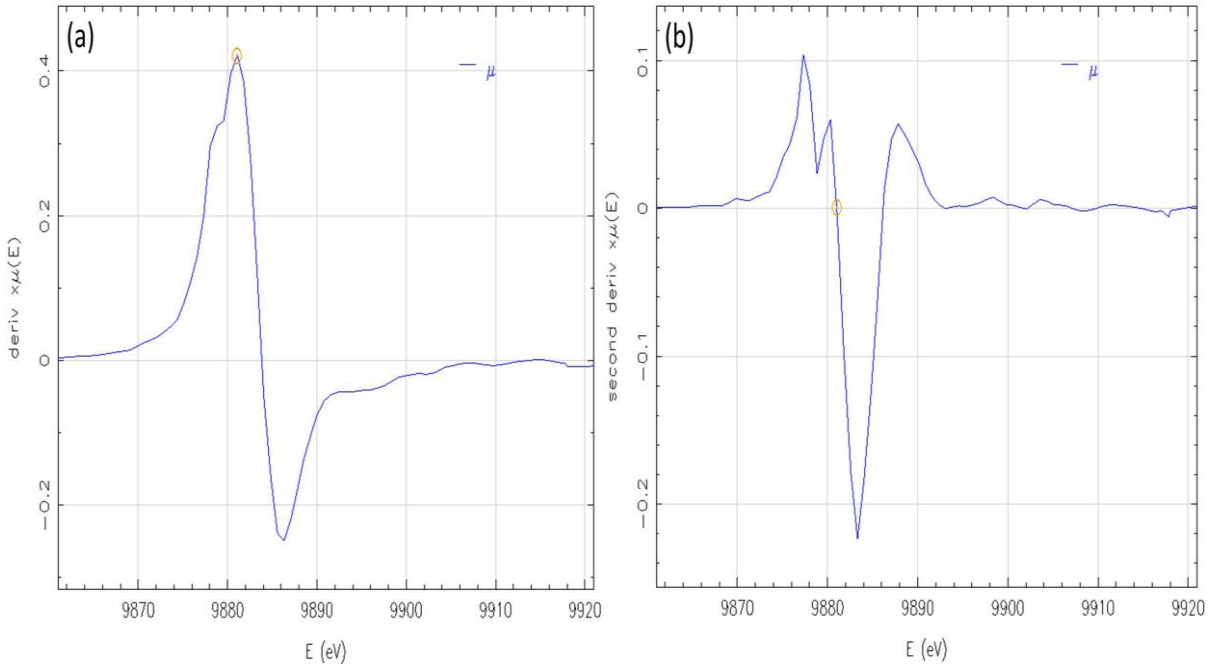

Figure A2: Ta LIII edge XANES spectrum of a Ta foil. (a) 1st, (b) 2nd derivative. The circles with the dot in their center mark the edge energy.

3. Alignment

Due to experimental reasons consecutive scans of the same sample need to be shifted towards each other. One example is that the first monochromator motor skipped a step. This is done for all reference spectra to the respective first one of a series which shifts the corresponding sample spectra accordingly.

4. Background subtraction/normalization

Every spectrum has a background caused by absorption of elements other than the one of interest and scattering. In ATHENA this is dealt with by manually adjusting a linear function to the pre-edge region and extrapolating as well as subtracting it from the whole spectrum. The result is then normalized by manually adjusting a second-order polynomial to the post-edge region. The ATHENA manual explains the necessity of this step: “Normalization is the process of regularizing your data with respect to variations in sample preparation, sample thickness, absorber concentration, detector and amplifier settings, and any other aspects of the measurement” [89]. Normalization thus makes spectra comparable. Example data together with the background and the normalization can be seen in Figure A3:

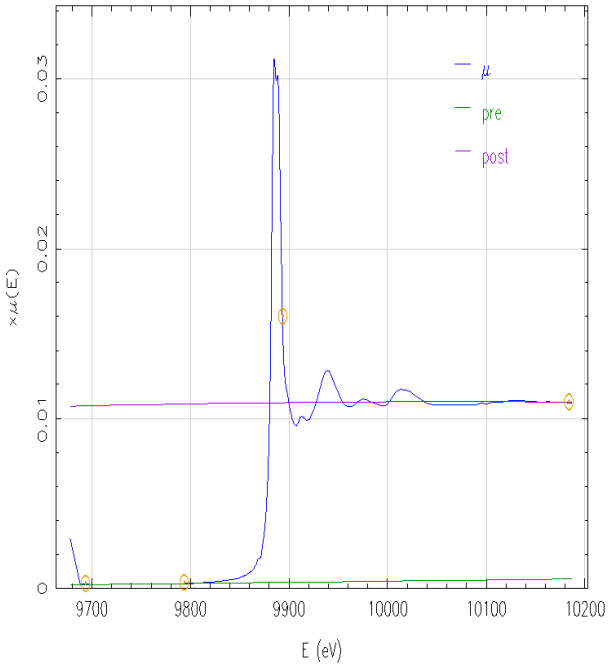

Figure A3: Ta LIII edge XANES spectrum of 4TiO2 including background subtraction (“pre”) and normalization (“post”). The circles with the dot in their center mark the beginning/end point between which background subtraction/normalization will be done.

The difference in absorption between the normalization and background line at the edge energy is called “edge jump”. When preparing a sample for transmission measurements one tries to get an edge jump of 1 because that gives an optimal signal-to-noise ratio.

5. Averaging

To increase the signal-to-noise ratio several spectra of the same sample are taken and averaged after applying steps 1 to 4 to each of them.

A.1.2 EXAFS

This section describes EXAFS data analysis more detailed. Parameters applied before and during the fit procedure are explained as well as statistical parameters given after a fit. For a better understanding, this procedure is now performed on Pt LIII edge data of a Pt foil.

1. Data extraction

EXAFS data are extracted using ATHENA and the approach described in chapter 2. Figure A4a shows Pt LIII edge data of a Pt foil together with the calculated background (one would get for an embedded atom if the interaction of the photoelectron waves with their neighbours could be turned off). Figure A4b gives the corresponding extracted EXAFS data:

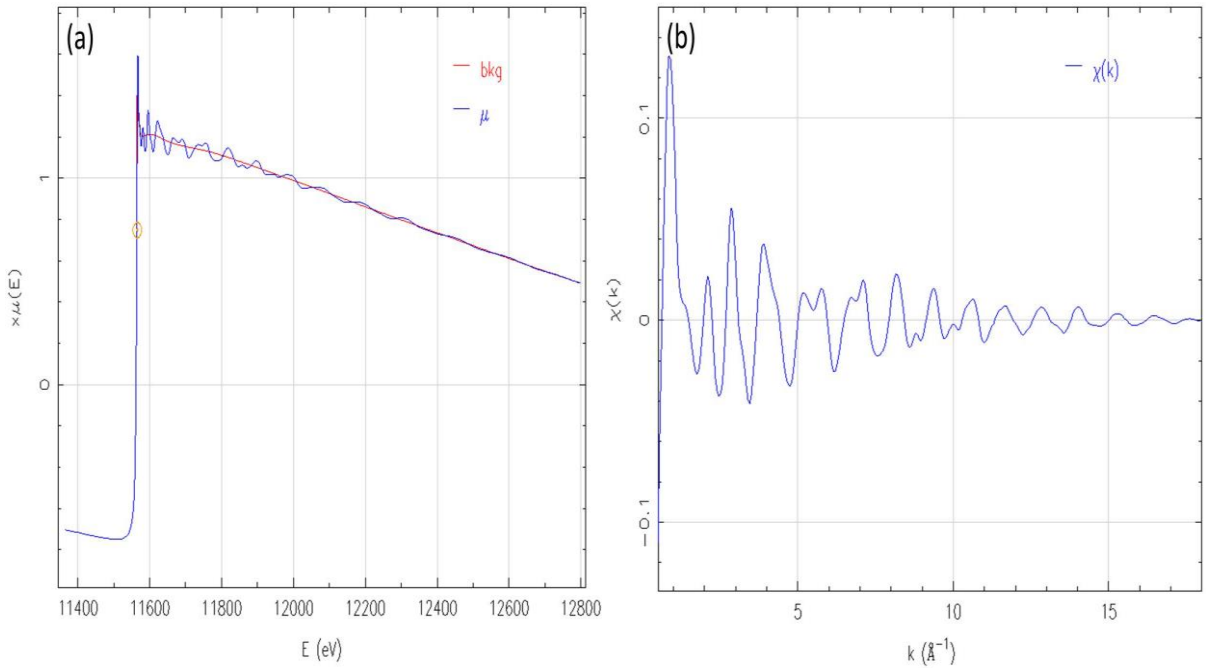

Figure A4: (a) Pt LIII edge data of a Pt foil including the background, (b) extracted EXAFS data as a function of the wavenumber k

2. k-weights and Fourier transform

Lighter elements contribute to the EXAFS data strongest at lower k-values whereas heavier elements contribute more at higher k-values [29]. Applying an appropriate k-weight (multiplying it with the data before a fit) emphasizes different parts of EXAFS data thus making better use of their information content. Since only heavy Pt atoms are present in this example a k^3-weight was applied. Before it can get Fourier transformed one needs to apply a window function. A Fourier transform expects an infinite signal which obviously is rarely given in a real life experiment. To prevent so-called “ripples”, EXAFS data are multiplied with a window function [28]. Ripples are an additional signal at higher R-values not stemming from and thus masking the signal of a sample. What a window function does is to put emphasis on the middle part of an EXAFS spectrum (where the signal is strongest) and gradually cuts out the edges (where the signal is weakest). How smoothly that is done is

determined by the dk value (“window sill”). In this work, a Hanning window with a dk value of 1.0 was used (Figure A5a). Since the EXAFS equation is complex there are several ways it can be plotted. As an example, Figure A5b shows the magnitude, which is the most common one:

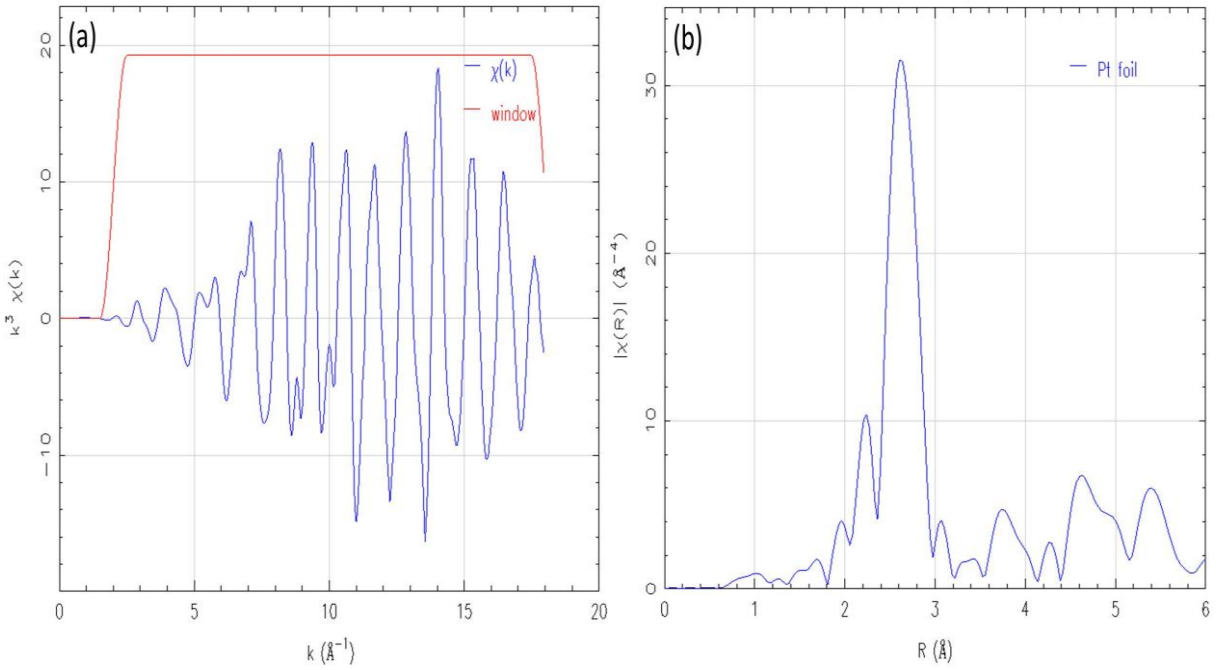

Figure A5: k^3-weighted EXAFS data of a Pt foil including a Hanning window (dk = 1.0) (a) in k-space and (b) the corresponding Fourier transform magnitude in R-space

3. Structural model

Just like XANES spectra finger-printing can be applied to EXAFS data or different k-weight compared in order to get rough information. Yet, the most fertile approach is to fit an EXAFS spectrum. To do so, one first has to get a structural model. For the Pt foil data it was downloaded from the ATOMS archive [49]. With the information space group, lattice parameters and atom(s) in the unit cell (and their respective relative coordinates) the program ATOMS calculates the absolute positions of all atoms in a cluster of a given size. Parts of an output file for a 6Å platinum cluster can be seen in Figure A6 (atoms beyond the first shell were truncated for clarity):

```
* This feff6 input file was generated by Artemis 0.8.014
* Atoms written by and copyright (c) Bruce Ravel, 1998-2001

* -- * -- * -- * -- * -- * -- * -- * -- * -- * -- * -- * -- * -- * -- *
*   total mu*x=1:     2.42 microns,  unit edge step:     4.11 micror
*   specific gravity = 21.512
* -- * -- * -- * -- * -- * -- * -- * -- * -- * -- * -- * -- * -- * -- *
*   Normalization correction:    0.00043 ang^2
* -- * -- * -- * -- * -- * -- * -- * -- * -- * -- * -- * -- * -- * -- *

* ------------------------------------------------------------------
* The following crystallographic data were used:
*
* title        name:     platinum
* title        formula:  Pt
* title        sites:    Pt1
* title        refer1:   Kittel, ISSP
* title        refer2:
* title        schoen:
* title        notes1:   metal, fcc
* space = F m -3 m
* a =    3.920 b =       3.920 c =       3.920
* alpha =       90.0   beta =   90.0   gamma =  90.0
* core =       Pt1     edge =  L3
* atoms
* ! elem   x          y          z       tag         occ
*   Pt    0.00000    0.00000    0.00000  Pt1           1.00000
* ------------------------------------------------------------------


TITLE name:     platinum
TITLE formula:  Pt
TITLE sites:    Pt1
TITLE refer1:   Kittel, ISSP
TITLE refer2:
TITLE schoen:
TITLE notes1:   metal, fcc

HOLE 4   1.0   *  Pt L3 edge  (11564.0 eV), second number is S0^2

*         mphase,mpath,mfeff,mchi
CONTROL   1      1     1     1
PRINT     1      0     0     0

RMAX        6.0

*CRITERIA     curved   plane
*DEBYE        temp     debye-temp
NLEG         4

POTENTIALS
*    ipot   Z  element
       0   78   Pt
       1   78   Pt

ATOMS                          * this list contains 55 atoms
*   x          y          z      ipot  tag              distance
   0.00000    0.00000    0.00000  0 Pt1              0.00000
   1.96000    1.96000    0.00000  1 Pt1_1            2.77186
  -1.96000    1.96000    0.00000  1 Pt1_1            2.77186
   1.96000   -1.96000    0.00000  1 Pt1_1            2.77186
  -1.96000   -1.96000    0.00000  1 Pt1_1            2.77186
   1.96000    0.00000    1.96000  1 Pt1_1            2.77186
  -1.96000    0.00000    1.96000  1 Pt1_1            2.77186
   0.00000    1.96000    1.96000  1 Pt1_1            2.77186
   0.00000   -1.96000    1.96000  1 Pt1_1            2.77186
   1.96000    0.00000   -1.96000  1 Pt1_1            2.77186
  -1.96000    0.00000   -1.96000  1 Pt1_1            2.77186
   0.00000    1.96000   -1.96000  1 Pt1_1            2.77186
   0.00000   -1.96000   -1.96000  1 Pt1_1            2.77186
```

Figure A6: ATOMS output file, atoms beyond the first shell were truncated for clarity

If there is no structural model available, *e.g.* in case of doping, one has to pick an ATOMS output file which resembles the desired one as closely as possible and modify it. The procedure is now demonstrated for replacing two Pt 1st shell atoms by N atoms as was done in chapter 4.1.5: (1) under "POTENTIALS" one has to add a third line with contains a 2 under "ipot", a 8 under "Z" and a N under "element". (2) under "ATOMS" one has to replace two "Pt1_1" by *e.g.* "N1_1".

Next, the program FEFF calculates single and multiple scatterings paths (ways photoelectrons can take before returning to the absorber atoms), their degeneracies (number of symmetrically equivalent paths) as well as relative intensities and lists them with increasing distance to the absorber atoms. Contributions of a higher than 4th order are neglected meaning that photoelectrons are scattered up to 3 times. A FEFF output file can be seen in Figure A7:

#	Deg.	Reff	amp.	fs	Scattering Path
1	12	2.772	100.00		[+] Pt1_1 [+]
2	6	3.920	25.07		[+] Pt1_2 [+]
3	48	4.158	16.20		[+] Pt1_1 Pt1_1 [+]
4	48	4.732	6.57		[+] Pt1_2 Pt1_1 [+]
5	24	4.801	59.87		[+] Pt1_3 [+]
6	48	5.172	10.90		[+] Pt1_1 Pt1_1 [+]
7	96	5.172	34.12		[+] Pt1_3 Pt1_1 [+]
8	12	5.544	19.97		[+] Pt1_4 [+]
9	12	5.544	8.53		[+] Pt1_1 Pt1_1 [+]
10	24	5.544	85.24	1	[+] Pt1_4 Pt1_1 [+]
11	12	5.544	15.44	1	[+] Pt1_1 [+] Pt1_1 [+]
12	12	5.544	3.53		[+] Pt1_1 [+] Pt1_1 [+]
13	48	5.544	5.34		[+] Pt1_1 [+] Pt1_1 [+]
14	12	5.544	91.47	2	[+] Pt1_1 Pt1_4 Pt1_1 [+]
15	48	5.544	5.11		[+] Pt1_1 Pt1_1 Pt1_1 [+]
17	48	5.544	11.06		[+] Pt1_1 Pt1_3 Pt1_1 [+]
20	48	5.746	3.23		[+] Pt1_3 Pt1_2 [+]

Figure A7: information returned from FEFF ("Deg" stands "degeneracy" = the number of symmetrically equivalent scatterings paths, "Reff" is the effective distance from absorber to neighbouring atoms = the distance photoelectrons travel divided by the times they get scattered when having returned to the absorber atom, "amp" is the amplitude relative to the strongest scattering path = first single-scattering path, "fs" is the number of forward scattering events, "scattering path" describes the way the photoelectrons took before returning to the absorber atoms)

The backscattering amplitude and phase of the atoms surrounding the Pt absorber atoms as well as the mean free path are hereby calculated.

How the fit process works is now described for the 1st shell of the Pt foil data using the first single-scattering path. Fit parameters were the amplitude reduction factor S_0^2, ΔE to align the

experimental and theoretical edge energies, ΔR to account for variations in Pt-Pt bond lengths and their mean-square displacement parameter σ^2. Numbers of next neighbours N was set to the crystallographic value of 12 which can be expected in a foil. This adds up to 4 fit parameters and 13.7 independent data points. The latter were calculated using the Nyquist theorem [28]:

$$N_{IP} = \frac{2}{\pi}\Delta k \Delta R + 1$$

"N_{IP}", "Δk" and "ΔR" stand for the number of independent data points, the k-range used for the Fourier transform and the R-range used for a fit. The Nyquist theorem estimates the information content of a given data set. A rule of thumb is that the number of independent data points should be at least double the number of fit parameters; a condition that was met here. The fit was done in R-space with a k^3-weighting. Data and fit can be seen in Figure A8a (k-space, back Fourier transformed) and Figure A8b (R-space):

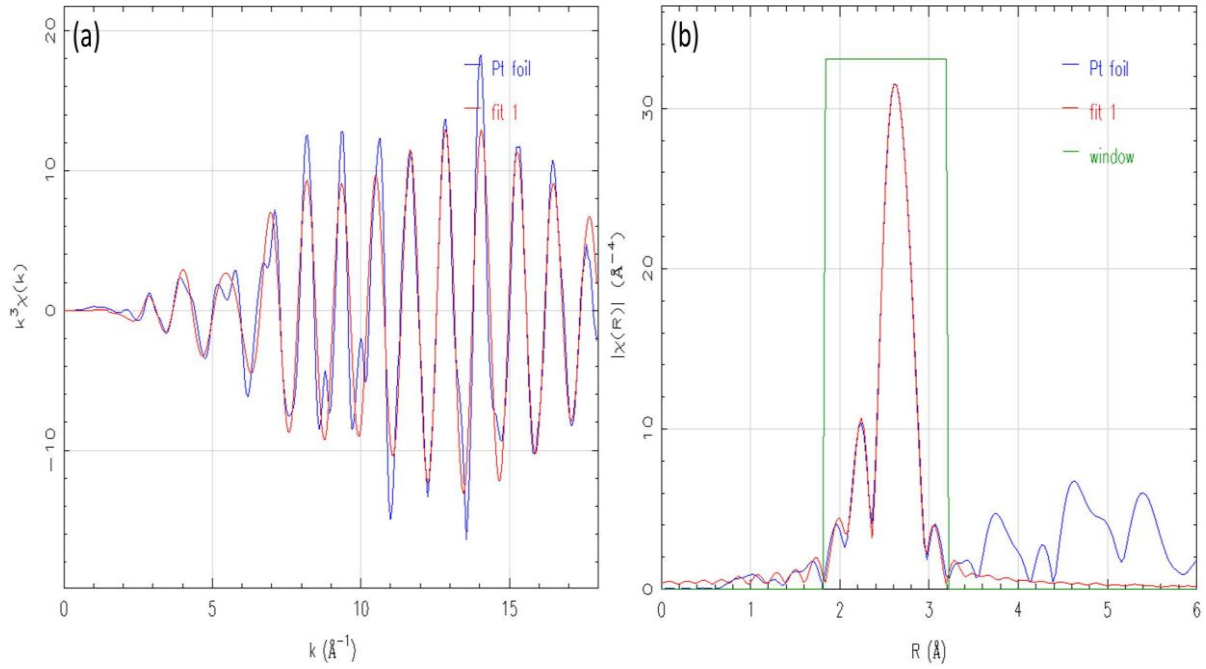

Figure A8: k^3-weighted EXAFS data of a Pt foil together with a 1st shell fit (a) in k-space (the fit was back Fourier transformed) and (b) the corresponding Fourier transform magnitude in R-space together with a window marking the fit region

The visual impression attests a good fit. Fit values and uncertainties are also reasonable:

- $S_0^2 = 0.86 \pm 0.04$ (should be between 0.7 and 1.0)
- ΔE_0 [eV] = 8.26 ± 0.52 (should be <10)
- ΔR [Å] = -0.007 ± 0.001 (this is a deviation at the third decimal point!)
- σ^2 [10^3 Å²] = 5.1 ± 0.1 (reasonable value for heavy 1st shell atoms)

Besides a visual impression and fit values plus uncertainties ARTEMIS also returns statistical goodness-of-fit parameters, parameters one can judge the feasibility of a fit by - the two most

important ones being the R-factor and the reduced chi-square parameter χ_v^2. The former gives the mean-square misfit, the squared difference between each fit and data point weighted by the sum of the squared data points and summed up over the whole data range [90]:

$$R = \sum_{i=1}^{N_{pts}} \frac{[Im(\chi_{dat}(R_i) - \chi_{th}(R_i))]^2 + [Re(\chi_{dat}(R_i) - \chi_{th}(R_i))]^2}{[Im(\chi_{dat}(R_i))]^2 + [Re(\chi_{dat}(R_i))]^2}$$

An R-value < 0.05 marks a good fit. For higher values the fit should be re-examined. The χ_v^2 parameter on the other hand can be used for comparisons between structural models with a different number of fit parameters used for fitting the same data set [90]:

$$\chi_v^2 = \frac{\chi^2}{v} = \frac{\chi^2}{N_{idp} - N_{var}}$$

With

$$\chi^2 = \frac{N_{idp}}{N_{pts} \cdot \varepsilon^2} \sum_{i=1}^{N_{pts}} [Re(\chi_{data}(R_i) - \chi_{th}(R_i))]^2 + [Im(\chi_{data}(R_i) - \chi_{th}(R_i))]^2$$

v	degree of freedom
N_{idp}	number of independent points in the measurement
N_{var}	number of variables in a fit
N_{pts}	number of data points in fit range
ε^2	uncertainties
Re/Im	real/imaginary part of EXAFS data
χ_{data}/χ_{th}	experimental/theoretical EXAFS data

χ^2 should be 1 for a good fit. For a discussion why that is never the case for a real life experiment see *e.g.* [30]. The reduced chi-square parameter is used instead to help choosing between structural models that seem similarly reasonable. The model whose χ_v^2 parameter is statistically significant smaller is more reasonable - “statistically significant” meaning that the χ_v^2 parameter should decrease by a factor of $1 + 2\sqrt{2/v}$ [90].

A.2 Ta/Nb LIII edge whiteline fit results

To determine their whiteline splittings and peak intensity ratios Ta and Nb LIII edge whitelines were fitted with MATHEMATICA using one arctan function and either two Lorentzian (Ta) or Gaussian functions (Nb). All functions were constrained to the same width. The 4TiO2 spectrum was fitted first and the fit value of the peak widths used fixed for all subsequent fits. Figure A9a-e and Table A1 as well as Figure A10a-e and Table A2 summarize the fit results.

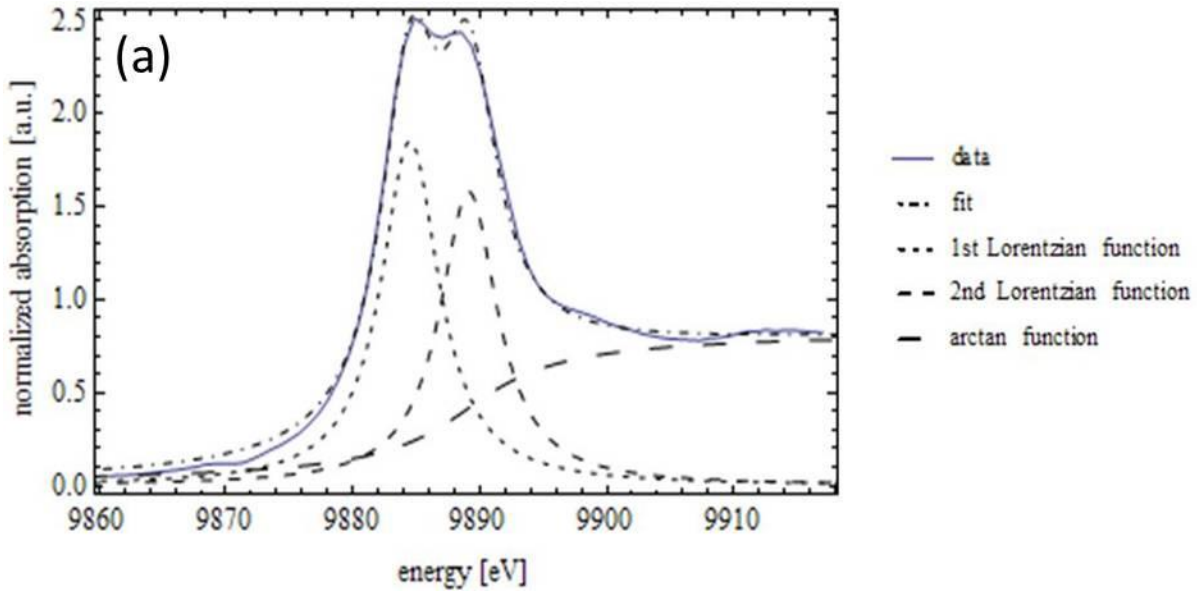

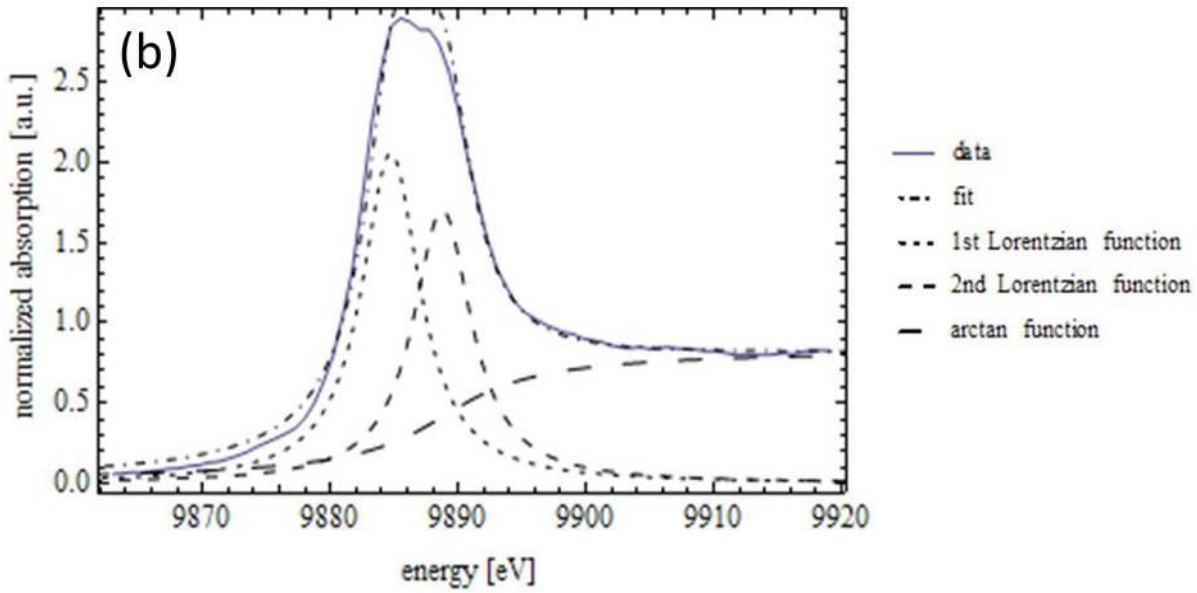

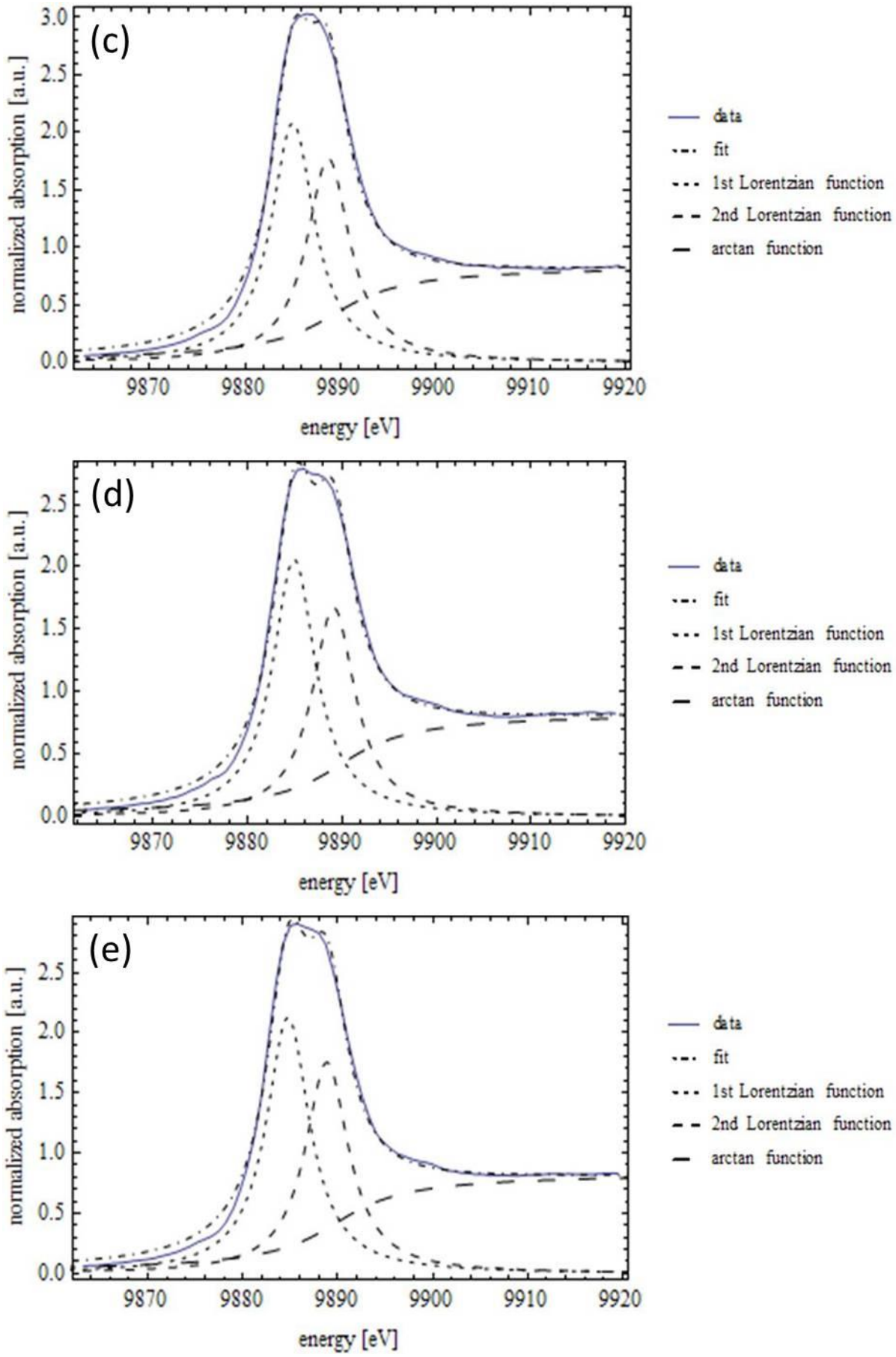

Figure A9: MATHEMATICA fit of the Ta LIII edge whitelines of (a) 4TiO2, (b) 4TiO2+KB, (c) 4TiO2+KB2, (d) 4TiO2+Pt, (e) 4TiO2+TKKE

Table A1: MATHEMATICA fit results of the Ta LIII edge whitelines

parameter / sample	4TiO2	4TiO2+KB	4TiO2+KB2	4TiO2+Pt	4TiO2+TKKE
arctan function amplitude	0.84 ± 0.01	0.85 ± 0.01	0.85 ± 0.01	0.84 ± 0.01	0.84 ± 0.01
arctan function width [eV]	5.6	5.6	5.6	5.6	5.6
arctan function position [eV]	9889.1 ± 1.4	9888.9 ± 1.7	9889.5 ± 1.6	9889.8 ± 1.4	9889.9 ± 1.5
1. Lorentzian function amplitude	16.2 ± 0.4	17.9 ± 0.6	18.1 ± 0.6	17.9 ± 0.5	18.5 ± 0.5
1. Lorentzian function width [eV]	5.6	5.6	5.6	5.6	5.6
1. Lorentzian function position [eV]	9884.5 ± 0.1	9884.7 ± 0.1	9885.0 ± 0.1	9884.9 ± 0.1	9884.8 ± 0.1
2. Lorentzian function amplitude	13.8 ± 0.6	14.9 ± 0.8	15.4 ± 0.8	14.6 ± 0.7	15.3 ± 0.7
2. Lorentzian function width [eV]	5.6	5.6	5.6	5.6	5.6
2. Lorentzian function position [eV]	9889.1 ± 0.1	9888.7 ± 0.1	9888.8 ± 0.1	9889.1 ± 0.1	9888.9 ± 0.1
1./2. Lorentzian function Δposition [eV]	4.6 ± 0.1	4.0 ± 0.1	3.7 ± 0.1	4.2 ± 0.1	4.1 ± 0.1
1./2. Lorentzian function amplitude ratio	1.2 ± 0.1	1.2 ± 0.1	1.2 ± 0.1	1.2 ± 0.1	1.2 ± 0.1

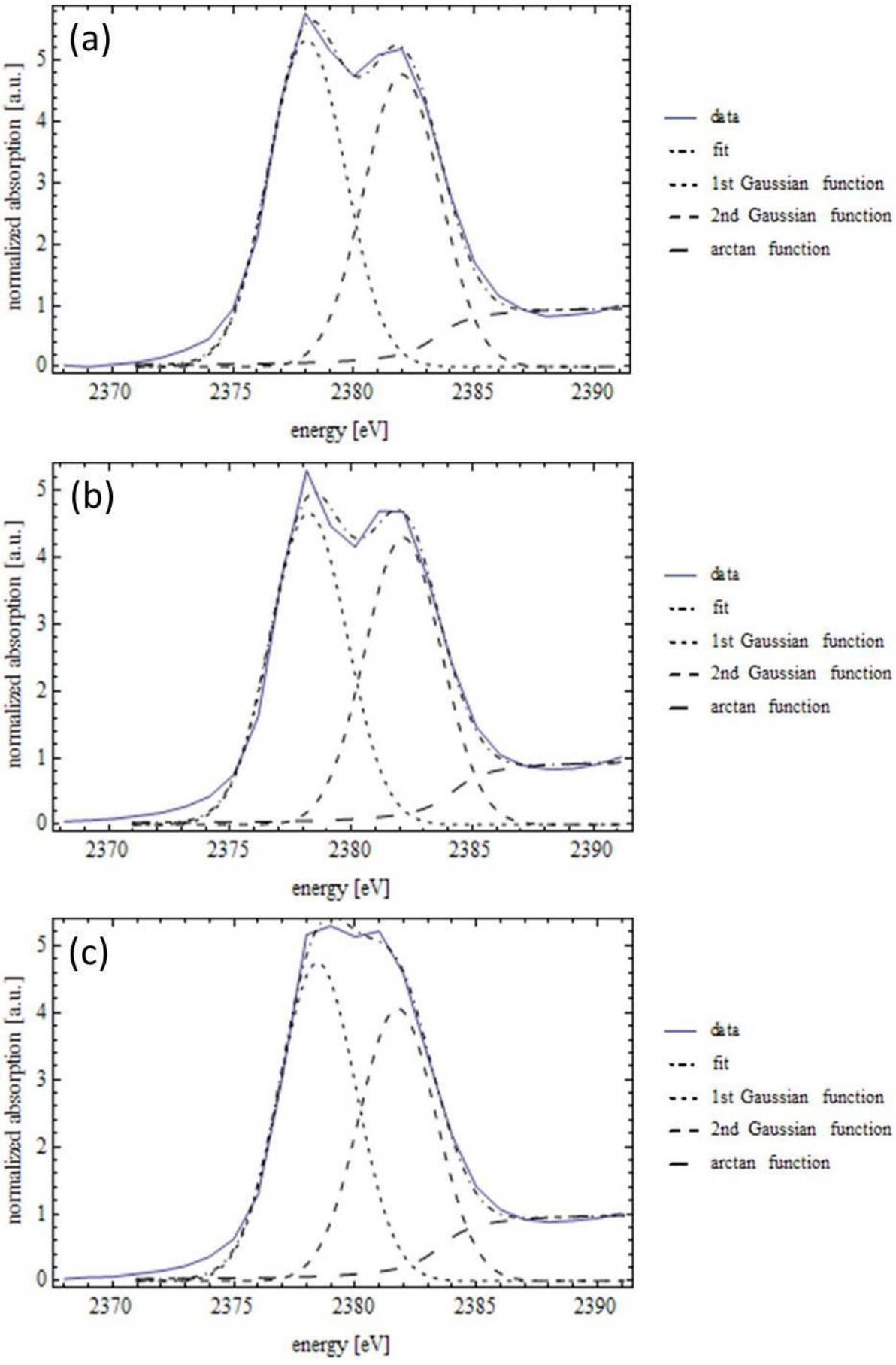
(a)
normalized absorption [a.u.]
energy [eV]
data
fit
1st Gaussian function
2nd Gaussian function
arctan function
(b)
normalized absorption [a.u.]
energy [eV]
data
fit
1st Gaussian function
2nd Gaussian function
arctan function
(c)
normalized absorption [a.u.]
energy [eV]
data
fit
1st Gaussian function
2nd Gaussian function
arctan function

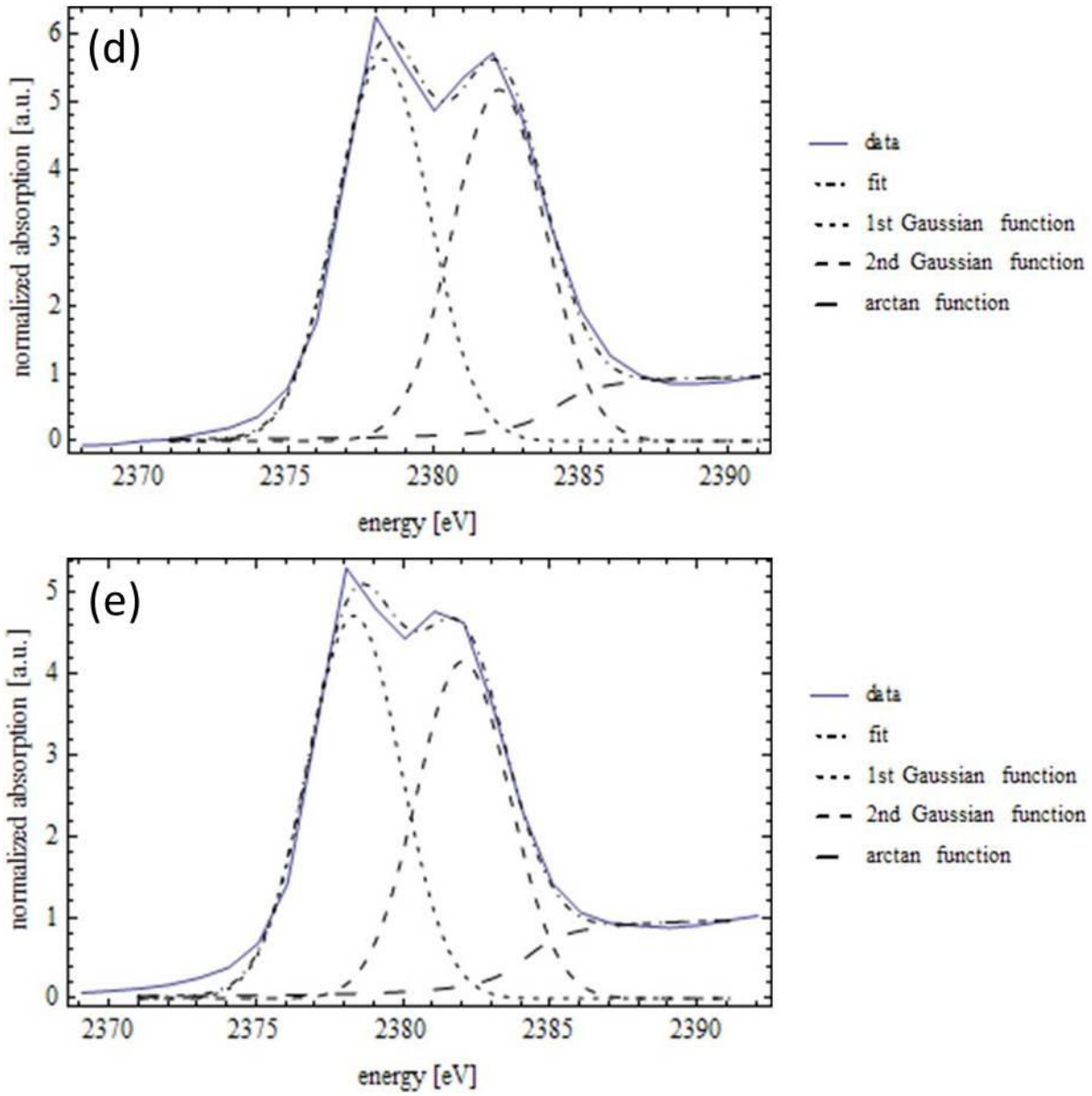

Figure A10: MATHEMATICA fit of the Nb LIII edge whitelines of (a) 4TiO2, (b) 4TiO2+KB, (c) 4TiO2+KB2, (d) 4TiO2+Pt, (e) 4TiO2+TKKE

Table A2: MATHEMATICA fit results of the Nb LIII edge whitelines

parameter / sample	**4TiO2**	**4TiO2+KB**	**4TiO2+KB2**	**4TiO2+Pt**	**4TiO2+TKKE**
arctan function amplitude	1.0 ± 0.1	1.0 ± 0.1	1.0 ± 0.1	1.0 ± 0.1	1.0 ± 0.1
arctan function width [eV]	1.1	1.1	1.1	1.1	1.1
arctan function position [eV]	2383.5 ± 1.7	2384.2 ± 1.3	2383.5 ± 1.5	2384.1 ± 1.4	2384.2 ± 1.1
1. Gaussian function amplitude	15.0 ± 0.3	13.1 ± 0.4	13.3 ± 0.6	15.7 ± 0.4	13.2 ± 0.4
1. Gaussian function width [eV]	1.1	1.1	1.1	1.1	1.1
1. Gaussian function position [eV]	2378.1 ± 0.1	2378.3 ± 0.1	2378.5 ± 0.1	2378.3 ± 0.1	2378.3 ± 0.1
2. Gaussian function amplitude	13.4 ± 0.7	12.0 ± 0.5	11.4 ± 0.5	14.5 ± 0.6	11.7 ± 0.4
2. Gaussian function width [eV]	1.1	1.1	1.1	1.1	1.1
2. Gaussian function position [eV]	2382.0 ± 0.1	2382.1 ± 0.1	2381.8 ± 0.2	2382.2 ± 0.1	2382.1 ± 0.1
1./2. Gaussian function Δposition [eV]	3.9 ± 0.2	3.9 ± 0.2	3.3 ± 0.2	4.0 ± 0.1	3.7 ± 0.2
1./2. Gaussian function amplitude ratio	1.1 ± 0.1	1.1 ± 0.1	1.2 ± 0.1	1.1 ± 0.1	1.1 ± 0.1

Additional remarks

Peak widths in every spectroscopy technique have two contributions: extrinsic (experimental) and intrinsic (sample-related) ones [91]. For XAFS the former are the energy resolution of the beamline [24] and the latter the core hole life time [91]. Experimental and sample-related peak broadening can be best fitted using Gaussian and Lorentzian functions, respectively. Ideally, a convolution of both, the so-called Voigt function, is used [92]. Since implementing these using MATHEMATICA was not successful a Pseudo-Voigt function was tested instead at the Ta and Nb LIII edge which is a linear combination of Gaussian and Lorentzian functions. Yet, using Lorentzian (Ta LIII) and Gaussian functions (Nb LIII edge) returned better results. Peak widths at the Ta LIII edge were 5.55eV which is bigger than the natural line width (4.88eV, [93]). The difference is considered experimental broadening. Peak widths at the Nb LIII edge on the other hand were 1.12eV which is smaller than the natural line width (1.66eV, [93])! Since this parameter was not interpreted but used for fitting only its actual value is secondary to its consistent use in all fits. All fit functions were used in a unit-normalized form meaning that their amplitudes correspond to the areas under the respective graph.

A.3 Nb K edge pre-edge feature fit results

To determine their intensities Nb K edge pre-edge features were fitted with MATHEMATICA using two Lorentzian and one arctan function. All functions were constrained to the same width. The 4TiO2 spectrum was fitted first and the arctan amplitude as well as the width of all functions used fixed for all subsequent fits. Figure A11a-e and Table A3 summarize the fit results.

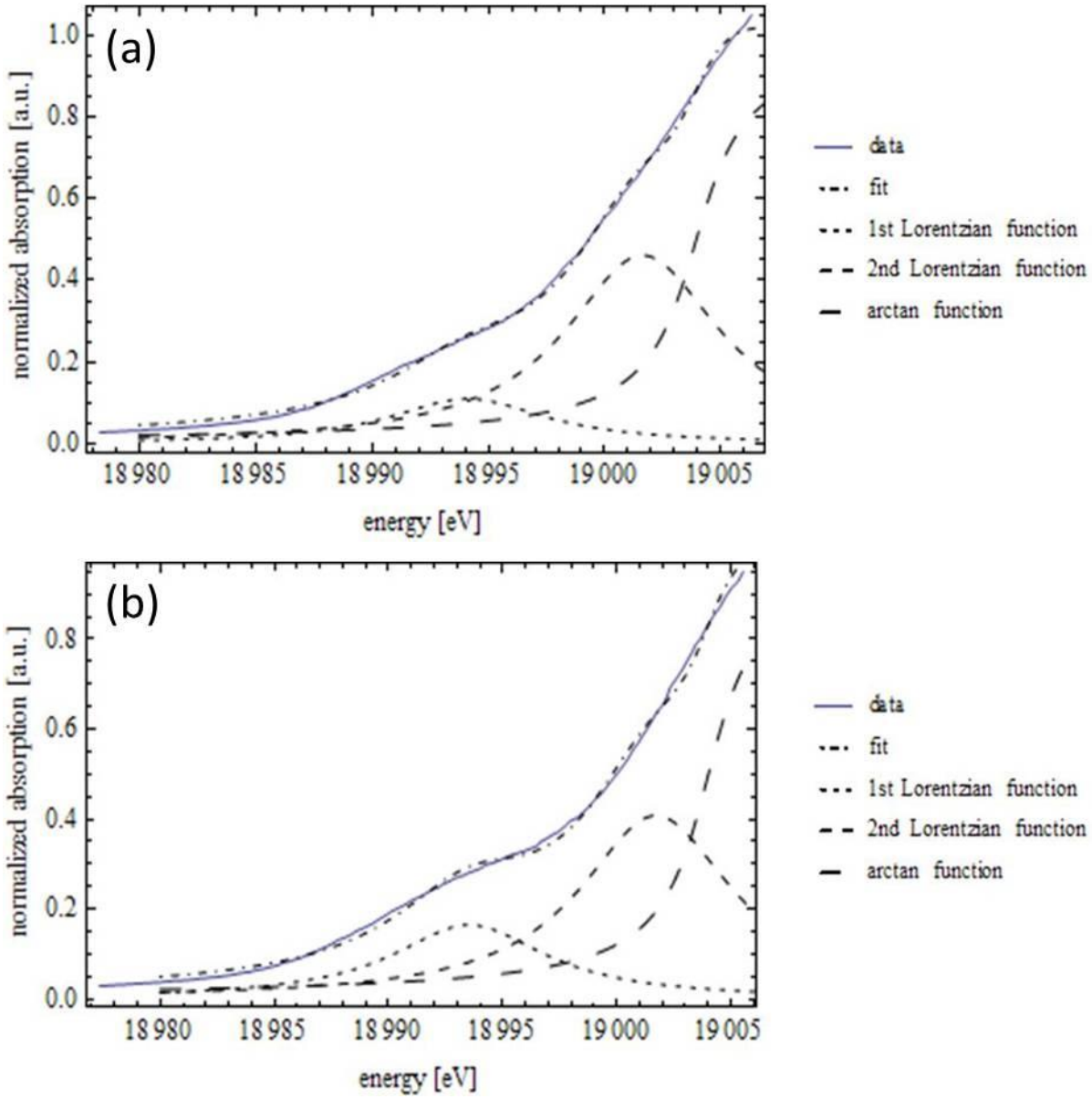

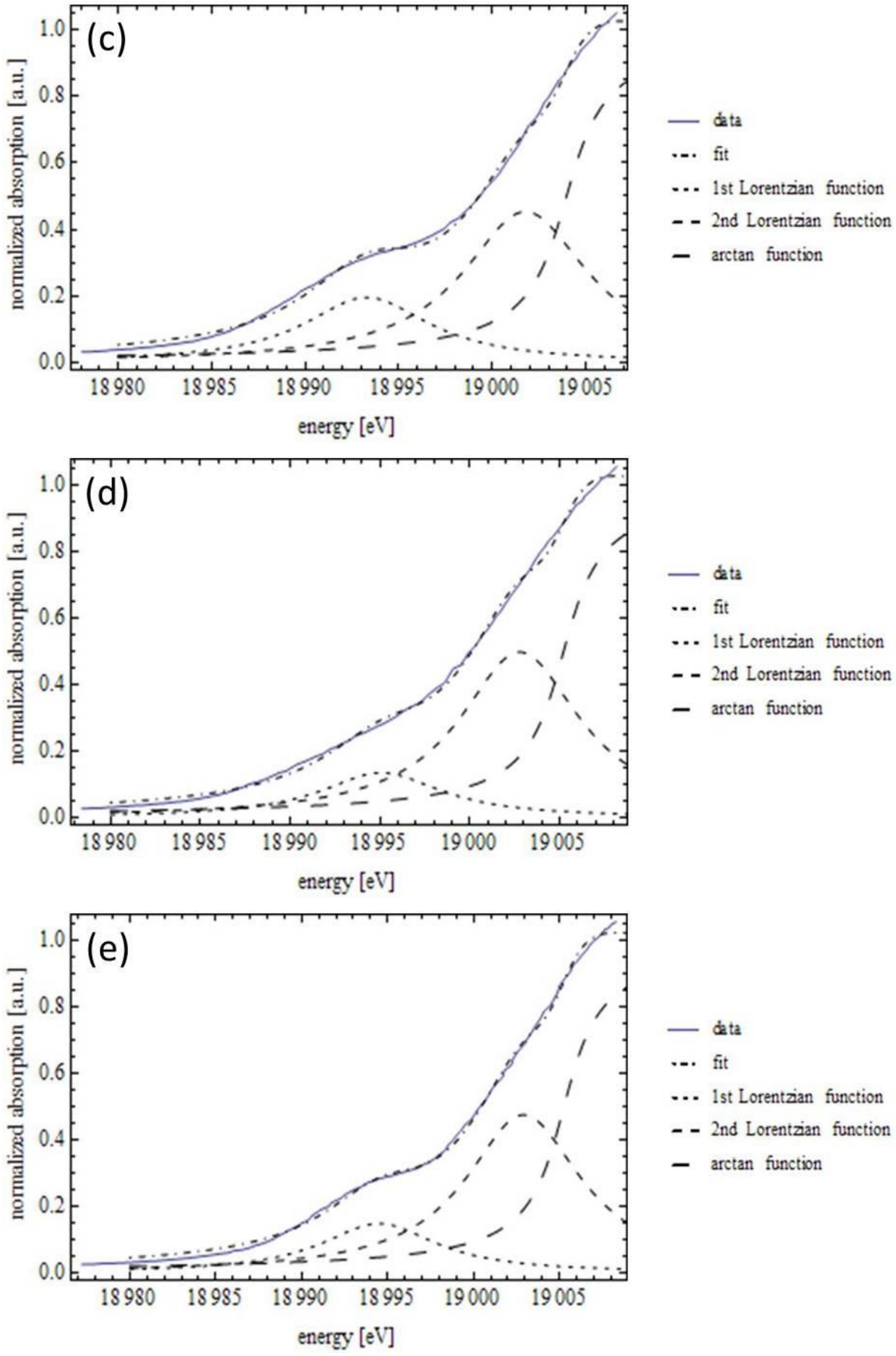

Figure A11: MATHEMATICA fit of the Nb K edge pre-edge features of (a) 4TiO2, (b) 4TiO2+KB, (c) 4TiO2+KB2, (d) 4TiO2+Pt, (e) 4TiO2+TKKE

Table A3: MATHEMATICA fit results of the Nb K edge pre-edge features

parameter / value	4TiO2	4TiO2+KB	4TiO2+KB2	4TiO2+Pt	4TiO2+TKKE
arctan function amplitude	1.0	1.0	1.0	1.0	1.0
arctan function width [eV]	1.6	1.6	1.6	1.6	1.6
arctan function position [eV]	19003.9 ± 0.1	19004.0 ± 0.1	19003.9 ± 0.1	19005.2 ± 0.1	19005.2 ± 0.1
1. Lorentzian function amplitude	1.4 ± 0.1	2.1 ± 0.1	2.5 ± 0.1	1.7 ± 0.1	1.9 ± 0.1
1. Lorentzian function width [eV]	8.2	8.2	8.2	8.2	8.2
1. Lorentzian function position [eV]	18994.1 ± 0.2	18993.5 ± 0.1	18993.3 ± 0.1	18995.1 ± 0.2	18994.5 ± 0.1
2. Lorentzian function amplitude	5.9 ± 0.1	5.3 ± 0.1	5.8 ± 0.1	6.4 ± 0.1	6.1 ± 0.1
2. Lorentzian function width [eV]	8.2	8.2	8.2	8.2	8.2
2. Lorentzian function position [eV]	19001.6 ± 0.1	19001.7 ± 0.1	19001.8 ± 0.1	19002.8 ± 0.1	19002.9 ± 0.1

Additional remarks

The primary goal was to fit the pre-edge features in order to determine their peak areas. Other fit parameters were not interpreted. This means that peak widths of Lorentzian and the arctan function were chosen differently since this approach returned better results. All fit functions were used in a unit-normalized form meaning that their amplitudes correspond to the areas under the respective graph.

A.4 Nb K edge EXAFS fit results

This chapter contains the complete fit results of which one or several were chosen in the results section as being most reasonable due to the lowest σ^2 values and residuals. Figure A12-16 and Tables A4-8 summarize these fit results.

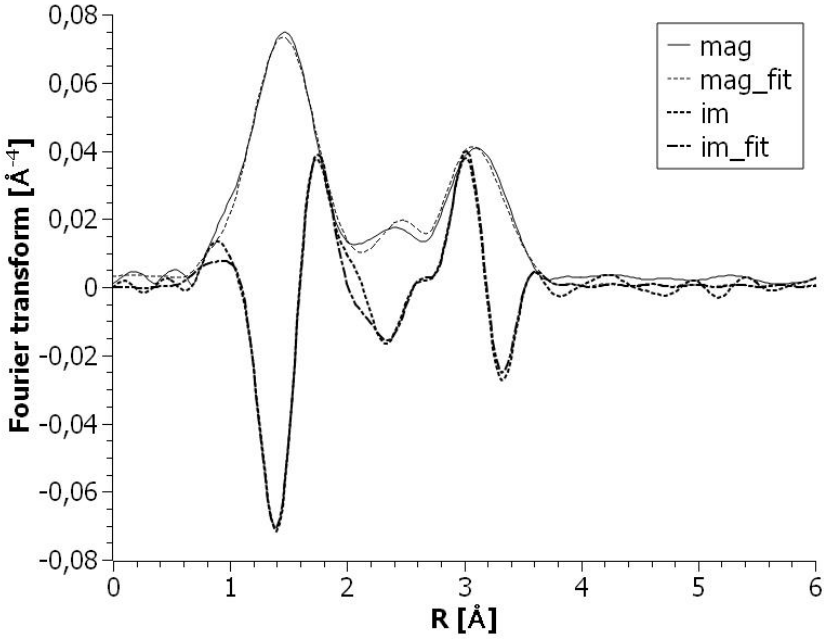

Figure A12: k^3-weighted Nb K edge EXAFS Fourier transform magnitude ("mag") and imaginary part ("im") of the sample 4TiO2 plus fit (model: scattering iii), not phase-corrected

Additional remark

The rutile structure was used as a structural model to fit all these five data sets. However, TiO_2 turned out to be predominantly present as anatase in the samples 4TiO2+KB and 4TiO2+KB2. Their fit values thus appear in the Appendix only. Nonetheless, because fits are reasonable I hypothesize that the actual geometric structure around Nb atoms in these two samples closely resembles the fitted ones.

Table A4: Nb K edge EXAFS fit results of 4TiO2 (the scattering and cluster model are described in chapter 4.1.5, “ii/iii/iv” represent the models used to resolve the O shell splitting as described in the same chapter. “f” refers to a parameter kept fixed during a fit to its respective crystallographic value, N = number of next neighbours, R = distance from absorber atom to the respective shell, σ2 = mean-square displacement of the bond length between the absorber atom and the atoms in a shell.)

model	**path 1**			**path 2**			**path 3**			**residual**
	N	R [Å]	σ^2 [Å²]	N	R [Å]	σ^2 [Å²]	N	R [Å]	σ^2 [Å²]	
scattering i	6.0	2.00	0.0085	2.0	3.02	0.0103	6.0	3.62	0.0079	10.4
scattering ii	2^f 4^f	2.10 1.97	0.0037 0.0037	2^f	3.02	0.0109	8^f	3.64	0.0103	6.9
scattering iii	3^f 3^f	2.08 1.94	0.0016 0.0016	2^f	3.02	0.0109	8^f	3.63	0.0103	6.6
scattering iv	4^f 2^f	1.97 2.10	0.0037 0.0037	2^f	3.02	0.0109	8^f	3.64	0.0103	6.9
cluster i	6.0	2.00	0.0076	2.0	2.83	0.0096	8.0	3.43	0.0116	14.2
cluster ii	2^f 4^f	2.10 1.97	0.0038 0.0038	2^f	2.84	0.0097	8^f	3.43	0.0116	13.2
cluster iii	3^f 3^f	1.94 2.08	0.0007 0.0007	2^f	2.85	0.0088	8^f	3.43	0.0115	12.1
cluster iv	4^f 2^f	1.97 2.10	0.0038 0.0038	2^f	2.84	0.0097	8^f	3.43	0.0116	13.1

path 1: Nb-O for scattering/cluster model

paths 2/3: Nb-Ti/Nb-Nb in case of scattering model/cluster model

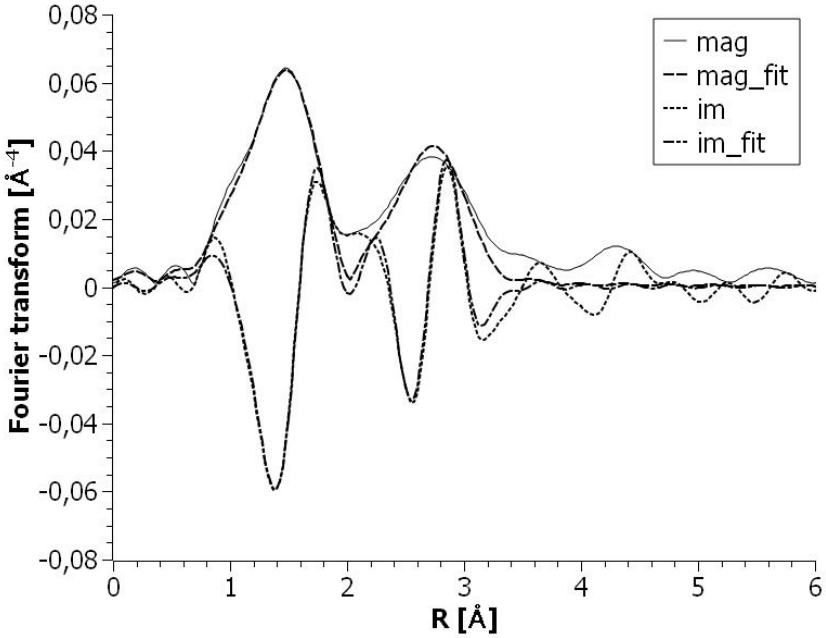

Figure A13: k^3-weighted Nb K edge EXAFS Fourier transform magnitude ("mag") and imaginary part ("im") of the sample 4TiO2+KB plus fit (model: scattering ii), not phase-corrected

Table A5: Nb K edge EXAFS fit results of 4TiO2+KB (explanations of the fit parameters can be found in the caption of Table A4)

model	**path 1**			**path 2**			**path 3**			**residual**
	N	R [Å]	σ^2 [Å²]	N	R [Å]	σ^2 [Å²]	N	R [Å]	σ^2 [Å²]	
scattering i	6.0	1.95	0.0093	2.0	2.61	0.0137	7.6	3.48	0.0121	17.3
scattering ii	2^f 4^f	1.84 1.99	0.0027 0.0027	2^f	3.10	0.0038	8^f	3.46	0.0190	10.6
scattering iii	3^f 3^f	1.91 2.05	0.0040 0.0040	2^f	3.13	0.0029	8^f	3.48	0.0243	11.5
scattering iv	4^f 2^f	1.95 2.06	0.0067 0.0067	2^f	3.13	0.0027	8^f	3.48	0.0252	12.5
cluster i	6.0	1.97	0.0093	2.0	2.89	0.0101	8.0	3.31	0.0154	11.4
cluster ii	2^f 4^f	1.89 2.03	0.0026 0.0046	2^f	2.92	0.0064	8^f	3.72	0.0155	14.8
cluster iii	3^f 3^f	1.92 2.05	0.0038 0.0034	2^f	2.92	0.0064	8^f	3.72	0.0155	14.8
cluster iv	4^f 2^f	1.94 2.07	0.0050 0.0023	2^f	2.92	0.0064	8^f	3.72	0.0155	14.8

path 1: Nb-O for scattering/cluster model
paths 2/3: Nb-Ti/Nb-Nb in case of scattering model/cluster model

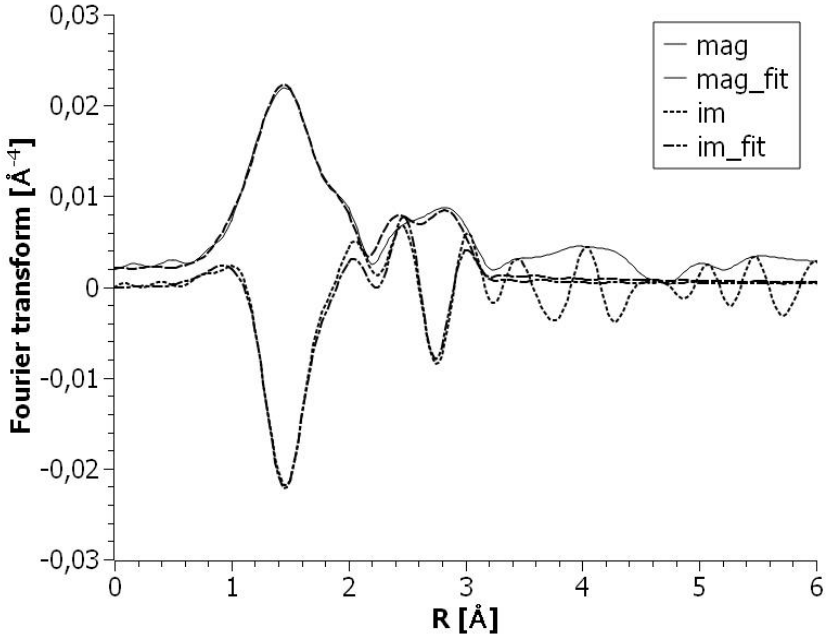

Figure A14: k^3-weighted Nb K edge EXAFS Fourier transform magnitude ("mag") and imaginary part ("im") of the sample 4TiO2+KB2 plus fit (model: cluster iv), not phase-corrected

Table A6: Nb K edge EXAFS fit results of 4TiO2+KB2 (explanations of the fit parameters can be found in the caption of Table A4)

model	**path 1**			**path 2**			**path 3**			**residual**
	N	R [Å]	σ^2 [Å²]	N	R [Å]	σ^2 [Å²]	N	R [Å]	σ^2 [Å²]	
scattering i	6.0	2.03	0.0222	0.6	3.19	0.0046	/	/	/	11.4
scattering ii	2^f 4^f	2.16 2.00	0.0173 0.0173	0.5	3.21	0.0047	/	/	/	8.1
scattering iii	3^f 3^f	1.96 2.13	0.0125 0.0125	0.6	3.21	0.0047	/	/	/	8.9
scattering iv	4^f 2^f	2.00 2.16	0.0173 0.0173	0.5	3.21	0.0047	/	/	/	8.1
cluster i	6.0	2.04	0.0215	1.1	3.01	0.0215	/	/	/	13.6
cluster ii	2^f 4^f	1.96 2.13	0.0097 0.0153	0.9	3.03	0.0101	/	/	/	7.9
cluster iii	3^f 3^f	1.98 2.16	0.0113 0.0124	0.9	3.02	0.0103	/	/	/	7.7
cluster iv	4^f 2^f	2.00 2.19	0.0133 0.0098	0.9	3.02	0.0107	/	/	/	7.5

path 1: Nb-O for scattering/cluster model
paths 2/3: Nb-Ti/Nb-Nb in case of scattering model/cluster model

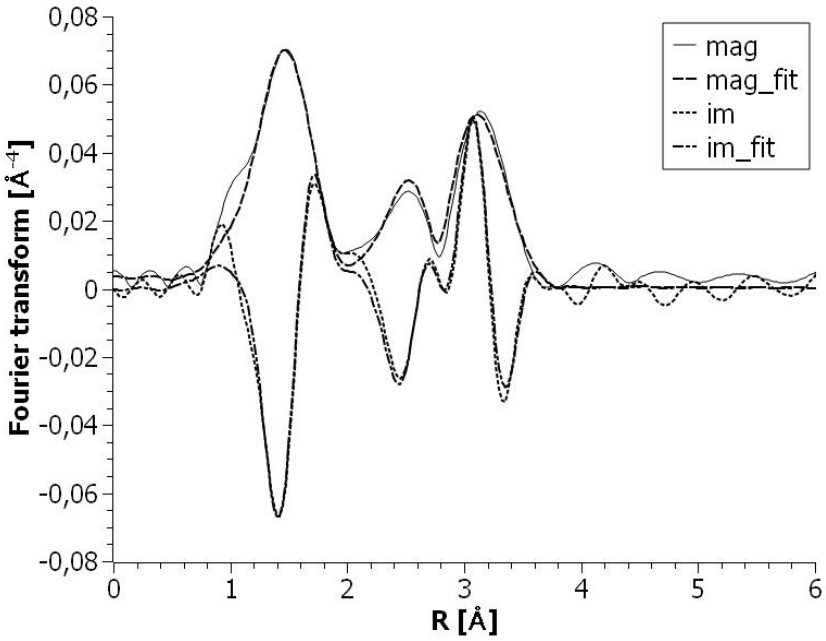

Figure A15: k^3-weighted Nb K edge EXAFS Fourier transform magnitude ("mag") and imaginary part ("im") of the sample 4TiO2+Pt plus fit (model: scattering ii), not phase-corrected

Table A7: Nb K edge EXAFS fit results of 4TiO2+Pt (explanations of the fit parameters can be found in the caption of Table A4)

model	**path 1**			**path 2**			**path 3**			**residual**
	N	R [Å]	σ^2 [Å²]	N	R [Å]	σ^2 [Å²]	N	R [Å]	σ^2 [Å²]	
scattering i	6.0	1.99	0.0088	1.8	3.05	0.0058	6.4	3.63	0.0074	10.8
scattering ii	2^f 4^f	2.09 1.96	0.0047 0.0047	2^f	3.05	0.0068	8^f	3.64	0.0090	9.8
scattering iii	3^f 3^f	2.05 1.93	0.0040 0.0040	2^f	3.05	0.0067	8^f	3.63	0.0090	11.1
scattering iv	4^f 2^f	1.96 2.09	0.0047 0.0047	2^f	3.05	0.0068	8^f	3.64	0.0090	9.8
cluster i	6.0	2.00	0.0088	2.0	2.88	0.0079	8.0	3.45	0.0112	18.6
cluster ii	2^f 4^f	2.12 1.98	0.0041 0.0041	2^f	2.89	0.0079	8^f	3.46	0.0111	15.5
cluster iii	3^f 3^f	2.08 1.94	0.0027 0.0027	2^f	2.88	0.0080	8^f	3.46	0.0111	16.4
cluster iv	4^f 2^f	1.98 2.12	0.0041 0.0041	2^f	2.89	0.0079	8^f	3.46	0.0111	15.5

path 1: Nb-O for scattering/cluster model
paths 2/3: Nb-Ti/Nb-Nb in case of scattering model/cluster model

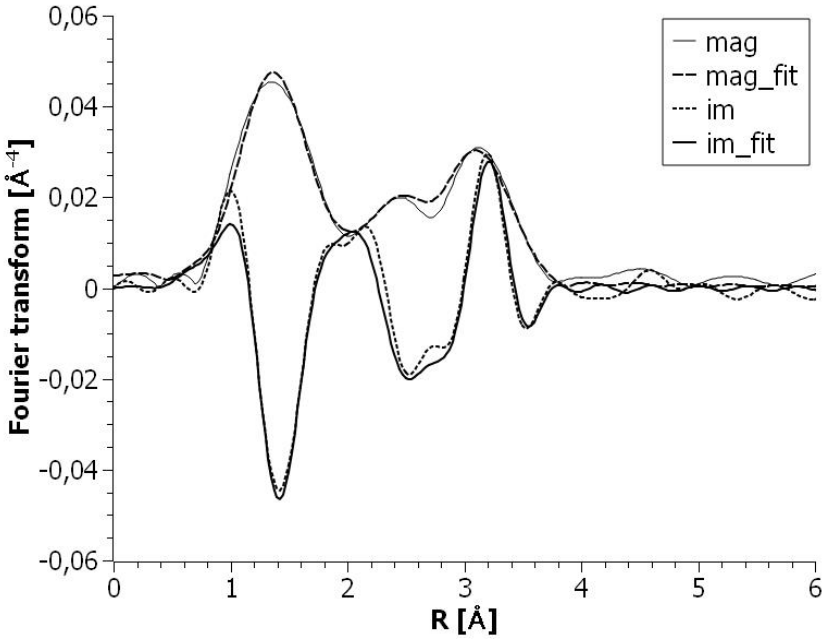

Figure A16: k^3-weighted Nb K edge EXAFS Fourier transform magnitude ("mag") and imaginary part ("im") of the sample 4TiO2+TKKE plus fit (model: scattering iv), not phase-corrected

Table A8: Nb K edge EXAFS fit results of 4TiO2+TKKE (explanations of the fit parameters can be found in the caption of Table A4)

model	**path 1**			**path 2**			**path 3**			**residual**
	N	R [Å]	σ^2 [Å²]	N	R [Å]	σ^2 [Å²]	N	R [Å]	σ^2 [Å²]	
scattering i	6.0	1.98	0.0123	0.9	3.03	0.0017	6.0	3.61	0.0092	12.0
scattering ii	2^f 4^f	2.12 1.95	0.0022 0.0049	2^f	3.05	0.0096	8^f	3.65	0.0122	8.9
scattering iii	3^f 3^f	2.09 1.93	0.0043 0.0030	2^f	3.05	0.0096	8^f	3.65	0.0122	8.7
scattering iv	4^f 2^f	2.07 1.91	0.0065 0.0015	2^f	3.05	0.0096	8^f	3.65	0.0122	8.6
cluster i	6.0	1.98	0.0121	2.0	2.84	0.0121	8.0	3.41	0.0131	17.9
cluster ii	2^f 4^f	1.89 2.06	0.0022 0.0047	2^f	2.86	0.0073	8^f	3.43	0.0125	16.0
cluster iii	3^f 3^f	1.91 2.08	0.0022 0.0017	2^f	2.86	0.0071	8^f	3.43	0.0124	13.3
cluster iv	4^f 2^f	1.94 2.10	0.0053 0.0022	2^f	2.86	0.0074	8^f	3.43	0.0126	15.0
path 1: Nb-O for scattering/cluster model paths 2/3: Nb-Ti/Nb-Nb in case of scattering model/cluster model										

Abstract

PEM fuel cells are an interesting energy source for mobile applications. Efforts to improve their weaknesses cost, performance, and durability include improving the catalysts' supports. Encouraging approaches are C-TiO_2 hybrid and core-shell supports whereas titanium dioxide is commonly doped to increase its electric conductivity.

In this thesis I studied the impact of Ta-/Nb- co-doping on a TiO_2 nano-support, C-TiO_2 hybrid/core-shell supports made by adding two kinds of carbon black and a Pt-TiO_2 catalyst-support unit. XANES results show that both dopants replaced Ti atoms and are statistically distributed in their respective TiO_2 host structure (which is either predominantly rutile or anatase). There is also evidence of interaction between these dopants and both the carbon supports as well as Pt catalyst, most likely via bridging oxygen atoms. EXAFS analysis reveals that Nb incorporation did distort the TiO_2 host structure of at least one sample to a greater extent compared to Ta incorporation. The core-shell support displays the highest degree of disorder and smallest particle size, which is most likely correlated.

Reduction/oxidation experiments show that Pt atoms in PtPd nano-catalysts supported on C-TiO_2 hybrid nano-supports have a low affinity for oxidation and are easily reduced.

Pulsed laser ablation in liquid (PLAL) has proven its usefulness as a nanoparticle (NP) synthesis method alternative to traditional chemical reduction methods.

Additive-free Pt NPs were synthesized by PLAL and their interaction characterized *in situ* with H_2O, a sodium phosphate buffer and sodium citrate as well as a TiO_2 support. XANES results indicate that the respective NP-solvent interaction varies in strength. The ions added *ex situ* diffuse through the particles' electric double layer and interact electrostatically with the Stern plane. Consequently, these ions weaken the interaction of the functional OH-groups which are bound to the partially oxidized platinum surfaces and cause their partial reduction. Comparing XANES/EXAFS spectra of laser-generated with wet-chemically synthesized Pt NPs indicate different types of Pt-O bonds: a Pt(IV)O_2-type in case of wet-chemical and a Pt(II)O-type in case of laser-generated NPs. A comparison of unsupported laser-generated platinum NPs in H_2O with TiO_2-supported ones shows no whiteline intensity differences and also an identical number of Pt-O bonds in both cases. This suggests that in the deposition process at least part of the double layer coating stays intact and that the ligand-free particle properties are preserved.

Acknowledgements

At this point I want to express my sincere gratitude to the following people:

First of all Prof. Dr. J. Hormes for accepting me as his PhD student thus having given me the opportunity for the great adventure that was Canada and to do lots of travel.

Prof. Dr. S. Linden for agreeing to be my co-supervisor.

The beamline scientists at HXMA (Ning Chen and Weifeng Chen) and IDEAS (Kim Tan and David Muir) for their support before, during and after beamtime. A special thanks to Ning for performing EXAFS fits. A very special thanks to Kim and David for their tireless efforts to get IDEAS running; without you guys I would have no measurements in sufficient quality to the present day.

Ru Igarashi and Tonia Batten for their hard work at IDEAS whenever it was necessary.

The engineering department for making the sample chamber and all in all everyone at the CLS that helped in any way making this thesis possible.

Christina Bock and Vladimir Neburchilov from the NRC for making samples and for providing information about them.
All the people I worked with at CENIDE, especially Galina Marzun, for making samples as well as (so it seemed at times) never-ending discussions about the results.

Ms. Martha W. Schaefer for reading through my thesis and correct my English (and Physics).

Last but not least I want to express my sincere gratitude to all the wonderful people I met in Saskatoon (in the first place all past and present members of my former soccer team NoRuls) and most of all Martin Niestroj for being a friend throughout the years - on and off the field.

Research described in this thesis was performed at the Canadian Light Source, which is supported by the Canada Foundation for Innovation, Natural Sciences and Engineering Research Council of Canada, the University of Saskatchewan, the Government of Saskatchewan, Western Economic Diversification Canada, the National Research Council Canada, and the Canadian Institutes of Health Research.

Reference list

[1] "There's plenty of room at the bottom"; Feynman, R. P.; talk he gave on December 29th 1959 at the annual meeting of the American Physical Society at the California Institute of Technology (Caltech); first published in Caltech Engineering and Science, 23 (1960), pp. 22–36

[2] "Quantitative visualization of colloidal and intracellular gold nanoparticles by confocal microscopy"; Klein, S.; Petersen, S.; Taylor, U.; Rath, D.; Barcikowski, S.; J. Biomed. Opt., 15 (2010), p. 036015

[3] "Synthesis and catalytic properties of metal nanoparticles: Size, shape, support, composition and oxidation state effects"; Cuenya, B. R.; Thin Solid Films, 518 (2010), pp. 3127–3150

[4] "The development of gas sensor for carbon monoxide monitoring using nanostructure of Nb-TiO2"; Anukunprasert, T.; Saiwan, C.; Traversa, E.; Science and Technology of Advanced Materials, 6 (2005), pp. 359–363

[5] „nano.DE-Report 2013: Status quo der Nanotechnologie in Deutschland"; Federal Ministry of Education and Research (BMBF), 2014

[6] "Nanoparticle Technology Handbook"; Hosokawa, M.; Nogi, K.; Naito, M.; Yokoyama, T.; Elsevier, 2nd edition, 2007

[7] "X-ray spectroscopy studies on the surface structural characteristics and electronic properties of platinum nanoparticles"; Bayindir, Z.; Duchesne, P. N. ; Cook, S. C.; MacDonald, M. A.; Zhang, P.; The Journal Of Chemical Physics, 131 (2009), pp. 244716-1–244716-7

[8] "Size- and support-dependency in the catalysis of gold"; Haruta, M.; Catalysis Today, 36 (1997), pp. 153–166

[9] "Electron–electron and electron-hole interactions in small semiconductor crystallites The size dependence of the lowest excited electronic state"; Brus, L. E.; J. Chem. Phys., 80 (1984), pp. 4403–4409

[10] "Support materials for PEMFC and DMFC electrocatalysts – A review"; Sharma, S.; Pollet, B. G.; Journal of Power Sources, 208 (2012), pp. 96–119

[11] "How Citrate Ligands Affect Nanoparticle Adsorption to Microparticle Supports"; Wagener, P; Schwenke, A.; Barcikowski, S.; Langmuir, 28 (2012), pp. 6132–6140

[12] "Relevance of Sol-Gel Methods for Synthesis of Fine Particles"; Schmidt, H.; KONA Powder and Particle, 14 (1996), pp. 92–103

[13] "The influence of various coatings on the electronic, magnetic and geometric properties of Cobalt – nanoparticles"; Hormes, J.; Modrow, H.; Boennemann, H.; Kumar, C.S.S.R.; J. Appl. Physics, 97 (2005), 10R102

[14] "Nanotechnology in a Nutshell: From Simple to Complex Systems"; Ngo, C.; van de Voorde, M.; Atlantis Press, 2014; "Making Nano-Objects"; chapter 2

[15] "Nanomaterials via Laser Ablation/Irradiation in Liquid: A Review"; Zeng, H; Du, Xi-Wen; Singh, S. C.; Kulinich, S. A.; Yang, S.; He, J.; Cai, W.; Adv. Funct. Mater., 22 (2012), pp. 1333–1353

[16] "What controls the composition and the structure of nanomaterials generated by laser ablation in liquid solution?"; Amendola, V; Meneghetti, M; Phys. Chem. Chem. Phys.; 15 (2013), pp. 3027–3046

[17] http://energy.gov/eere/fuelcells/types-fuel-cells (September 21, 2015)

[18] "Electrocatalytic Activity and Stability of Pt clusters on State-of-the-Art Supports: A Review"; Shrestha, S.; Liu, Y.; Mustain, W. E.; Catalysis Reviews: Science and Engineering, 53 (2011), pp. 256–336

[19] "Development of a Titanium Dioxide-Supported Platinum Catalyst with Ultrahigh Stability for Polymer Electrolyte Membrane Fuel Cell Applications"; Huang, S.-Y.; Ganesan, P.; Park, S.; Popov, B. N.; J. Am. Chem. Soc., 131 (2009), pp. 13898–13899

[20] "Carbon-Nb0.07Ti0.93O2 composite supported Pt-Pd electrocatalysts for PEM fuel cell oxygen reduction reaction"; Ignaszak, A.; Song, C.; Zhu, W.; Wang, Y.-J; Zhang, J.; Bauer, A.; Baker, R.; Neburchilov, V.; Ye, S.; Campbell, S.; Electrochimica Acta, 75 (2012), pp. 220–228

[21] https://www.akzonobel.com/polymeradditives/ (December 27, 2015)

[22] "Adsorption of Colloidal Platinum Nanoparticles to Supports Charge Transfer and Effects of Electrostatic and Steric Interactions"; Marzun, G.; Streich, C.; Jendrzej, S.; Barcikowski, S; Wagener, S.; Langmuir, 30 (2014), pp. 11928–11936

[23] "Size control and supporting of palladium nanoparticles made by laser ablation in saline solution as a facile route to heterogeneous catalysts"; Marzun, G.; Nakamura, J.; Zhang, X.; Barcikowski, S.; Wagener, P.; Applied Surface Science, 348 (2015), pp. 75–84

[24] "An Introduction to Synchrotron Radiation: Techniques and Applications"; Willmott, P.; John Wiley & Sons, 2011

[25] "The Physics of Atoms and Quanta: Introduction to Experiments and Theory"; Haken, H.; Wolf, H. C.; Springer, 7th edition, 2005

[26] "EXAFS: Basic Principles and Data Analysis"; Teo, B. K.; Springer Berlin Heidelberg, 1986

[27] "Fundamentals of XAFS"; Newville, M.; Consortium of Advanced Radiation Sources; University of Chicago; Revision 1.7, 2004

[28] "Methods of Soil Analysis. Part 5. Mineralogical Methods"; Ulery, A.L.; Drees, A.L. (editors); SSSA Book Series, no. 5; Soil Science Society of America; 2008; "Analysis of Soils and Minerals Using X-ray Absorption Spectroscopy"; Kelly, S.D.; Hesterberg, D.; Ravel; B.; chapter 14; pp. 387–464

[29] "XAFS spectroscopy; fundamental principles and data analysis"; Koningsberger, D.C.; Mojet, B.L.; van Dorssen, G.E.; Ramaker, D.E.; Topics in Catalysis, 10 (2000), pp. 143–155

[30] "Advanced Topics in EXAFS Analysis"; Ravel, B.; APS XAFS Summer School, 2008

[31] "Theory of the extended x-ray absorption fine structure"; Lee, P. A.; Pendry, J. B.; Phys. Rev. B, 11 (1975), pp. 2795–2811

[32] http://www.camd.lsu.edu/beamlines.htm (September 21, 2015)

[33] http://www.xia.com/Differential_Pump.html (December 4, 2015)

[34] "High Vacuum Two Crystal Soft X-ray Monochromator"; Lemonnier, M.; Collet, O.; Depautex, C.; Esteva, J.-M.; Raoux, D.; Nuclear Instruments and Methods, 152 (1978), pp. 109–111

[35] "Absorptionsspektroskopie an Atomen und kleinen Molekülen im weichen Röntgengebiet"; Chauvistre, R.; diploma thesis, Bonn University (Germany), 1987

[36] "Preparation of XAFS samples"; Bunker, G.; talk; Illinois Institute of Technology http://gbxafs.iit.edu/training/XAFS_sample_prep.pdf (September 21, 2015)

[37] "Microwave assisted polyol method for the preparation of PtC, Ru/C and PtRu/C nanoparticles and its application in electrooxidation of methanol"; Harish, S.; Baranton, S.; Coutanceau, C.; Joseph, J.; J. Pow. Sources, 214 (2012), pp. 33–39

[38] "Ta and Nb co-doped TiO2 and its carbon-hybrid materials for supporting Pt–Pd alloy electrocatalysts for PEM fuel cell oxygen reduction reaction"; Wang, Y.-J.; Wilkinson, D. P.; Neburchilov, V.; Song, C.; Guest, A.; Zhang; J.; J. Mater. Chem. A, 2 (2014), pp. 12681–12685

[39] http://www.sachtleben.de/fileadmin/pdf_dateien/titandioxid/HOMBIKAT_TYPE_II.pdf (September 21, 2015)

[40] "Size-Selected Synthesis of PtRu Nano-Catalysts: Reaction and Size Control Mechanism"; Bock, C.; Paquet, C.; Couillard, M.; Botton, G. A.; MacDougall, B. R.; J. Am. Chem. Soc., 126 (2004), pp. 8028–8037

[41] "The In-Situ Investigation of High Temperature Reactions of Cobalt and Cobalt Containing Micro and Nanoparticles by X-ray Absorption Near Edge Structure Spectroscopy"; Liu, D.; diploma thesis, Bonn University (Germany), 2009

[42] "Monitoring of Pt Nanoparticle Formation by H2 Reduction of PtO2: An in Situ Dispersive X-ray Absorption Spectroscopy Study"; Bernardi, F.; Alves, M. C. M.; Morais, J.; J. Phys. Chem. C, 114 (2010), pp. 21434–21438

[43] "On highly active partially oxidized platinum in carbon monoxide oxidation over supported platinum catalysts"; Alayon, E.M.C.; Singh, J.; Nachtegaal, M.; Harfouche, M.; van Bokhoven, J.A.; Journal of Catalysis, 263 (2009), pp. 228–238

[44] "Data processing with IFEFFIT, ATHENA & ARTEMIS"; Newville, M.; Consortium for Advanced Radiation Sources, University of Chicago; July 24, 2007

[45] "ATHENA, ARTEMIS, HEPHAESTUS: data analysis for x-ray absorption spectroscopy using IFEFFIT"; Ravel, B.; Newville, M; J. Synchrotron Rad., 12 (2005), pp. 537–541

[46] "X-ray data booklet"; Thompson, A. C. (editor); Center for X-ray Optics and Advanced Light Source; 3rd edition, 2009

[47] WinXAS manual; Ressler, T.; version 3.2, 2009

[48] www.crystallography.net/ (September 21, 2015)

[49] http://cars9.uchicago.edu/~newville/adb/search.html (September 21, 2015)

[50] http://www.webelements.com/ (December 17, 2015)

[51] "X K Edge Absorption of Titanium and L Edges of Tantalum in (Ti, Ta)O, Rutile Solid Solutions"; Poumellec, B.; Marucco, J. F.; Touzelin, B.; phys. stat. sol. (b), 137 (1986), pp. 519–531

[52] "Novel magnetic nanoparticles: size and surfactant effects on geometric and electronic structure, probed using X-ray Absorption Spectroscopy"; Palina, N.; doctorate thesis, Bonn University (Germany), 2005

[53] "Physik fuer Ingenieure"; Hering, E.; Martin, R.; Stohrer, M.; VDI, 5th edition, 1995

[54] "Photoemission and STM study of the electronic structure of Nb-doped TiO2"; Morris, D.; Dou, Y.; Rebane, J. ; Mitchell, C. E. J.; Egdell, R. G.; Law, D. S. L.; Vittadini, A.; Casarin, M.; Physical Review B, 61 (2000), pp. 13445–13457

[55] "Niobium-Doped Titania Nanoparticles: Synthesis and Assembly into Mesoporous Films and Electrical Conductivity"; Liu, Y.; Szeifert, J. M.; Feckl, J. M.; Mandlmeier, B.; Rathousky, J.; Hayden, O.; Fattakhova-Rohlfing, D.; Bein, T.; ACS Nano, 4 (2010), pp. 5373–5381

[56] "Improved-Performance Dye-Sensitized Solar Cells using Nb-doped TiO2 Electrodes: Efficient Electron Injection and Transfer"; Lue, X.; Mou, X.; Wu, J.; Zhang, D.; Zhang, L.; Huang, F.; Xu, F.; Huang, S.; Adv. Funct. Mater., 20 (2010), pp. 509–515

[57] "Insights into the structural and chemical modifications of Nb additive on TiO2 nanoparticles"; Ruiz, A. M.; Dezanneau, G.; Arbiol, J.; Cornet, V.; Morante, Joan R.; Chem. Mater., 16 (2004), pp. 862–871

[58] http://ruby.colorado.edu/~smyth/min/tio2.html

[59] "X-Ray Absorption K-Edge Spectra of Titanium in (Ti, Nb)O2 Rutile Solid Solutions"; Poumellec, B.; Lagnel, F.; Marucco, J. F.; Touzelin, B.; phys. stat. sol. (b), 133 (1986), pp. 371–377

[60] "Assignment of pre-edge peaks in K-edge x-ray absorption spectra of 3d transition metal compounds electric dipole or quadrupole"; Yamamoto, T; X-Ray Spectrom., 37 (2008), pp. 572–584

[61] "Determination of Ti coordination from pre-edge peaks in Ti K-edge XANES"; Jiang, B.; Su, D.; Spence, J. C. H.; Physical Review B, 76 (2007), pp. 214117-1–214117-9

[62] "Ti K-edge XANES studies of Ti coordination and disorder in oxide compounds: Comparison between theory and experiment"; Farges, F.; Brown Jr., G. E.; Rehr, J. J.; Physical Review B, 56 (1997), pp. 1809–1819

[63] "Structural determination of titanium-oxide nanoparticles by x-ray absorption spectroscopy"; Wu, Z. Y.; Zhang, J.; Ibrahim, K.; Xian, D. C.; Li, G.; Tao, Y.; Hu, T. D.; Bellucci, S.; Marcelli, A.; Zhang, Q. H.; Gao, L.; Chen, Z. Z.; Appl. Phys. Lett., 80 (2002), pp. 2973–2975

[64] "Structural and Electronic Properties of Sol-Gel Titanium Oxides Studied by X-ray Absorption Spectroscopy"; Luca, V.; Djajanti, S.; Howe, R. F.; J. Phys. Chem. B, 102 (1998), pp. 10650–10657

[65] "Anatase-TiO2 Nanomaterials: Morphological/Size Dependence of the Crystallization and Phase Behavior Phenomena"; Fernandez-Garcıa, M.; Wang, X.; Belver, C.; Hanson, J. C.; Rodriguez, J. A.; J. Phys. Chem. C, 111 (2007), pp. 674–682

[66] "Redox and speciation of tin in hydrous silicate glasses a comparison with Nb, Ta, Mo and W"; Farges, F.; Linnen, R. L.; Brown, Jr., G. E.; The Canadian Mineralogist, 44 (2006), pp. 795–810

[67] "X-ray absorption spectroscopy investigation of structurally modified lithium niobate crystals"; Vitova, T.; doctorate thesis, Bonn University (Germany), 2008

[68] "Redox Chemistry of Tantalum Clusters on Silica Characterized by X-ray Absorption Spectroscopy"; Nemana, S.; Gates, B. C.; J. Phys. Chem. B, 110 (2006), pp. 17546–17553

[69] "Structural Analysis of Group V, VI, and VII Metal Compounds by XAFS"; Asakura, H.; Shishido, T.; Yamazoe, S.; Teramura, K.; Tanaka, T.; J. Phys. Chem. C, 115 (2011), pp. 23653–23663

[70] "Revised effective ionic radii and systematic studies of interatomic in Halides and Chalkogenides"; Shannon, R. D.; Acta Cryst. A32 (1976), p. 751–767

[71] "Investigation of the structural environment of Ta in a silicate glass and water system under high P–T conditions"; Mayanovic, R. A.; Yan, H.; Anderson, A. J.; Solferino, G.; Journal of Non-Crystalline Solids, 368 (2013), pp. 71–78

[72] "Direct observation of fractional change of niobium ionic species in a solution by means of X-ray absorption fine structure spectroscopy"; Kubouchi, Y.; Hayakawa, S.; Namatame, H.; Hirokawa, T.; X-Ray Spectrom., 41 (2012), pp. 259–263

[73] "Structural environment of Nb5+ in dry and fluid-rich (H2O, F) silicate glasses: A combined XANES and EXAFS study"; Piilonen, P. C.; Farges, F.; Linnen, R. L.; Brown, Jr., G. E.; Pawlak, M.; Pratt, A.; The Canadian Mineralogist, 44 (2006), pp. 775–794

[74] http://ruby.chemie.uni-freiburg.de/Vorlesung/oxide_3_3_mo2.html (July 29, 2015)

[75] "Coordination and Valence of Niobium in TiO2-NbO2 Solid Solutions through X-Ray Absorption Spectroscopy"; Antonio, M. R.; Song, I.; Yamaha, H.; Journal Of Solid State Chemistry, 93 (1991), pp. 183–192

[76] "Structure of surface tantalate species and photo-oxidation of carbon monoxide over silica-supported tantalum oxide"; Tanaka, T.; Nojima, H.; Yamamoto, T.; Takenaka, S; Funabiki, T; Yoshida, S.; Phys. Chem. Chem. Phys., 1 (1999), pp. 5235 –5239

[77] "Niobium and tantalum in minerals: Siderophile, chalcophile or lithophile, and polyvalent"; Martin, R. F.; Wülser, P.-A.; Journal of Geochemical Exploration, 147 (2014), pp. 16–25

[78] "Facile removal of stabilizer-ligands from supported gold nanoparticles"; Lopez-Sanchez, J. A.; Dimitratos, N.; Hammond, C.; Brett, G. L.; Kesavan, L.; White, S.; Miedziak, P.; Tiruvalam, R.; Jenkins, R. L.; Carley, A. F.; Knight, D.; Kiely, C. J.; Hutchings, G. J.; Nature Chemistry, 3 (2011), pp. 551–556

[79] "Laser ablation of a platinum target in water. III. Laser-induced reactions"; Nichols, W. T.; Sasaki,T.; Koshizaki, N.; Journal of applied physics, 100 (2006), p. 114913

[80] "Estimation of surface oxide on surfactant-free gold nanoparticles laser-ablated in water"; Muto, H.; Yamada, K.; Miyajima, K.; Mafune, F.; The Journal of Physical Chemistry C, 111 (2007), pp. 17221–17226

[81] Colloid Science: Principles, Methods and Applications; 2nd edition; Cosgrove, T.; Wiley; 2010

[82] "In situ non-DLVO stabilization of surfactant-free, plasmonic gold nanoparticles: Effect of Hofmeister's anions"; Merk, V.; Rehbock, C.; Becker, F.; Hagemann, U.; Nienhaus, H.; Barcikowski, S.; Langmuir, 30 (2014), pp. 4213–4222

[83] "Contribution of shape resonance and Pt-H EXAFS in the Pt L2,3 x-ray absorption edges of supported Pt nanoparticles: Application and consequences for catalyst characterization"; Ramaker, D. E.; Mojet, B. L.; Garriga Oostenbrink, M. T.; Miller, T.; Koningsberger, D. C.; Phys. Chem. Chem. Phys., 1 (1999), pp. 2293–2302

[84] "Identification of CO Adsorption Sites in Supported Pt Catalysts Using high-energy-resolution fluorescence detection X-ray spectroscopy"; Safonova, O. V.; Tromp, M.; van Bokhoven, J. A.; de Groot, F. M; F.; Evans, J.; Glatzel, P.; J. Phys. Chem. B, 110 (2006), pp. 16162–16164

[85] "Sensitivity of Pt x-ray absorption near edge structure to the morphology of small Pt clusters"; Ankudinov, A. L.; Rehr, J. J.; Low, J. J.; Bare, S. R.; J. Chem. Phys., 116 (2002), pp. 1911–1919

[86] "In situ X-ray probing reveals fingerprints of surface Platinum oxide"; Friebel, D.; Miller, D.J.; O'Grady C.P.; Anniyev, T.; Bargar, J.; Bergmann, U.; Ogasawara H.; Wikfeldt, K.T.; Petterson, L.G.M.; Nilson, A.; Phys. Chem. Chem. Phys., 13 (2011), pp. 262–266

[87] "A comparative study of the water gas shift reaction over platinum catalysts supported on CeO2, TiO2 and Ce-modified TiO2"; Gonzalez, I.D.; Navarro, R.M.; Wen, W.; Marinkovic, N.; Rodriguez, J.A.; Rosa, F.; Fierro, J.L.G.; Catalysis Today, 149 (2010), pp. 372–379

[88] "Highly Active and Stable Carbon-Metal Oxide Supported Pt-Pd Nanocatalysts for Oxygen Reduction at Proton Exchange Membrane Fuel Cell Cathodes"; Neburchilov, V.; talk given at the HFC ("Hydrogen + Fuel Cells") conference, June 19th 2013

[89] "ATHENA User's Guide"; Ravel, B.; document version 1.3, 2007

[90] "EXAFS analysis with FEFF an FEFFIT. Part 2: Commentary"; Ravel, B.; version 0.04, workshop, 2000

[91] "Electronic Structure and Soft X-Ray Emission Spectra of 5d Transition Metals"; Nemoshkalenno, V. V.; Antonov, V. N.; Antonov, Vl. N.; John, W.; Wonn, H.; Ziesche, P.; phys. stat. sol. (b), 111 (1982), pp. 11–52

[92] "High Energy Resolution X-ray Absorption Spectroscopy of Environmentally Relevant Lead(II) Compounds"; Swarbrick, J. C.; Skyllberg, U.; Karlsson, T.; Glatzel, P.; Inorg. Chem., 48 (2009), pp. 10748–10756

[93] "Natural line widths of atomic K and L levels, Ka x-ray lines and several KLL auger lines", Krause, M. O.; Oliver, J. H.; J. Phys. Chem. Ref. Data, 8 (1979), pp. 329–338